Quantitative and temporal measurement of autophagy rates and morphological profiles

By

NITIN SAI BEESABATHUNI

DISSERTATION

Submitted in partial satisfaction of the requirements for the degree of

DOCTOR OF PHILOSOPHY

in

Chemical Engineering

in the

OFFICE OF GRADUATE STUDIES

of the

UNIVERSITY OF CALIFORNIA

DAVIS

Approved:

Priya S Shah, Chair

John Albeck

Ambarish Kulkarni

Committee in Charge

2023

Dedicated to my parents, grandmother, and every loving mother across all universes.

Acknowledgments

Without the support of many people during my Ph.D. journey, this work would not have been feasible. First and foremost, I would like to express my deepest gratitude to my advisor. Dr. Priya Shah for her invaluable guidance, support, and mentorship. Her unwavering belief in my abilities helped me navigate through many challenges. I am truly grateful to her for her patience in teaching me technical skills and her guidance in developing my soft and management skills. I am also thankful to Dr. John Albeck for his invaluable feedback and insight throughout, which greatly contributed to the development of my research.

I am deeply indebted to my friends, Shiaki Minami, Timothy Hui, Deepshika Gilbile, and Meghna Jha, for their constant support and help throughout my Ph.D. They were always there to lend a listening ear and provided me with feedback and much-needed breaks during many rough times. I would like to convey my thanks to Ritika Gangaraju, Ana Acosta, Soyoon Park, Eshan Thilakaratne, Neil Adia, and Matthew Kenaston for working with me, sharing my vision, and patiently listening to my ideas of exploring the uncharted territories of research. I would also like to acknowledge Adam Fishburn, Oanh Pham, Shruthi Garimella, Rob Stott, and Judy Anderson Fishburn, for creating a warm and welcoming atmosphere that made me feel at home.

Lastly, I would not be where I am today without the constant support of my parents, Vani Beesabathuni and Chaitanya Beesabathuni. Amma and Nanna, you both sacrificed the most for my career and I don't think I can ever repay my gratitude apart from simply acknowledging you both. I would also like to express my deepest thanks to my sister, Dr. Nitya Beesabathuni, for her incredible support and belief in me. She took on all the family responsibilities as I pursued my Ph.D. far from my home country.

Copyright material acknowledgment

- Part of Chapter 1 contains material originally published in Frontiers in Microbiology:

  Fishburn AT, Pham OH,Kenaston MW, Beesabathuni NS and Shah PS (2022) Let's Get Physical: Flavivirus-Host Protein-Protein Interactions in Replication and Pathogenesis. Front Microbiol. 2022 Mar 3; 13:847588. doi: 10.3389/fmicb.2022.847588.

  Beesbathuni NS contributed to the autophagy section in this work, which is used in Chapter 1

- Chapter 2 contains material originally published in Autophagy journal.

  Beesabathuni NS, Park S, Shah PS (2022) Quantitative and temporal measurement of dynamic autophagy rates. Autophagy. 2022 Sep 24; doi: 10.1080/15548627.2022.2117515.

  Beesbathuni NS conceived and executed this work. which is used in Chapter 2.

- Both articles are modified to comply with the formatting requirements of this thesis.

Abstract

Quantitative and temporal measurement of autophagy rates and morphological profiles

Autophagy is a multistep dynamic degradative process that is essential for maintaining cellular homeostasis. Autophagy is linked to a wide range of diseases, including cancer, metabolic diseases, and aging. Therefore, autophagy is emerging as a promising therapeutic target for many diseases. Systematically quantifying autophagy is critical for gaining fundamental insights and effectively modulating this dysregulated process during diseases. However, current methods do not quantitatively capture the dynamic nature of autophagy with high sensitivity and scalability. In this work, we proposed two approaches to address these limitations and characterize autophagy comprehensively.

Established methods to quantify individual autophagy steps are restricted to steady-state measurements, which provide limited information about the perturbation and the cellular response. We present a theoretical and experimental framework to measure autophagic steps in the form of rates under non-steady state conditions. We use this approach to measure temporal responses to small-molecule drugs and nutrient-deprived conditions. We quantified changes in autophagy rates in as little as 10 min, which can establish direct mechanisms for autophagy perturbation before feedback begins. In summary, this new approach enables the quantification of autophagy flux with high sensitivity and temporal resolution and facilitates a comprehensive understanding of this process.

Dynamic autophagy rate measurements are useful but resource-intensive and limited by the throughput and number of phenotypic measurements. High-throughput methods to characterize autophagy are essential for accelerating the drug discovery process. We developed a highly

scalable image-based profiling approach to characterize ~900 morphological features at a single-cell level with high temporal resolution. We differentiated drug treatments based on morphological profiles using a random forest classifier with ~90% accuracy and identified the key morphological features that govern the classification. Additionally, temporal morphological profiles accurately predicted complex changes in autophagy after perturbation, such as total cargo degradation. This approach can characterize the mechanism of action of perturbations with less resource-intensive measurements. Therefore, this study acts as proof of principle for using image-based profiling in high-throughput autophagy characterization and to identify biologically relevant phenotypes, which can accelerate drug discovery.

Table of Contents

List of Figures and Tables

Chapter 1: Introduction

Chapter 2: Quantitative and temporal measurement of dynamic autophagy rates

Chapter 3: Image-based temporal profiling of autophagy-related phenotypes

Chapter 4: Implications and Future work

Appendix A: Supplemental information for quantitative and temporal measurement of autophagy rates

Chapter 4: Supplemental information for image-based temporal profiling of autophagy-related phenotypes

Chapter 1: *Introduction*

Macroautophagy (hereafter referred to as autophagy) is an intracellular recycling process that breaks down misfolded proteins and damaged organelles into their primary building blocks. This dynamic process involves autophagosome formation, the fusion of autophagosomes with lysosomes, and the degradation of autolysosomes. The word autophagy was derived from the Greek words auto ("self") and phagy ("eating") and was first coined and discovered by Christian de Duve in the 1960s [1]. The field remained dormant until early 1990 when Yoshinori Ohsumi's group developed a method that enabled the monitoring of autophagosomes in yeast, revolutionizing the field. Using this method, Yoshinori Ohsumi's group then identified the essential autophagy-related genes in yeast [2]. His group and many others have later revealed biological mechanisms governing autophagy in yeast as well as in mammalian cells and established autophagy as a crucial cellular process.

Constitutive autophagy is essential for cellular homeostasis and is modulated during many extrinsic stresses such as nutrient deprivation or pathogen infection [3,4]. This process is also dysregulated during chronic diseases associated with aging, neurodegeneration, and cancer [5,6]. Autophagy can be modulated using pharmacological agents and is a major drug development target for treating cancer, neurodegeneration, and pathogen infection [7,8]. Along with medical applications, autophagy modulation has also shown the potential to enhance biomanufacturing by increasing cell longevity [9]. Thus, tools to measure autophagy systematically and extensively will be critical in any application that involves modulating this process. However, the existing methods to measure autophagy do not capture autophagy dynamically and comprehensively.

In this chapter, we briefly introduce the biological mechanism of the autophagy pathway and commonly used autophagy modulators and their mechanism of action. We next discuss autophagy in relevance to cancer and flavivirus infection and address the associated challenges. Finally, we discuss the shortcomings of methods used for measuring autophagy which motivated this study.

Background and motivation

Biology of the autophagy pathway

The autophagy pathway is initiated by the formation of phagophores which are double membrane structures derived from the endoplasmic reticulum of the cell [10]. The phagophores grow and simultaneously encapsulate cytoplasmic components to form closed double-lipid bilayer structures called autophagosomes [11]. The captured cytoplasmic components are commonly referred to as cargo and the cargo captured can either be selective or non-selective. For example, the selective degradation of mitochondria through the autophagy pathway is termed mitophagy. Several autophagy-related (ATG) proteins that are responsible for autophagosome formation and maturation and cargo receptors that mediate the degradation of selective cargo have been identified [12]. MAP1LC3/LC3 (microtubule-associated protein 1 light chain 3) is a vital autophagy protein that is involved in the elongation and development of the autophagosome [13,14]. LC3 also acts as an adaptor protein for capturing specific cargo [15]. LC3 is the most commonly used marker for tracking the autophagy pathway. LC3 is first cleaved by ATG4B to expose the glycine residue at the C-terminus of the protein. This form of the protein is termed LC3-I. LC3-I is then conjugated to phosphodiethaloamine to form LC3-II which is bound to the autophagosome membrane. Processing of the LC3 to LC3-II is shown in detail in **Figure 1-1**. The closed autophagosomes then fuse with lysosomes with the help of many cellular components such as

SNARE complexes, motor proteins and phospholipids to form autolysosomes [16]. The degradative enzymes present inside the lysosomes such as hydrolases degrade the captured material into basic building blocks.

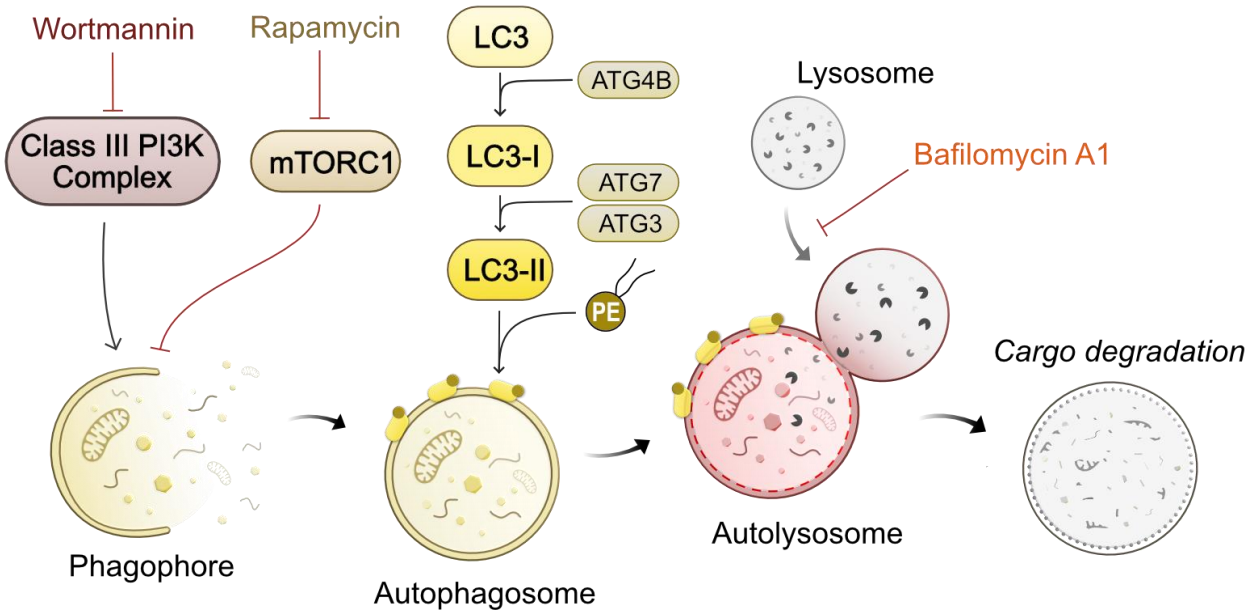

Figure 1-1. Autophagy pathway, key signaling nodes, and commonly used modulators.

The autophagy pathway is linked to many signaling pathways [17]. Here, we briefly discuss some of the key nodes of the autophagy signaling pathway and the commonly used regulators to disrupt the autophagy process (**Fig 1-1**). In nutrient-rich conditions, the mechanistic target of rapamycin kinase complex 1 (mTORC1) is one of the key upstream inhibitors of the autophagy pathway [18,19]. Rapamycin is one of the commonly used small-molecule drugs to selectively inhibit certain aspects of mTORC1 activity [20–22]. Therefore, rapamycin is frequently used for upregulating the autophagy pathway. Class III PI3K complex is another key signaling node that facilitates the growth of the phagophore membrane [23]. Wortmannin is a commonly used regulator that inhibits the autophagy pathway by inhibiting class III PI3K activity [24,25]. On the other hand, bafilomycin A1 is another small molecule drug that is used to disrupt the later stages of the autophagy pathway. The specific role of bafilomycin A1 as an inhibitor of the fusion step of

autophagosome-lysosome or as an inhibitor of the acidification of autolysosomes or both is still unclear [26].

Autophagy and disease

Autophagy has been linked to many diseases such as neurodegenerative diseases, cancer, infectious diseases, and aging (**Fig 1-2A**). In certain diseases, the role of autophagy is complex and the direction of autophagy modulation for therapeutic benefit is ambiguous. As an example, we focus on autophagy in cancer and flavivirus infection, discuss the challenges, and the need for better tools to address these challenges.

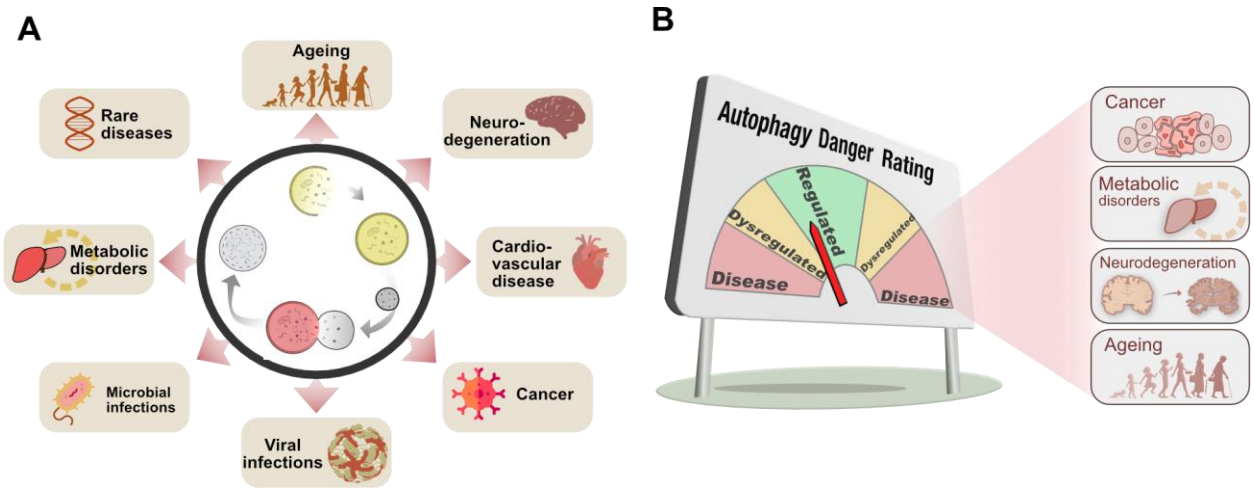

Figure 1- 2. Autophagy and disease. (**A**) Autophagy is linked to various diseases. (**B**) Precise regulation of autophagy is critical for averting further disease.

Autophagy and cancer

Autophagy plays anti-tumorigenic and pro-tumorigenic roles in cancer [27]. The consensus is that the basal level of autophagy is important to maintain cellular quality and to prevent cancer initiation

in healthy cells [28–30]. In later stages of tumor progression, autophagy helps facilitate cancer progression by supplying amino acids and fatty acids for tumor cells growing in a nutrient-starved environment [29,31,32]. Cytostatic effects on tumors were also associated with the upregulation of autophagy during MTOR inhibitor treatments to reduce cell proliferation [33,34]. Therefore, inhibition of autophagy is currently proposed as one of the strategies to maximize therapeutic benefit [7]. Upregulation of autophagy also suppresses tumor growth by initiating autophagy-dependent cell death (ACD) [35,36]. Given such a convoluted relationship between cancer and autophagy, comprehensive characterization and precise modulation of autophagy are pivotal to minimize further disease progression and maximizing therapeutic efficiency (**Fig 1-2B**). Many other key questions that can improve precise regulation strategies remain unanswered as well. For example, the precise amount of autophagy that needs to be perturbed to initiate cell death context dependent? Given the dual roles of autophagy in promoting nutrient availability and initiating cell death, could the same cancer cell be driven to cell death by inhibiting and inducing autophagy, but with different amounts of perturbation? To address such questions and develop rational therapies, accurate and dynamic measurements of autophagy are vital. Nevertheless, most current methods rely on steady state measurements and are inadequate in capturing the dynamic nature of autophagy with high sensitivity and resolution. Dynamic measurements are pivotal in understanding the autophagy system holistically under various genetic and environmental conditions. Quantitative measurements that can distinguish different autophagy steps with high sensitivity would assist in identifying the mechanism of action of new treatments and the cellular response.

Autophagy and flaviviruses

Autophagy is involved in the replication of flaviviruses [37,38]. We generated an extensive list of protein interactions between viral and autophagy proteins from unbiased proteomic screens indicating the involvement of autophagy during flavivirus infection (**Table 1-1**). However, the

overall role of autophagy as a proviral or antiviral in flavivirus replication is complex and has no clear consensus [4,39]. One of the major reasons that cause the ambiguity in implicating the role of autophagy in flavivirus infection is the lack of quantitative and sensitive methods to measure autophagy. Additionally, although both autophagy and virus replication are highly dynamic processes, most methods currently available cannot quantify individual autophagy steps temporally leading to an incomplete picture. Therefore, the need for systematic methods to measure autophagy dynamically and precisely during virus infection cannot be overstated. Such methods will provide insights into the specific autophagy step perturbed by the viral components as a function of time, the cellular response, and hence the overall role of autophagy in the life cycle of virus replication. Interestingly, most of the autophagy proteins that were identified in our search were cargo receptors such as FAM134C, CALCOCO1, and BNIP3 (**Table 1-1**). This leads to the hypothesis that selective autophagy plays a key role in virus replication and is consistent with existing studies showing the upregulation of lipophagy and downregulation of reticulophagy during dengue virus infection [40,41]. This adds a layer of complexity to measuring autophagy where the cargo that's captured and processed also needs to be monitored. Hence, tools to capture the temporal change in autophagy state, cargo captured, and degraded are essential for understanding the interplay between autophagy and virus replication.

Autophagy protein	Autophagy related role	Viral proteins
ACBD5	Pexophagy receptor	NS4A[1]
AMBRA1	Key regulator of autophagy by modulating the BECN1-PIK3C3 complex	NS1[7], NS2B[7]
ATG9A	Supplies membrane for the growing autophagosome	E[7]
BNIP3 (NIP3)	Mitophagy receptor	NS5[1,2]
EI24(EPG4)	Regulates the formation of degradative autolysosomes during autophagy	NS1[2], NS4B[3]
LGALS8	Restricts infection by initiating autophagy via interaction with CALCOCO2/NDP52	NS3[6]
MTOR	Key regulator of autophagy through phosphorylation of ULK1, DAP, AMBRA1, and RUBCNL	NS4A[1,2]
PHB2	Mitophagy receptor	NS2B3[3], NS4B[3]
SQSTM1 (p62)	Multiple cargo receptor	NS4B[2]
STX17	Regulates autophagosome fusion with lysosomes	NS2A[7]
VCP	Essential for the maturation of ubiquitin-containing autophagosomes and the clearance of ubiquitinated protein by autophagy	NS2B3[5]
WAC	Regulator of autophagy	NS2B[6]
AUP1	Lipophagy regulator	NS2A[4], NS4B[3,4]
FAM134C	Reticulophagy receptor	NS4A[1], NS4B[3]
RTN3	Reticulophagy receptor	NS4A[1]
SEC62	Reticulophagy receptor	NS4A[2]
CALCOCO1	Reticulophagy receptor	NS5[5]
NBR1	Aggrephagy, pexophagy and xenophagy receptor	NS2A[4]
VMP1	Required for autophagosome biogenesis	NS4A[4]
TMEM41B	Required for autophagosome biogenesis	NS4B[3]

Table 1-1. Protein–protein interaction (PPI) found between autophagy proteins and viral proteins. Six data sets were used for analysis [42–47]. Superscript represents the viral protein and study reporting the interaction. 1Shah et al. (2018) (ZIKV) [44]. 2Shah et al. (2018) (DENV) [44]. 3 Scaturro et al. (2018) (ZIKV) [43], 4Coyaud et al. (2018) (ZIKV) [42]. 5 Li et al. (2019) (WNV) [45]. 6Golubeva et al. (2020) (ZIKV) [46]. 7 Zeng et al. (2020) (ZIKV) [47]. PPIs that were found significant by the authors were considered for the search. Approximately, 100 autophagy proteins were probed for interactions based on a list of proteins mentioned in these studies [12,48,49].

Challenges associated with measuring autophagy and limitations of current methods.

Western blot

Western blot is commonly used to estimate the change in protein levels. For autophagy measurement, the amount of LC3-II protein is compared before and after autophagy regulation. To further comprehend if autophagosome initiation is modulated or autophagosome fusion, lysosome inhibitors are added to prevent autophagosome clearance and LC3-II levels are

compared. Lack of requirement of sophisticated equipment makes western blot a widely used method for estimating autophagy. However, western blots are typically low throughput and less quantitative. Moreover, western blot measurements do not allow the dissection of all the autophagic steps as the measured LC3-II is associated with both autophagosomes and autolysosomes.

Fluorescence microscopy and flow cytometry

Fluorescent reporter systems have enabled the quantification of autophagosomes in live cells. Green fluorescent protein (GFP) labeling of LC3 allows for the quantification of autophagosomes as spots in cells using fluorescence microscopy. GFP is pH sensitive and is bleached in the acidic environment of the autolysosome in this system [50,51]. Tandem green and red (GFP-RFP) labeling of LC3 has also been used to identify acidic autolysosomes since RFPs are more acid-stable [52,53]. Even though these systems allow direct monitoring of autophagosomes and autolysosomes in real-time, they do not provide direct quantification of each step, also known as 'autophagy flux'. For instance, the accumulation of autophagosomes could be a result of an increase in the formation or decrease in the clearance of autophagosomes. The same principle applies to autolysosomes.

To quantitatively measure autophagy flux, the inputs and outputs of autophagosome and autolysosome accumulation must be dissected. Measuring autophagosome accumulation after inhibiting clearance with small molecules such as bafilomycin A_1 is a commonly used approach for measuring autophagic flux [54]. Nevertheless, this approach does not provide a direct quantification of autophagosome and autolysosome clearance steps. Using a similar approach, Loos and colleagues have formalized a theoretical framework to systematically measure

autophagy in the form of steady-state rates [55]. In 2018, they experimentally validated this theoretical approach using fluorescence-based live cell imaging and described a detailed experimental setup [56]. Although steady-state measurements provide critical information about the end state of the system, it lacks information about the path taken by the system to reach that state. For example, two opposite perturbations might reach the same final state but might have a different mechanism of action (**Fig 1-3A and B**).

A new approach using a novel fluorescent probe was described to quantify autophagic flux by measuring the GFP/RFP signal ratio without adding lysosomal inhibitors [57]. The GFP/RFP intensity can be measured using flow cytometry or fluorescence microscopy. However, this method does not provide a direct quantification of autolysosomes. It is also not sensitive to identifying differences in the autophagic flux if the changes are relatively similar. For example, inhibition of autophagosome formation could lead to similar changes in both GFP and RFP signals. Thus, a true change in flux may still result in a similar GFP/RFP ratio as basal, leading to ambiguity. Another case could be equal and simultaneous initiation and inhibition of autophagosome formation and clearance (resulting in a constant GFP signal), which could lead to no observable difference in the fluorescence levels. Finally, most measurements made using the methods discussed above are made long after perturbation, when the system reaches a new steady state where the rates of all the steps are equal. Although this provides very useful information about the final autophagy state, it is incapable of informing the nature of the perturbation and the dynamic response of the cells to the perturbation. To illustrate, an autophagosome formation inhibitor and an autophagosome formation inducer might reach the same final steady state even though they perturb autophagy very differently. Therefore, it is essential to temporally quantify all the steps involved in autophagy to gain a better understanding of the perturbation as well as the regulatory mechanisms of this dynamic process.

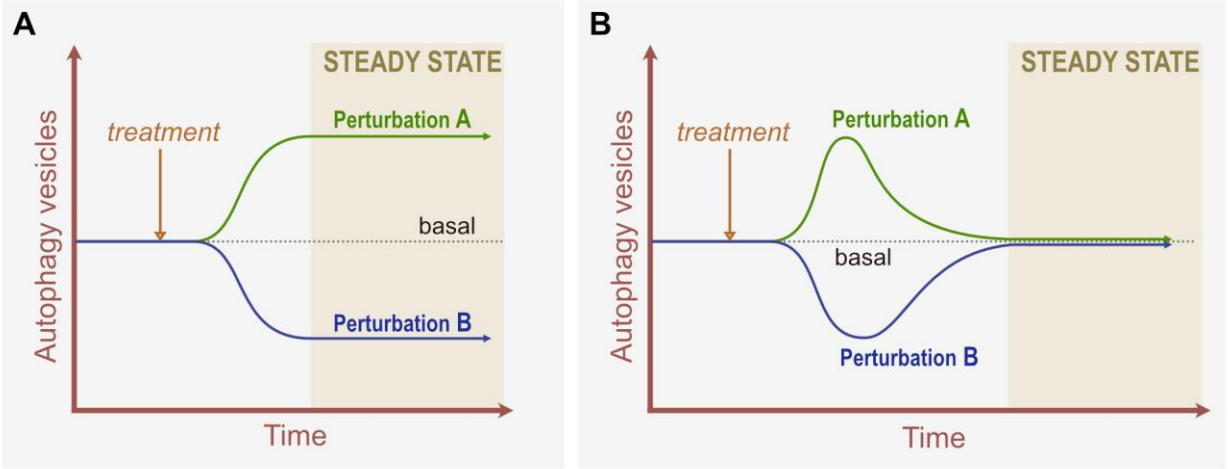

Figure 1-3. Dynamic response of autophagy to perturbations. (A) Perturbations that can change the steady state level of autophagy. (B) Perturbation affects autophagy, but the final steady state is the same as the initial.

Conclusion

In conclusion, methods that can measure individual autophagy steps with high temporal resolution and sensitivity would assist in a better understanding of the biological mechanism of autophagy, and perturbations that affect autophagy and would ultimately lead to the development of precision therapies for treating diseases. Furthermore, developing such methods that can be scalable would accelerate the drug discovery process.

To address these challenges, we propose two new methods for systematically characterizing the dynamic change in the autophagy state. Both these methods rely on automated live cell imaging, fluorescence microscopy, and image analysis. The first method is based on a theoretical framework that allows the monitoring of individual autophagy steps in terms of rates with high sensitivity and temporal resolution. This method highlighted the importance of measuring autophagy dynamically and revealed novel insights into the timescale of autophagy regulation for

various perturbations. The second method is based on an image-based profiling approach where about 900 phenotypic measurements were measured at a single cell level temporally. This approach allows high-throughput characterization of autophagy and accurately captures the dynamic changes in the autophagy state. Together, these methods would accelerate drug discovery for autophagy modulation, provide new fundamental insights into biological mechanisms and facilitate the establishment of systematic autophagy measurements.

References

[1] Ohsumi Y. Historical landmarks of autophagy research. Cell Res 2014 241 [Internet]. 2013 [cited 2023 Jan 8];24:9–23. Available from: https://www.nature.com/articles/cr2013169.

[2] Takeshige K, Baba M, Tsuboi S, et al. Autophagy in yeast demonstrated with proteinase-deficient mutants and conditions for its induction. J Cell Biol [Internet]. 1992 [cited 2023 Jan 8];119:301–311. Available from: http://rupress.org/jcb/article-pdf/119/2/301/1418421/301.pdf.

[3] Green DR, Levine B. Review To Be or Not to Be ? How Selective Autophagy and Cell Death Govern Cell Fate. Cell. 2014;157:65–75.

[4] Choi Y, Bowman JW, Jung JU. Autophagy during viral infection - A double-edged sword. Nat Rev Microbiol [Internet]. 2018;16:341–354. Available from: http://dx.doi.org/10.1038/s41579-018-0003-6.

[5] Hansen M, Rubinsztein DC, Walker DW. Autophagy as a promoter of longevity: insights from model organisms. 2018;

[6] Nixon RA. The role of autophagy in neurodegenerative disease [Internet]. Nat. Med. Nature Publishing Group; 2013 [cited 2021 Jun 12]. p. 983–997. Available from:

https://www.nature.com/articles/nm.3232.

[7] Mulcahy Levy JM, Thorburn A. Autophagy in cancer: moving from understanding mechanism to improving therapy responses in patients. Cell Death Differ. Springer Nature; 2020. p. 843–857.

[8] Galluzzi L, Pedro JMB, Levine B, et al. Pharmacological modulation of autophagy : therapeutic potential and persisting obstacles. Nat Publ Gr [Internet]. 2017;16:487–511. Available from: http://dx.doi.org/10.1038/nrd.2017.22.

[9] Kim YJ, Baek E, Lee JS, et al. Autophagy and its implication in Chinese hamster ovary cell culture. Biotechnol Lett. 2013;35:1753–1763.

[10] Axe EL, Walker SA, Manifava M, et al. Autophagosome formation from membrane compartments enriched in phosphatidylinositol 3-phosphate and dynamically connected to the endoplasmic reticulum. J Cell Biol [Internet]. 2008 [cited 2023 Jan 8];182:685–701. Available from: www.jcb.org/cgi/doi/10.1083/jcb.200803137.

[11] Yu L, Chen Y, Tooze SA. Autophagy pathway: Cellular and molecular mechanisms. 2018 [cited 2023 Jan 8]; Available from: https://doi.org/10.1080/15548627.2017.1378838.

[12] Galluzzi L, Baehrecke EH, Ballabio A, et al. Molecular definitions of autophagy and related processes. EMBO J [Internet]. 2017 [cited 2023 Jan 8];36:1811–1836. Available from: https://onlinelibrary.wiley.com/doi/full/10.15252/embj.201796697.

[13] Suzuki K, Kirisako T, Kamada Y, et al. The pre-autophagosomal structure organized by concerted functions of APG genes is essential for autophagosome formation. EMBO J [Internet]. 2001 [cited 2023 Jan 8];20:5971–5981. Available from: https://pubmed.ncbi.nlm.nih.gov/11689437/.

[14] Xie Z, Nair U, Klionsky DJ. Atg8 controls phagophore expansion during autophagosome

formation. Mol Biol Cell [Internet]. 2008 [cited 2023 Jan 8];19:3290–3298. Available from: https://pubmed.ncbi.nlm.nih.gov/18508918/.

[15] Rogov V, Dötsch V, Johansen T, et al. Interactions between autophagy receptors and ubiquitin-like proteins form the molecular basis for selective autophagy. Mol Cell [Internet]. 2014 [cited 2023 Jan 8];53:167–178. Available from: https://pubmed.ncbi.nlm.nih.gov/24462201/.

[16] Lőrincz P, Juhász G. Autophagosome-Lysosome Fusion. J Mol Biol. 2020;432:2462–2482.

[17] He C, Klionsky DJ. Regulation Mechanisms and Signaling Pathways of Autophagy. 2009 [cited 2023 Jan 8]; Available from: www.annualreviews.org.

[18] Jung CH, Ro SH, Cao J, et al. mTOR regulation of autophagy. FEBS Lett [Internet]. 2010 [cited 2023 Jan 8];584:1287–1295. Available from: https://pubmed.ncbi.nlm.nih.gov/20083114/.

[19] Kim J, Kundu M, Viollet B, et al. AMPK and mTOR regulate autophagy through direct phosphorylation of Ulk1. Nat Cell Biol 2011 132 [Internet]. 2011 [cited 2023 Jan 8];13:132–141. Available from: https://www.nature.com/articles/ncb2152.

[20] Brown EJ, Albers MW, Bum Shin T, et al. A mammalian protein targeted by G1-arresting rapamycin-receptor complex. Nature [Internet]. 1994 [cited 2021 Jun 13];369:756–758. Available from: https://www.nature.com/articles/369756a0.

[21] Sabatini DM, Erdjument-Bromage H, Lui M, et al. RAFT1: A mammalian protein that binds to FKBP12 in a rapamycin-dependent fashion and is homologous to yeast TORs. Cell [Internet]. 1994 [cited 2021 Jun 13];78:35–43. Available from: http://www.cell.com/article/0092867494905703/fulltext.

[22] Sabersu CJ, Martinl1 MM, Brunnj GJ, et al. THE JOURNAL OF BIOLOGICAL CHEMISTRY

Isolation of a Protein Target of the FKBP12-Rapamycin Complex in Mammalian Cells*. 1995.

[23] Petiot A, Ogier-Denis E, Blommaart EFC, et al. Distinct Classes of Phosphatidylinositol 3â€^{2}-Kinases Are Involved in Signaling Pathways That Control Macroautophagy in HT-29 Cells*. J Biol Chem. 2000;275:992–998.

[24] Blommaart' EFC, Krause2 U, Schellens3 JPM, et al. The phosphatidylinositol 3-kinase inhibitors wortmannin and LY 294002 inhibit autophagy in isolated rat hepatocytes. Eur J Biochem [Internet]. 1997 [cited 2023 Jan 8];243. Available from: https://febs.onlinelibrary.wiley.com/doi/10.1111/j.1432-1033.1997.0240a.x.

[25] Petiot A, Ogier-Denis E, Blommaart EFC, et al. Distinct classes of phosphatidylinositol 3'-kinases are involved in signaling pathways that control macroautophagy in HT-29 cells. J Biol Chem. 2000;275:992–998.

[26] Klionsky DJ, Elazar Z, Seglen PO, et al. Does bafilomycin A1 block the fusion of autophagosomes with lysosomes? Autophagy. 2008;4:849–850.

[27] White E. Deconvoluting the context-dependent role for autophagy in cancer. Nat Rev Cancer 2012 126 [Internet]. 2012 [cited 2023 Jan 9];12:401–410. Available from: https://www.nature.com/articles/nrc3262.

[28] Takamura A, Komatsu M, Hara T, et al. Autophagy-deficient mice develop multiple liver tumors. Genes Dev [Internet]. 2011 [cited 2023 Jan 9];25:795–800. Available from: https://pubmed.ncbi.nlm.nih.gov/21498569/.

[29] Karantza-Wadsworth V, Patel S, Kravchuk O, et al. Autophagy mitigates metabolic stress and genome damage in mammary tumorigenesis. Genes Dev [Internet]. 2007 [cited 2023 Jan 9];21:1621–1635. Available from: https://pubmed.ncbi.nlm.nih.gov/17606641/.

[30] Mathew R, Kongara S, Beaudoin B, et al. Autophagy suppresses tumor progression by limiting chromosomal instability. Genes Dev [Internet]. 2007 [cited 2023 Jan 9];21:1367–1381. Available from: https://pubmed.ncbi.nlm.nih.gov/17510285/.

[31] Lum JJ, Bauer DE, Kong M, et al. Growth Factor Regulation of Autophagy and Cell Survival in the Absence of Apoptosis. Cell. 2005;120:237–248.

[32] Degenhardt K, Mathew R, Beaudoin B, et al. Autophagy promotes tumor cell survival and restricts necrosis, inflammation, and tumorigenesis. Cancer Cell [Internet]. 2006 [cited 2023 Jan 9];10:51–64. Available from: https://pubmed.ncbi.nlm.nih.gov/16843265/.

[33] Bissler JJ, McCormack FX, Young LR, et al. Sirolimus for Angiomyolipoma in Tuberous Sclerosis Complex or Lymphangioleiomyomatosis. N Engl J Med [Internet]. 2008 [cited 2023 Jan 9];358:140–151. Available from: https://www.nejm.org/doi/full/10.1056/nejmoa063564.

[34] Marsh DJ, Trahair TN, Martin JL, et al. Rapamycin treatment for a child with germline PTEN mutation. Nat Clin Pract Oncol 2008 56 [Internet]. 2008 [cited 2023 Jan 9];5:357–361. Available from: https://www.nature.com/articles/ncponc1112.

[35] Fulda S, Kögel D. Cell death by autophagy: emerging molecular mechanisms and implications for cancer therapy. Oncogene 2015 3440 [Internet]. 2015 [cited 2023 Jan 9];34:5105–5113. Available from: https://www.nature.com/articles/onc2014458.

[36] Jung S, Jeong H, Yu SW. Autophagy as a decisive process for cell death. Exp Mol Med 2020 526 [Internet]. 2020 [cited 2023 Jan 9];52:921–930. Available from: https://www.nature.com/articles/s12276-020-0455-4.

[37] Ke P-Y. The Multifaceted Roles of Autophagy in Flavivirus-Host Interactions. Int J Mol Sci. 2018;19:3940.

[38] Fishburn AT, Pham OH, Kenaston MW, et al. Let's Get Physical: Flavivirus-Host Protein–Protein Interactions in Replication and Pathogenesis. Front Microbiol. 2022;13.

[39] Echavarria-Consuegra L, Smit JM, Reggiori F. Role of autophagy during the replication and pathogenesis of common mosquito-borne flavi- and alphaviruses. Open Biol. 2019;9.

[40] Lennemann NJ, Coyne CB. Dengue and Zika viruses subvert reticulophagy by NS2B3-mediated cleavage of FAM134B. Autophagy [Internet]. 2017;13:322–332. Available from: http://dx.doi.org/10.1080/15548627.2016.1265192.

[41] Zhang J, Lan Y, Li MY, et al. Flaviviruses Exploit the Lipid Droplet Protein AUP1 to Trigger Lipophagy and Drive Virus Production. Cell Host Microbe [Internet]. 2018;23:819-831.e5. Available from: https://doi.org/10.1016/j.chom.2018.05.005.

[42] Coyaud E, Ranadheera C, Cheng D, et al. Global Interactomics Uncovers Extensive Organellar Targeting by Zika Virus. Mol Cell Proteomics [Internet]. 2018 [cited 2023 Jan 9];17:2242–2255. Available from: https://pubmed.ncbi.nlm.nih.gov/30037810/.

[43] Scaturro P, Stukalov A, Haas DA, et al. An orthogonal proteomic survey uncovers novel Zika virus host factors. Nature [Internet]. 2018 [cited 2023 Jan 9];561:253–257. Available from: https://pubmed.ncbi.nlm.nih.gov/30177828/.

[44] Shah PS, Link N, Jang GM, et al. Comparative Flavivirus-Host Protein Interaction Mapping Reveals Mechanisms of Dengue and Zika Virus Pathogenesis. Cell. 2018;175:1931-1945.e18.

[45] Li M, Johnson JR, Truong B, et al. Identification of antiviral roles for the exon-junction complex and nonsense-mediated decay in flaviviral infection. Nat Microbiol [Internet]. 2019 [cited 2023 Jan 9];4:985–995. Available from: https://pubmed.ncbi.nlm.nih.gov/30833725/.

[46] Golubeva VA, Nepomuceno TC, Gregoriis G de, et al. Network of Interactions between

ZIKA Virus Non-Structural Proteins and Human Host Proteins. Cells [Internet]. 2020 [cited 2023 Jan 9];9. Available from: https://pubmed.ncbi.nlm.nih.gov/31936331/.

[47] Zeng J, Dong S, Luo Z, et al. The Zika Virus Capsid Disrupts Corticogenesis by Suppressing Dicer Activity and miRNA Biogenesis. Cell Stem Cell [Internet]. 2020 [cited 2023 Jan 9];27:618-632.e9. Available from: https://pubmed.ncbi.nlm.nih.gov/32763144/.

[48] Gatica D, Lahiri V, Klionsky DJ. Cargo recognition and degradation by selective autophagy. Nat Cell Biol [Internet]. 2018;20:233–242. Available from: http://dx.doi.org/10.1038/s41556-018-0037-z.

[49] Gubas A, Dikic I. A Guide To… The regulation of selective autophagy receptors. FEBS J. 2021;

[50] Kabeya Y, Mizushima N, Ueno T, et al. LC3 , a mammalian homologue of yeast Apg8p , is localized in autophagosome membranes after processing. 2000;19.

[51] Bampton ETW, Goemans CG, Niranjan D, et al. The dynamics of autophagy visualized in live cells: from autophagosome formation to fusion with endo/lysosomes. Autophagy. 2005;1:23–36.

[52] Kimura S, Noda T, Yoshimori T. Dissection of the autophagosome maturation process by a novel reporter protein, tandem fluorescent-tagged LC3. Autophagy. 2007;3:452–460.

[53] Tanida I, Ueno T, Uchiyama Y. A super-ecliptic, phluorin-mkate2, tandem fluorescent protein-tagged human LC3 for the monitoring of mammalian autophagy. PLoS One. 2014;9:3–10.

[54] Fass E, Shvets E, Degani I, et al. Microtubules support production of starvation-induced autophagosomes but not their targeting and fusion with lysosomes. J Biol Chem. 2006;281:36303–36316.

[55] Loos B, Du Toit A, Hofmeyr JHS. Defining and measuring autophagosome flux - Concept and reality. Autophagy. 2014;10:2087–2096.

[56] Toit A, Hofmeyr JS, Gniadek TJ, et al. Measuring autophagosome flux. Autophagy [Internet]. 2018;00:1–12. Available from: https://doi.org/10.1080/15548627.2018.1469590.

[57] Kaizuka T, Morishita H, Hama Y, et al. An Autophagic Flux Probe that Releases an Internal Control. Mol Cell [Internet]. 2016;64:835–849. Available from: http://dx.doi.org/10.1016/j.molcel.2016.09.037.

Chapter 2: *Quantitative and temporal measurement of dynamic autophagy rates*

Introduction

In this chapter, we present an approach to quantify the rates of each step of the autophagy pathway under non-steady state conditions. This approach directly builds upon previous advances that provided a quantitative framework to measure autophagy rates at a steady state [1,2] and is enabled by high-throughput live cell imaging and measurement of instantaneous autophagy rates. With this approach, we study the effects of well-characterized autophagy regulators rapamycin and wortmannin. Through our non-steady state analysis, we show that rapamycin dynamically regulated autophagy flux to reach an elevated state that decreases back to basal levels over time. We use the non-steady state rate approach to reveal two modes of regulation that cause this dynamic behavior. We further show that rapamycin concentrations can be used to precisely modulate autophagy flux. Conversely, we show wortmannin initially inhibits autophagy flux, which recovers over time in a concentration-dependent manner. Additionally, we performed a similar analysis during serum and glutamine starvation. Measuring rates after starvation indicated that autophagy rates are rapidly and transiently induced by serum starvation, while glutamine starvation inhibited autophagy rates on a longer time scale. Taken together, this innovative approach has the potential to provide novel insights related to autophagy and mechanisms driving autophagy-regulating perturbations through quantitative measurements.

Results

Non-steady state measurement of autophagy rates

Measurement of steady state autophagy flux has long been performed [3,4]. Loos and colleagues established a formal framework to quantify autophagy flux or the rate of autophagosome formation

under steady state conditions [1,2]. The model considers the whole autophagic process as a multistep process governed by three steps: 1) the rate of formation of autophagosomes (R_1), 2) the rate of autolysosome formation via fusion of autophagosomes with lysosomes (R_2) and 3) the rate of degradation of autolysosomes (R_3) (**Fig 2-1A**). This method relies on quantifying autophagosomes and their accumulation over time in live cells by using GFP-labeled LC3 as described above. Performing a mass balance on the autophagosomes (AP) yields an expression for the rate of change of autophagosomes:

$$\frac{dAP}{dt} = R_1 - R_2 \quad (1)$$

Similarly, the rate of change of autolysosomes (AL) can be written as:

$$\frac{dAL}{dt} = R_2 - R_3 \quad (2)$$

Under steady state, no change in autophagosomes or autolysosomes over time is observed because R_1, R_2, and R_3 are equal. Using bafilomycin A_1 to inhibit the fusion of the autophagosome with lysosomes sets $R_2 = 0$ and results in autophagosome accumulation. Immediately post inhibition:

$$\left(\frac{dAP}{dt}\right)_{inh} = R_1 \quad (3)$$

where $\left(\frac{dAP}{dt}\right)_{inh}$ is the accumulation rate of autophagosomes following inhibition of R_2 by bafilomycin A_1 [1,2] (**Fig 2-1B**).

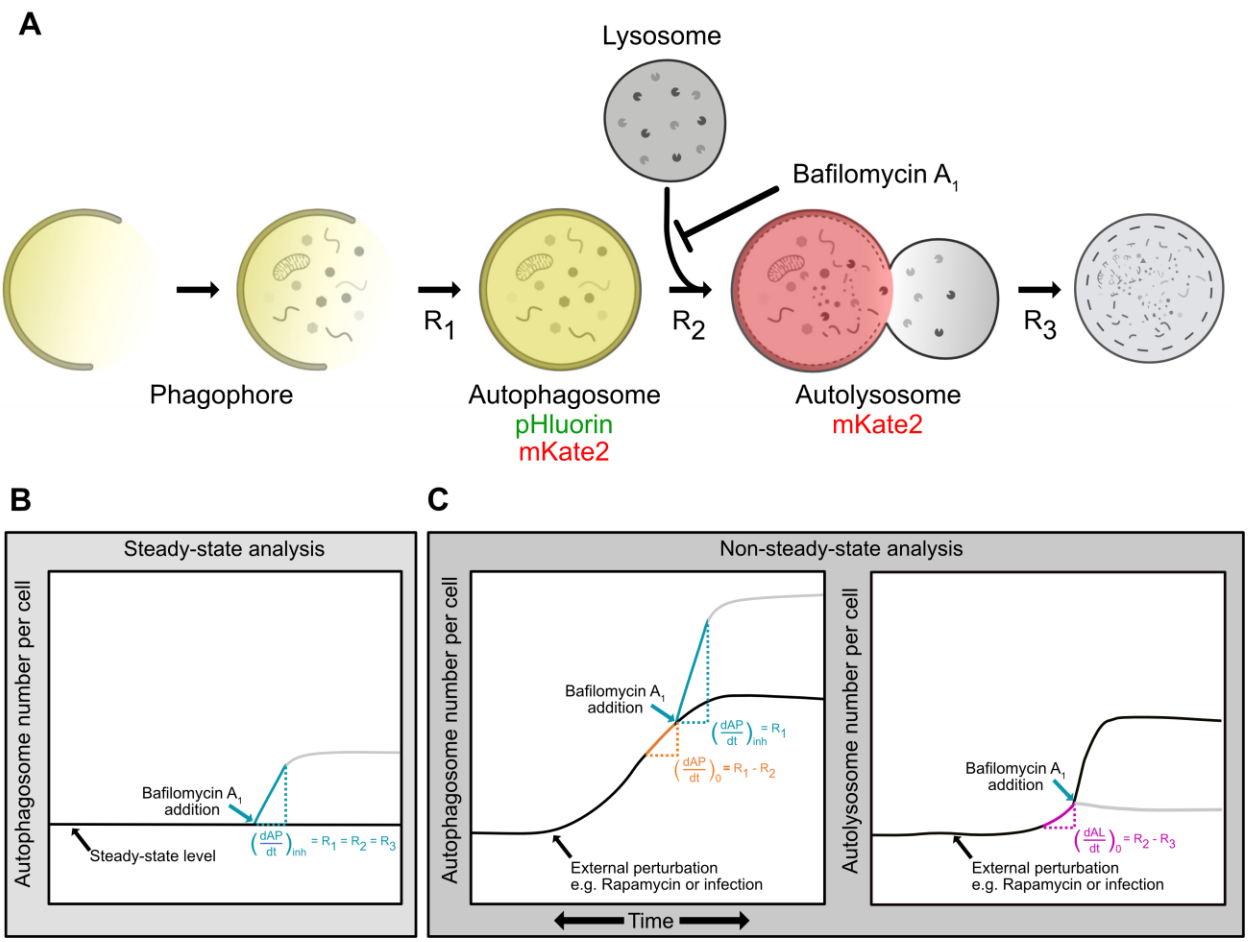

Figure 2-1. Conceptual framework of non-steady state analysis of autophagy rates. (A) Phagophores expand to form autophagosomes. Autophagosomes fuse with lysosomes to form autolysosomes. Contents are degraded in autolysosomes. The rates of each of these steps (R1, R2, and R3) can be measured using a mass action model and live-cell imaging. Fluorescently tagged LC3 (pHluorin-mKate2-LC3) can be used to quantify autophagosomes (pHluorin- and mKate2-positive) and autolysosomes (mKate2-positive, pHluorin is quenched at low pH). (B) Measurement of autophagosome numbers following inhibition of autophagosome-lysosome fusion using bafilomycin A1 allows for measurement of R1, the rate of autophagosome formation. When performed at a steady state, this rate is equal to the other rates in the pathway. (C) When changes in autophagosome and autolysosome numbers are measured using an instantaneous rate approach, all rates in the autophagy pathway (R1, R2, and R3), which may not be equal under dynamic conditions, can be measured.

Despite the success of quantitative autophagy flux measurements, non-steady state measurements (dynamic conditions in which R_1, R_2, and R_3 may not be equal) remain out of reach. We expanded on this previous work to develop a non-steady state rate approach that enables the evaluation of all three rates under dynamic conditions (**Fig 2-1C**). Measuring the change in the number of autophagosomes with time just before the chemical inhibition would

provide the net rate of change of autophagosomes at that time point $\left(\frac{dAP}{dt}\right)_0$. R_2 can then be evaluated using equations (1) and (3):

$$R_2 = R_1 - \left(\frac{dAP}{dt}\right)_0 \quad (4)$$

We can extend this analysis to also quantify the instantaneous net rate of change of autolysosomes $\left(\frac{dAL}{dt}\right)_0$ prior to chemical inhibition. R_3 can be evaluated using equations (2) and (4):

$$R_3 = R_2 - \left(\frac{dAL}{dt}\right)_0 \quad (5)$$

Thus, we can recover the absolute formation and fusion rates of autophagosomes along with the degradation rate of autolysosomes as a function of time by carrying out this approach at multiple time points.

Experimental system to monitor autophagy dynamics.

Accurately quantifying autophagy rates over time requires a method to distinguish autophagosomes from autolysosomes and to track them in live cells simultaneously. Several tandem reporter systems that can distinguish autophagosomes from autolysosomes have been previously described [5–7], though none have been used to extract rate data for all steps in the autophagy pathway. We used the previously developed Super-Ecliptic, pHluorin-mKate2-LC3 system [8]. pHluorin is an acid-sensitive GFP, while mKate2 is an acid-stable RFP. Thus, autophagosomes are green and red, while the acidic autolysosomes are only red (**Fig 2-1A**).

We first confirmed that the accumulation of pHluorin-mKate2-labeled puncta is specific to autophagosomes using the tandem reporter with wild-type (WT) LC3 and a LC3 mutant (LC3 ΔG). LC3 ΔG lacks the glycine at the carboxyl-terminus, which is essential for proper lipidation and association with autophagosomes [9,10]. The addition of bafilomycin A1 and rapamycin, two well-established modulators of autophagy [11,12], lead to the expected accumulation of pHluorin-mKate2-labeled puncta in cells expressing WT LC3, but not in LC3 ΔG-expressing cells (**Fig 2-2A**).

We then calibrated our experimental system to determine the optimal concentration of bafilomycin A_1 to inhibit R_2 completely. We monitored autophagosome and autolysosome dynamics over time before and after the addition of bafilomycin A_1 at various concentrations (**Fig 2-2B and C**). Autophagosome and autolysosome numbers were confirmed to be at a steady state prior to the addition of bafilomycin A_1. We observed a constant increase in autophagosomes over time following the addition of bafilomycin A_1 for all concentrations tested, with more dramatic increases at higher concentrations. For autolysosomes, we did not observe any considerable changes for higher concentrations (100 nM and above) but for 10 nM bafilomycin A_1 we observed an increase in the autolysosome numbers. This could be due to complete inhibition of autolysosome clearance by bafilomycin A_1 [3,11] but only partial inhibition of the fusion step as indicated by the lower slope of autophagosome increase, leading to continuous autolysosome production but no clearance.

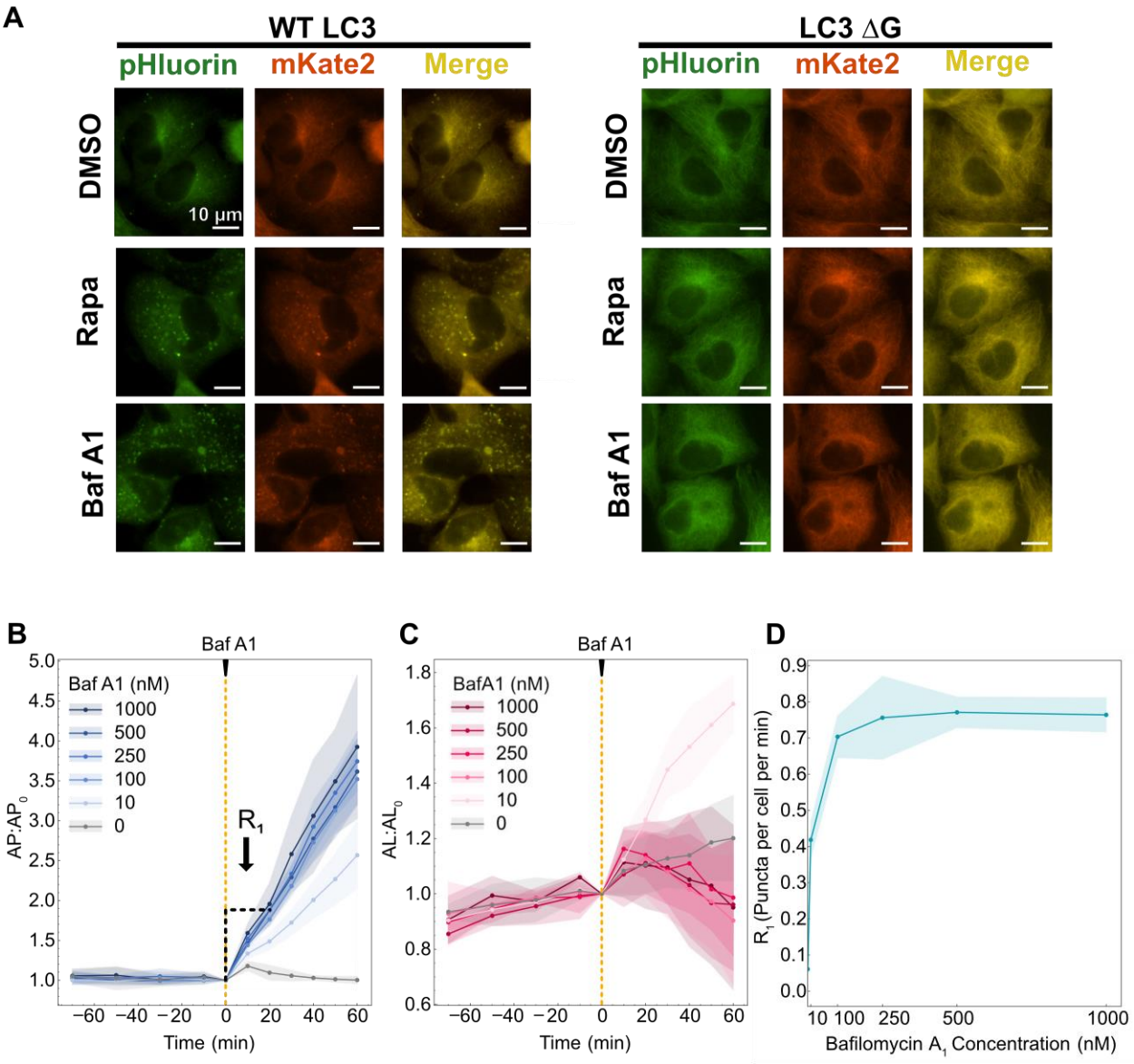

Figure 2-2. Calibration of system conditions for data collection. (A) Images of cells expressing the pHluorin-mKate2-LC3 tandem fluorescent reporter following DMSO, 100 nM rapamycin (Rapa) and 500 nM bafilomycin A1 (Baf A1) treatment. WT LC3 represent wild type and LC3 ΔG was used as a negative control because this mutant cannot be lipidated for phagophore association. (B) Autophagosomes and (C) autolysosomes were quantified over 90 min before addition of bafilomycin A1 and 60 min after. R1 was calculated using the first 20 min of data following bafilomycin A1 treatment. (D) R1 rates are plotted as a function of bafilomycin A1 concentration. At least 150-200 cells were imaged for all experiments.

We used autophagosome data to determine R_1 as a function of bafilomycin A_1 concentration. R_1 was measured as the slope using 20 min of data immediately following the addition of bafilomycin A_1 (**Fig 2-2B**). The ability to measure rates within 20 min is a major advantage of this system as

it allows the measurement of instantaneous R_1 with minimal feedback from bafilomycin A_1 addition. A saturation of R_1 was observed starting at 100 nM bafilomycin A_1 (**Fig 2-2D**). However, to ensure complete inhibition of R_2 even during induced conditions (*e.g.,* higher autophagosome and lysosome numbers), a concentration of 500 nM bafilomycin A_1 was used for all subsequent experiments. We also acknowledge that it may not be possible to differentiate between autophagosomes and autolysosomes after bafilomycin A_1 treatment. This is due to the unclear mechanism of bafilomycin A_1 of either inhibiting fusion of autophagosomes with lysosomes or inhibition of acidification of autolysosomes [13]. Therefore, the measured number of autophagosomes could be accumulated either in the form of unfused autophagosomes or unacidified autolysosomes. Nevertheless, this does not affect our analysis as the approach only relies on measuring autophagosome accumulation after inhibition and we can measure the accumulation in either form. A mathematical explanation is provided in the Appendix A.

Rapamycin-induced autophagosome and autolysosome dynamics are concentration-dependent.

We next tested the ability to monitor autophagosome and autolysosome temporal dynamics using rapamycin, which induces autophagosome formation through the inhibition of MTORC1 (mechanistic target of rapamycin kinase complex 1)[14–16]. We tested seven concentrations of rapamycin (**Fig 2-3, A-1A-B**). Autophagosomes increased following rapamycin treatment, with higher rapamycin concentrations resulting in a more rapid increase (**Fig 2-3A, A-1A**). For the highest concentrations of rapamycin ($\geq$ 10 nM), this rapid increase peaked at 30 min post-treatment, followed by a gradual decrease. We observed a saturation behavior for concentrations above 10 nM. A mid-range concentration of rapamycin (1 nM) resulted in a more gradual increase in autophagosome numbers, followed by a slight decrease. The lowest concentration of rapamycin tested (0.1 nM) had no effect. Autolysosome dynamics followed similar concentration-

dependent trends, with slightly delayed peaks at 1.5-2 h post-treatment for higher concentrations (**Fig 2-3B, A-1B**). Interestingly, there was no difference in autophagosome and autolysosome peak time (3.5-4 h) for the mid-range concentrations of rapamycin (0.5 and 1 nM). The raw autophagosome and autolysosome data are provided in the Appendix A (**Fig A-1C and D**). We also confirmed rapamycin inhibition of MTORC1 activity by monitoring change in the phosphorylation status of the RPS6/S6 ribosomal protein at the Ser 240/244 site, which is a downstream substrate of mTORC1 (**Fig A-1E**).

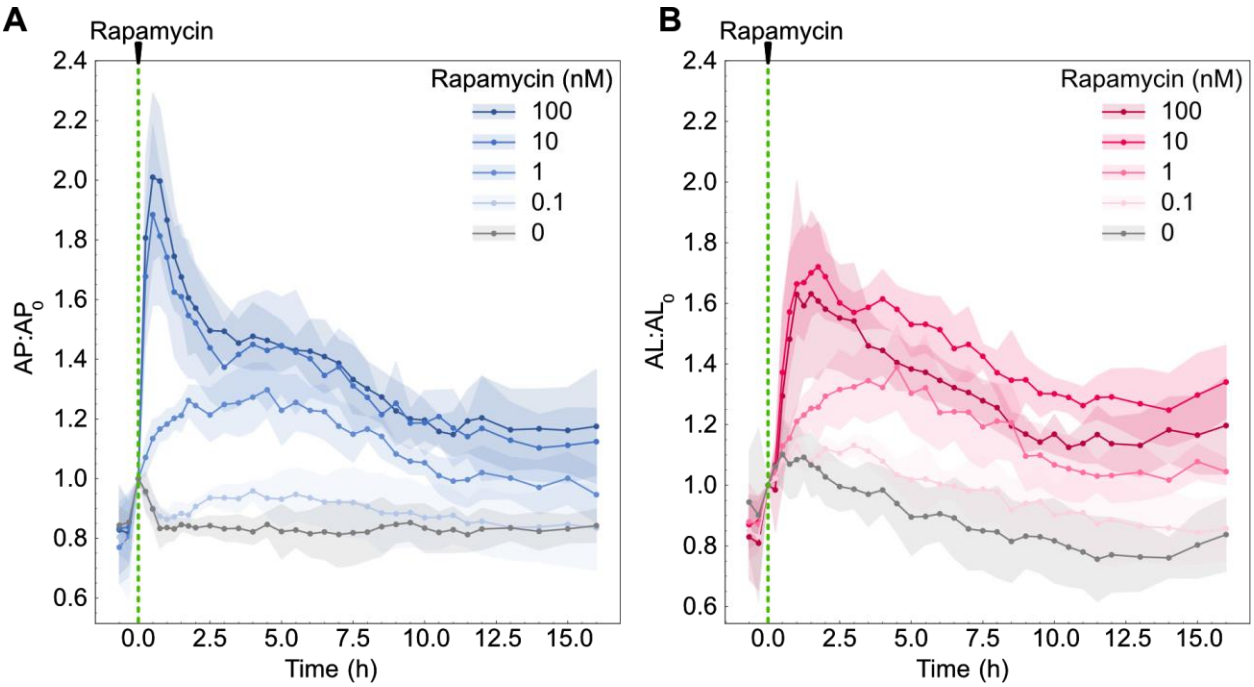

Figure 2-3. Autophagosome and autolysosome dynamics are a function of rapamycin concentration. (**A**) Autophagosome and (**B**) autolysosome number dynamics after rapamycin treatment. The indicated concentration of rapamycin was added at 0 min. The number of autophagosomes and autolysosomes at 0 min was used as the normalization factor. Data points represent mean while shaded area represents ± standard deviation. Four independent replicates were performed. At least 150-200 cells were imaged for all experiments.

Time evolution of autophagy rates reveals initial rate-limiting steps.

The autophagosome dynamics for high concentrations of rapamycin ($\geq$ 10 nM) suggested two possible models of cellular response to rapamycin treatment. The sudden increase in autophagosome numbers followed by a decrease could be driven by a rapid increase in the rate of autophagosome formation (R_1), while the rates of autolysosome formation and degradation (R_2 and R_3, respectively) lag due to latency in the pathway response. Alternatively, R_1 could increase and then decrease due to feedback mechanisms induced by sustained rapamycin treatment. We next sought to distinguish between these two possible cellular response models using the non-steady state rate approach described earlier.

To understand which mode of response cells were operating, we measured R_1, R_2, and R_3 over time following rapamycin treatment. Initially, we focused on cells treated with a high concentration of rapamycin (100 nM) compared to untreated cells (DMSO). Raw autophagosome and autolysosome data used for rate measurements at 30 min are shown as an example to illustrate the procedure followed (**Fig 2-4A and B**). Cells were at a steady state before rapamycin treatment, with no changes in either autophagosome or autolysosome numbers. Following rapamycin addition, we observed an increase in autophagosome and autolysosome numbers, similar to our previous experiments. Bafilomycin A_1 was then added to measure rates. This overall procedure was repeated to collect rate data from 10 min to 15 h post-treatment. Importantly, the rates of untreated cells (basal autophagy rates) were at a steady state, meaning all three rates were equal and did not vary over time (**Fig A-2**).

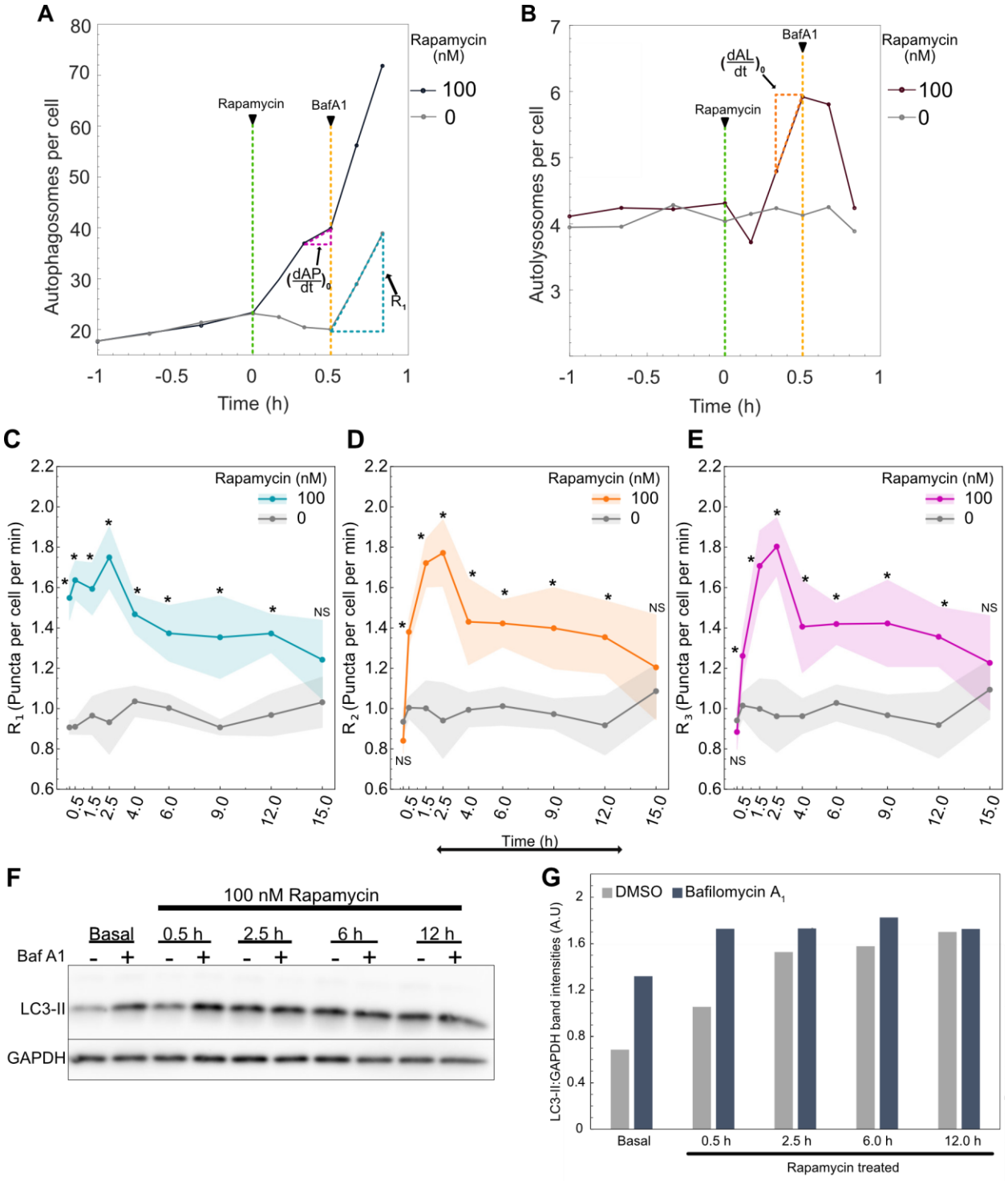

Figure 2-4. Autophagy rates change over time following rapamycin treatment. (**A**) Raw autophagosome and (**B**) raw autolysosome dynamics for rate measurement at 30 min post-rapamycin treatment. R_1 was calculated using the autophagosome data 20 min post-bafilomycin A_1 addition. $\left(\frac{dAP}{dt}\right)_0$ and $\left(\frac{dAL}{dt}\right)_0$ were calculated using the autophagosome and autolysosome data respectively 10 min before bafilomycin A_1 addition. (**C**) Change in R_1 (**D**) R_2 and (**E**) R_3 over time. Data points represent the mean while shaded area

represents ± standard deviation. Four independent replicates were performed. (*) indicates p-value < 0.05 and NS indicates not significant. P-values were calculated using an independent two-tail t-test. (**F**) LC3-II and GAPDH protein quantification using western blot. Cells were treated with 100 nM rapamycin for different time points followed by 500 nM bafilomycin A_1 (Baf A1) treatment. Basal samples represent DMSO-treated cells. (**G**) Quantification of the western blot shown in Fig 2-4F using densitometry. LC3-II band intensity is normalized with the respective GAPDH band intensity in the same lane. At least 150-200 cells were imaged for all imaging experiments.

For rapamycin-treated cells, we observed a nearly immediate increase in R_1, with significant changes in R_1 measured as soon as 10 min post-treatment compared to untreated cells (**Fig 2-4C**). This significantly elevated rate was maintained until 12 h post-treatment. This result is consistent with the known mechanism of rapamycin inducing autophagy upstream of phagophore expansion and thus validates the proposed non-steady state approach to characterize the effects of external perturbation on autophagy. Interestingly, R_2 and R_3 were slower to increase, with significantly increased rates starting at 30 min post-treatment (**Fig 2-4D and E**). Similar to R_1, R_2 and R_3 maintained significantly elevated rates until 12 h post-treatment. At 15 h post-treatment, all rapamycin rates were statistically indistinguishable from the basal rates of untreated cells. The dynamics we observed suggest that R_2 and R_3 may represent rate-limiting steps initially, after which there is a general decrease in all rates.

To confirm the puncta and rate dynamics observed using the new method are consistent with the traditionally used method, we measured LC3-II protein levels using western blot. We treated cells with 100 nM rapamycin for different time points followed by the addition of 500 nM bafilomycin A_1 to measure R_1 (**Fig 2-4F-G and A-3A-B**). Cells were treated with bafilomycin A_1 for 2 h to ensure a consistent and detectable change in the LC3-II levels. Here, the higher sensitivity of the new method is noteworthy, as it can detect changes as soon as 20 min after bafilomycin A_1 treatment compared to 2 h for western blot. We confirmed the increase in LC3-II levels for DMSO samples after treatment with bafilomycin A_1, indicating the inhibition of the fusion step. For just rapamycin

treatment, we observed an increase in LC3-II levels starting at 30 min followed by constant maintenance of LC3-II levels until 12 h post-treatment. This is contrary to the observed autophagosome and autolysosome puncta dynamics where there is an initial increase followed by a decrease (**Fig 2-3A-B**). We hypothesize that the variation between puncta dynamics measurements and western blot measurements is caused by the intrinsic nature of each measurement. LC3-II protein levels measured using western blot indicate the summation of LC3-II protein on autophagosomes and autolysosomes. Both autophagosome and autolysosome puncta remained higher than the initial state even at 15 h, indicating higher levels of LC3-II protein at those time points. Moreover, the number of LC3-II molecules bound to each autophagosome could be dynamic and challenging to measure. Nonetheless, the initial accumulation of LC3-II was consistent between the two methods. To validate the observed R_1 dynamics, bafilomycin A_1 was added at multiple time points after treatment with rapamycin **(Fig 2-4F-G and A-3A-B)**. We observed a clear increase in LC3-II accumulation at 30 min, while for the later time points, it only caused a modest increase. This indicates R_1 is higher initially and declines over time. These results were also consistent with measurements made using the non-steady state method, where R_1 increased over 2.5 h post-treatment, followed by a gradual decrease.

Latency and feedback contribute to rapamycin-driven autophagy rate dynamics.

We next set out to test these temporal differences in rates by comparing rates at different time points for rapamycin-treated cells. At 10 and 30 min post-treatment, R_1 was significantly greater than R_2 and R_3 (**Fig 2-5A**), consistent with the rapid increase in the autophagosome numbers until 30 min post-treatment. But this difference was eliminated by 1.5 h post-treatment because of increases in R_2 and R_3 (**Fig 2-5A**), which is also consistent with the peak time of autolysosome numbers (**Fig 2-3B**). We focused our detailed temporal analysis on R_1 since R_2 and R_3 reached the same level as R_1 and followed the same trend from 1.5 h onward. Interestingly, we observed

a constant R_1 until 2.5 h post-treatment, at which point there was a gradual decrease until 15 h (**Fig 2-5B**). Thus, an increase in the overall flux through the pathway in response to rapamycin is initially limited by latency in R_2 and R_3, but not R_1. This is followed by a general decrease in autophagy rates after 2.5 h. Thus, both models of regulation we initially hypothesized to exist are playing a role in the autophagy dynamics we observed.

To illustrate this hybrid model of cellular response and regulation of autophagy rates, we juxtaposed the autophagosome and autolysosome dynamics with rate data (**Fig 2-5C**). We used 30 min as a reference point to compare the temporal changes in R_1 since autophagosome numbers peak at 30 min. The immediate spike in R_1 but lag for R_2 and R_3 caused the initial accumulation of autophagosomes in the first 30 min. From 30 min to 2.5 h, the decrease in autophagosomes was caused by an increase in R_2 and R_3 to the same level as R_1, leading to the degradation of accumulated autophagosomes, which we named the degradative regime (DR). However, after 2.5 h, the decrease in autophagosome numbers was a result of the decrease in R_1 along with R_2 and R_3, which we named the feedback regime (FR). These results underscore the overall consistency of temporal rate data with the autophagosome and autolysosome dynamics.

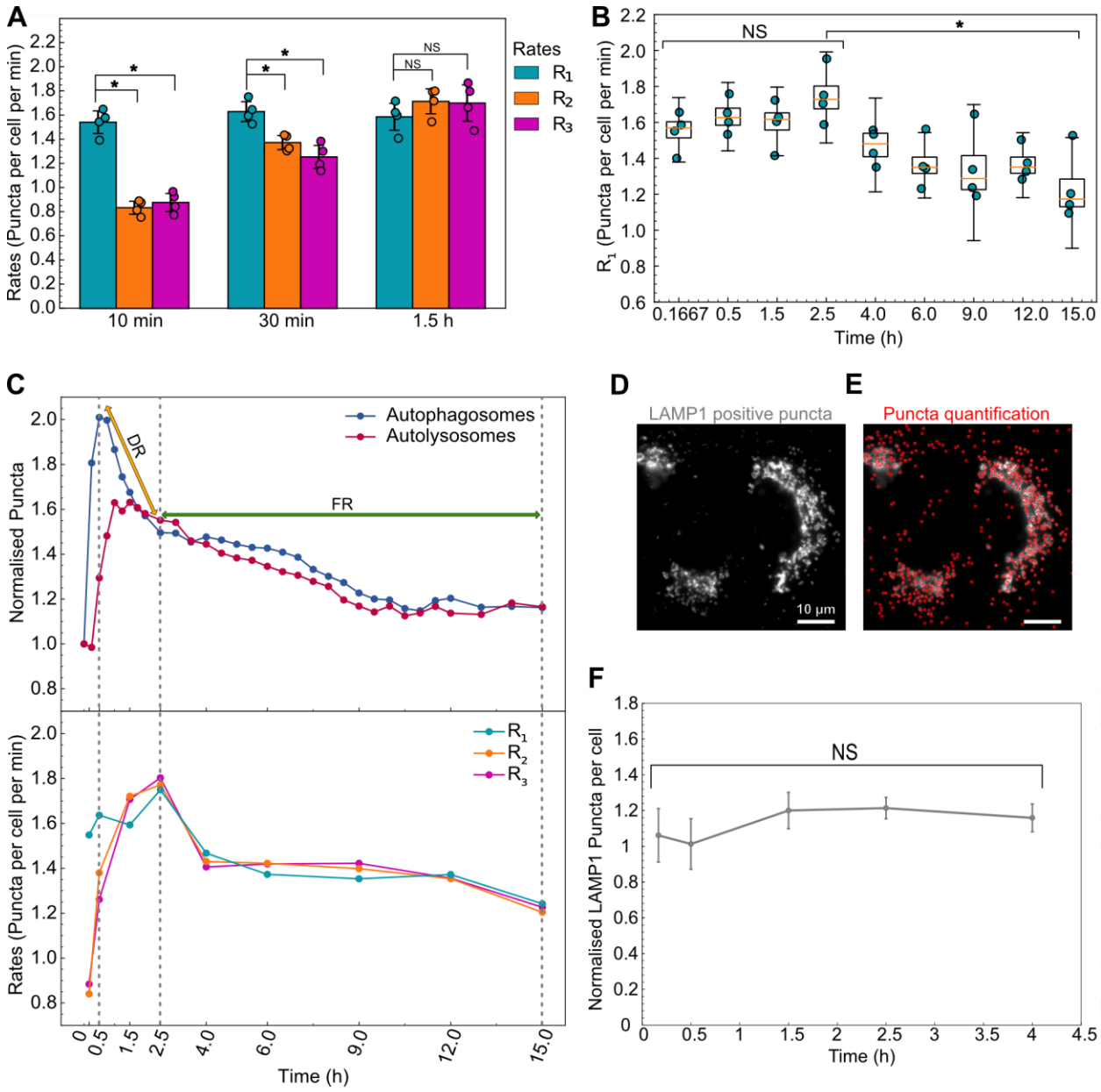

Figure 2-5. Autophagy rates indicate a hybrid model of cellular response to high concentrations of rapamycin. (**A**) Statistical comparison of autophagy rates for cells treated with 100 nM rapamycin at three different time points. (**B**) Temporal change in R_1 for cells treated with 100 nM rapamycin. (*) indicates p-value < 0.05 and NS indicates not significant. Statistical significance for the first four points was calculated using a one-way ANOVA test. The P-value for the statistical test between 2.5 and 15 h is calculated using paired two-tail t-test. (**C**) Normalized mean values of autophagosome ($AP:AP_0$) and autolysosome numbers ($AL:AL_0$) along with mean values of autophagic rates (R_1, R_2, R_3) are compared to visualize the two regimes of cellular response. DR and FR represent degradative and feedback regimes, respectively. (**D**) A549 cells stained with LAMP1 antibody. (**E**) LAMP1 positive puncta detection (shown in red). Scale bar: 10 µm. (**F**) Temporal change in the normalized LAMP1 puncta/ cell (rapamycin treated to DMSO treated) after treatment with 100nM rapamycin. Error bars represent standard error for four

independent replicates. NS indicates not significant, statistical significance was calculated using a one-way ANOVA test. At least 150-200 cells were imaged for all experiments.

We hypothesized that the initial lag in R_2 and R_3 in degradative regime is due to a lack of lysosomes to fuse with the newly formed autophagosomes. To test this hypothesis, we performed immunofluorescence staining for LAMP1 (Lysosomal Associate Membrane Protein 1) after treating cells with 100 nM rapamycin for 4 h (**Fig 2-5D**). We chose 4 h, as R_2 and R_3 reach R_1 by 1.5 h and remain the same thereafter. We quantified the LAMP1-positive puncta for basal and 100 nM rapamycin-treated cells (**Fig 2-5E**). Contrary to our hypothesis, there was no significant difference in the normalized puncta (rapamycin-treated relative to basal) between 10 min and 4 h of rapamycin treatment (**Fig 2-5F**). This indicates that the number of lysosomes is not a limiting factor for the fusion step, and another aspect of autophagosome-lysosome fusion is limiting.

Initial autophagy rates and time evolution of rates depend on rapamycin concentration.

Given the concentration-dependent effects of rapamycin on autophagosome and autolysosome dynamics, we hypothesized that autophagy rates might also exhibit concentration-dependent effects. We thus measured all the rates for a range of rapamycin concentrations over 15 h (**Fig 2-6A and A-4)**. Mid-range concentrations of rapamycin (0.5-1.0 nM) resulted in a more gradual increase in R_1 compared to high rapamycin concentrations (10-100 nM). To quantify rapamycin's ability to induce autophagy, we modeled R_1 using the Hill equation [17] (**Fig 2-6B**). R_1 at 10 min was used to model rapamycin induction kinetics because this time point represents the effect of rapamycin on autophagy with minimal time for feedback mechanisms from the cells. In the Hill equation, $(R_1)_{Basal}$ represents the basal rate of autophagosome formation in the absence of any perturbation. This basal rate was estimated to be 0.90 puncta per cell per minute. V_m and K_m

represent the rapamycin-induced maximal autophagy level and half-maximal rapamycin concentration, respectively. V_m and K_m were estimated to be 0.685 puncta per cell per minute and 1.1 nM. The exponent *n* represents the observed Hill coefficient and was estimated to be 1.9. This model can be used to predict rapamycin's ability to induce R_1 at early stages and will be useful in developing a complete temporal model. This method may be extended to various autophagy perturbations, which may relate to the mechanism of action based on the perturbed initial response and enable modeling of the response.

In addition to concentration-dependent effects on initial R_1, we also observed concentration-dependent effects on the time evolution of R_1. For a mid-range concentration of rapamycin (0.5 nM), R_1 gradually increased and reached the same level as R_1 of higher concentrations (100 nM) over 6 h (**Fig 2-6C**). This was surprising given the very low accumulation of autophagosomes and autolysosomes for 0.5 nM treatment (**Fig A-1A and B**). Consequently, we explored the temporal nature of all autophagy rates (R_1, R_2, and R_3) for this mid-range concentration of rapamycin. We hypothesized that the slower response time for R_1 at mid-range concentrations of rapamycin (**Fig 2-6A**) might allow adequate time for R_2 and R_3 to adjust in sync with R_1, even at early time points, compared to the rapid response for high concentrations of rapamycin (100 nM). Measuring R_2 and R_3 over time showed a similar trend, equal to R_1 over the entire 15 h time course, thus resulting in a low accumulation of the autophagic vesicles (**Fig 2-6D**). Interestingly, rates decreased at longer time points. R_1 was indistinguishable from basal levels by 15 h post-treatment for 0.5 nM rapamycin (**Fig 2-6C**), similar to the high concentration of rapamycin (**Fig 2-4C-E**). This led us to look at long-term impacts on R_1 for all concentrations of rapamycin. For all concentrations tested, R_1 was not significantly different from basal levels by 15 h post-treatment (**Fig 2-6E**), suggesting adaptation of the autophagy response to long-term inhibition of mTOR complexes. Taken together, rapamycin treatment results in early responses that are concentration-

dependent, with mid-range concentrations resulting in slower responses that evolve as steady state flux through the pathway. These results further signify the importance of measuring all the autophagy rates temporally to capture the complete response.

Given the temporal and concentration-dependent behavior of autophagy, we wanted to develop a simple metric for measuring the total amount of autophagy processed until steady state conditions are reached. We measured the area under the curve (AUC) for R_3. Assuming the average cargo captured and degraded are the same for each condition, this measure would indicate the total amount of cargo completely degraded through the autophagic pathway. For example, perturbations such as rapamycin that induce autophagic flux would have higher AUC while perturbations that inhibit autophagy initiation or clearance would have low AUC. Using the R_3 temporal data spanning 15 h, we calculated the AUC for basal and all rapamycin treatments (**Fig 2-6F**). While 0.1 nM rapamycin was indistinguishable from the basal condition, all other rapamycin concentrations lead to significantly higher AUC, indicating higher autophagic flux. Intriguingly, all rapamycin concentrations above 0.1 nM degraded similar amounts of cargo. These results were consistent with the observed slow response for the mid-range concentration (0.5 and 1 nM) and a faster but shorter response for higher concentrations (10 and 100 nM) as discussed earlier. Henceforth, this measurement can be used as an additional metric to track the total amount of autophagy perturbed.

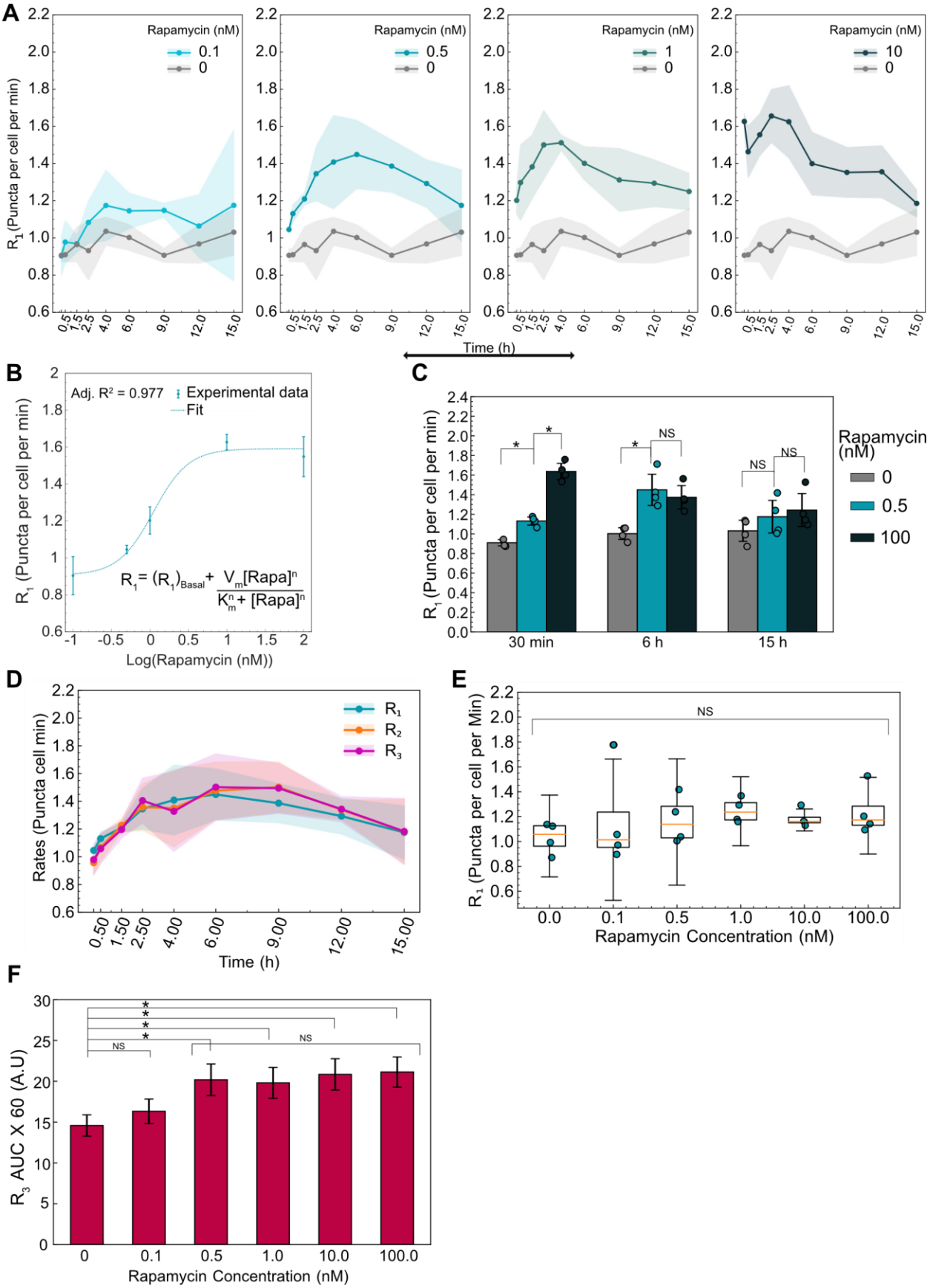
A
Rapamycin (nM)
0.1
0
0.5
1
10
R1 (Puncta per cell per min)
Time (h)
B
Adj. R² = 0.977
Experimental data
Fit
R1 = (R1)Basal + Vm[Rapa]n / Kmn + [Rapa]n
R1 (Puncta per cell per min)
Log(Rapamycin (nM))
C
R1 (Puncta per cell per min)
Rapamycin (nM)
0
0.5
100
30 min
6 h
15 h
NS
D
R1
R2
R3
Rates (Puncta cell min)
Time (h)
E
R1 (Puncta per cell per Min)
NS
Rapamycin Concentration (nM)
F
R3 AUC X 60 (A.U)
NS
Rapamycin Concentration (nM)

Figure 2-6. Initial and time evolution of autophagy rates depend on rapamycin concentration. (**A**) Temporal dynamics of R_1 for different concentrations of rapamycin. Data points represent the mean while shaded area represents $\pm$ standard deviation. Four independent replicates were performed. (**B**) R_1 at 10 min after rapamycin addition is plotted as a function of rapamycin concentration. Individual data points represent experimental data while the dotted line represents the model fit. The model used for fitting the data along with the adjusted R^2 value is also shown. (**C**) Statistical comparison of R_1 for three different rapamycin concentrations at three different time points. (*) indicates p-value < 0.05 and NS indicates not significant. P-values were calculated using an independent two-tail t-test. (**D**) Temporal evolution of all autophagic rates (R_1, R_2, R_3) for 0.5 nM rapamycin-treated cells. Data points represent the mean while the shaded area represents $\pm$ standard deviation. (**E**) R_1 at 15 h as a function of rapamycin concentration. NS indicates not significant. P-values were calculated using a one-way ANOVA test. (**F**) AUC for R_3 data for different concentrations of rapamycin. Data represent mean $\pm$ standard deviation. P-values were calculated using a one-way ANOVA test followed by Tukey's post hoc test for pairwise comparison. At least 150-200 cells were imaged for all experiments.

Wortmannin temporarily inhibits basal and rapamycin-induced autophagosome formation.

After validating our non-steady state approach using an autophagy inducer, we next set out to test the method using wortmannin, a commonly used inhibitor of autophagosome formation [18,19]. We used 1 μM wortmannin to test its ability to inhibit basal and rapamycin-induced autophagy. First, we measured the autophagosome and autolysosome temporal dynamics after treating with wortmannin and/or rapamycin (**Fig 2-7A and 2-7B**). We observed an immediate decrease in the autophagosome numbers for wortmannin, as well as wortmannin with rapamycin-treated conditions, while the autolysosome numbers remained constant. Surprisingly, after 30 min, we observed an increase in the autophagosome numbers in cells treated with wortmannin only and a combination of wortmannin with rapamycin. Moreover, the rate of increase in autophagosome number for wortmannin with rapamycin-treated cells was faster than just wortmannin-treated cells. The autophagosomes for wortmannin with rapamycin reached initial levels by 1 h and kept increasing to saturate at a higher level than basal (~1.8 fold) by 6 h, followed by a slight downward trend by 15 h. Wortmannin-only treatment took 3.5-4 h for autophagosome numbers to reach the initial level and saturated at a slightly higher level (~1.3 fold). For autolysosomes, we observed a higher accumulation for wortmannin with rapamycin treatment

(~1.5 fold) compared to just wortmannin (~1.1 fold), similar to the autophagosome behavior. We used 100 nM rapamycin and basal (DMSO) as controls and their behavior remained the same as in earlier experiments. From the known inhibitor mechanism of wortmannin, we hypothesize the initial drop in autophagosomes is a result of the inhibition of R_1. However, the increase after 30 min could either be a result of an increase in R_1 or a much lower decrease in R_2 and R_3 compared to R_1 or a combination of both. Rates for each step is needed to uncover the dynamics involved.

We used the non-steady state method discussed earlier to measure the individual rates following wortmannin treatment. At 10 min, we observed an immediate decrease in the R_1 while R_2 and R_3 remained at the basal level for wortmannin-treated cells, confirming the known inhibitory mechanism of action of wortmannin (**Fig 2-7C-E**). Moreover, R_1 for wortmannin with rapamycin was also significantly lower at 10 min compared to basal and rapamycin treatments (**Fig 2-7C and F**). Therefore, wortmannin initially inhibits basal as well as rapamycin-induced autophagosome formation. R_2 and R_3 decreased by 30 min due to the lack of autophagosomes to degrade because of decreased R_1 (**Fig 2-7D and E**). Interestingly, R_1 increased over time following initial inhibition by wortmannin. Wortmannin is less stable in cell culture media and could be the major reason for recovery after wortmannin treatment [20]. However, the possibility of feedback cannot be completely ruled out. R_2 and R_3 follow a similar trend as R_1 after 30 min with a slight delay (**Fig A-5A and B**). This indicates that the behavior is mainly driven by R_1 and the downstream flow of autophagosomes through the pathway is unperturbed. Rapamycin and basal rate behaviors were consistent with the previous results (**Fig 2-7C- E**)**.**

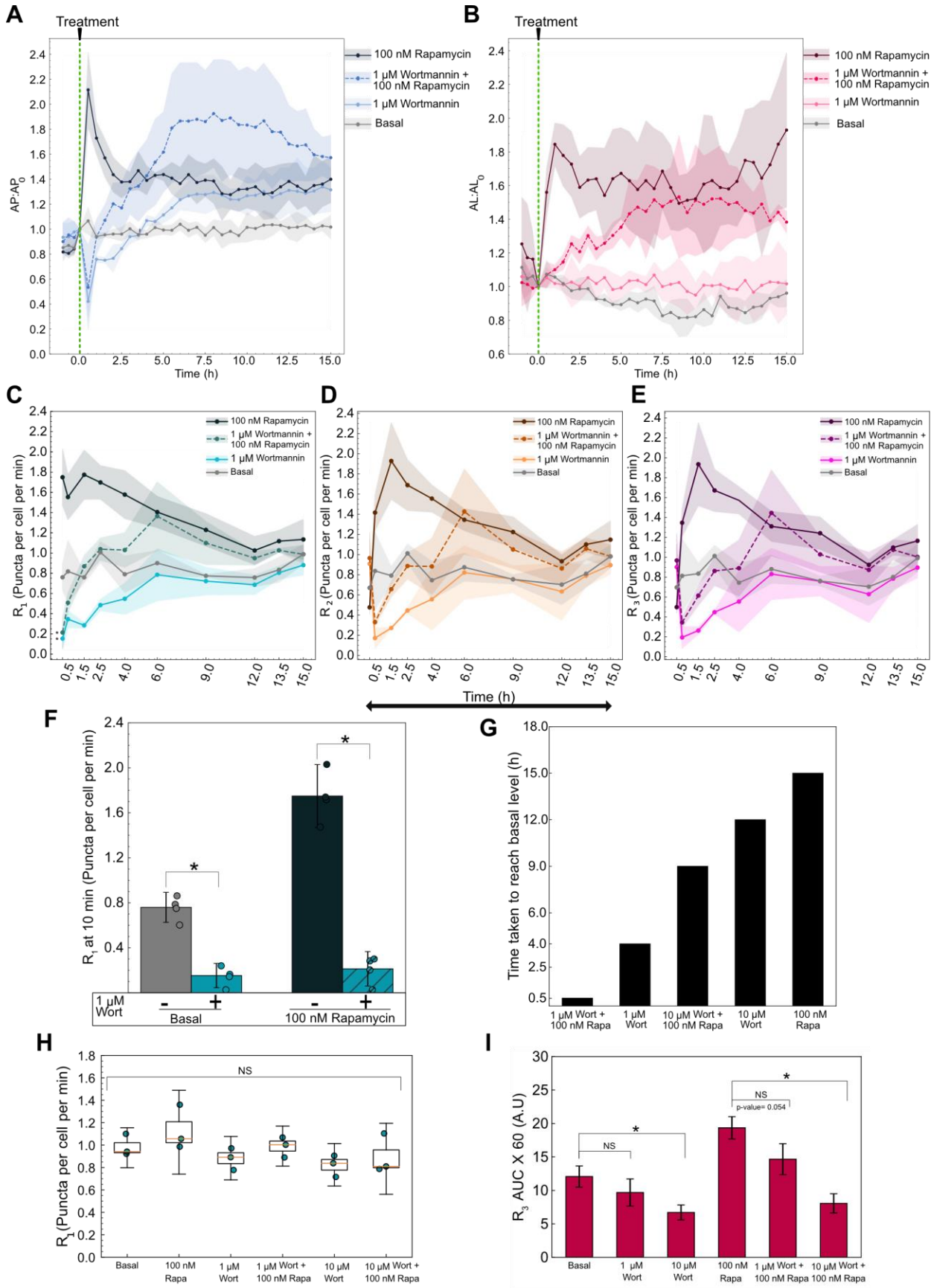
A
Treatment
AP:AP0
Time (h)
100 nM Rapamycin
1 μM Wortmannin + 100 nM Rapamycin
1 μM Wortmannin
Basal
B
Treatment
AL:AL0
Time (h)
C
R1 (Puncta per cell per min)
D
R2 (Puncta per cell per min)
E
R3 (Puncta per cell per min)
Time (h)
F
R1 at 10 min (Puncta per cell per min)
1 μM Wort
Basal
100 nM Rapamycin
G
Time taken to reach basal level (h)
1 μM Wort + 100 nM Rapa
1 μM Wort
10 μM Wort + 100 nM Rapa
10 μM Wort
100 nM Rapa
H
R1(Puncta per cell per min)
NS
Basal
100 nM Rapa
1 μM Wort
1 μM Wort + 100 nM Rapa
10 μM Wort
10 μM Wort + 100 nM Rapa
I
R3 AUC X 60 (A.U)
NS
p-value= 0.054
Basal
1 μM Wort
10 μM Wort
100 nM Rapa
1 μM Wort + 100 nM Rapa
10 μM Wort + 100 nM Rapa

Figure 2-7. Variable autophagy recovery time from wortmannin's inhibition.(**A**) Autophagosome and (**B**) autolysosome number dynamics after treatment. The indicated concentration of small molecule was added at 0 min. The number of autophagosomes and autolysosomes at 0 min was used as the normalization factor. Data points represent the mean while the shaded area represents $\pm$ standard deviation. Three independent replicates were performed. (**C**) R_1 (**D**) R_2 (**E**) R_3 temporal dynamics for basal, 1 µM wortmannin (Wort) with and without 100 nM rapamycin (Rapa), and 100 nM rapamycin alone. Data points represent the mean while the shaded area represents $\pm$ standard deviation. Three independent replicates were performed. (*) indicates p-value < 0.05, p-values were calculated using an independent two-tail t-test. (**F**) Statistical comparison of R_1 at 10 min for different treatments. (*) indicates p-value < 0.05, p-values were calculated using an independent two-tail t-test. (**G**) Time taken for R_1 of each treatment condition to reach the basal level. (**H**) R_1 at 15 h plotted as a function of treatment condition. NS indicates not significant. p-values were calculated using a one-way ANOVA test. (**I**) AUC for R_3 for different treatments. P-values were calculated using a one-way ANOVA test followed by Tukey's post hoc test for pairwise comparison. (*) indicates p-value < 0.05 and NS indicates not significant. At least 150-200 cells were imaged for all experiments.

We tested a higher wortmannin concentration (10 µM) to probe if it plays a role in the recovery of R_1 (**Fig A-5C-E**). We analyzed the time taken for R_1 to reach back to a statistically insignificant level as basal and potentially exceed it (**Fig 2-7G**). A treatment of 1 µM wortmannin reached basal level by 4 h while 10 µM wortmannin took approximately 12 h, suggesting wortmannin's concentration is a governing factor. Moreover, we observed a faster recovery of wortmannin with rapamycin-treated cells. For 1 µM wortmannin, cells also treated with rapamycin reached basal level by 30 min compared to 4 h for wortmannin alone. Similarly, for 10 µM wortmannin, the cells with rapamycin took 9 h compared to 12 h with wortmannin alone. The accelerated recovery of rapamycin-treated cells could be due to the additional autophagosome induction capacity of rapamycin.

We next analyzed the final steady state rates and the total cargo degraded in terms of R_3 AUC over 15 h. At 15 h, the rates of all treatment conditions were indistinguishable from each other as well as the basal condition (**Fig 2-7H**). This result reemphasizes the importance of temporal monitoring of autophagy, as rapamycin and wortmannin, which have opposing effects on autophagosome formation, reach the same final steady state. Finally, using the R_3 data collected

over 15 h, we calculated the AUC for 1 µM and 10 µM wortmannin treatment conditions (**Fig 2-7I**). We anticipated a decrease in the overall cargo degraded as wortmannin inhibited the initiation of autophagosome formation and thus reduced the overall flux through the pathway. We did not observe a significant decrease in the overall cargo degraded for 1 µM wortmannin treatment compared to basal but did for 10 µM wortmannin treatment. For cells treated with wortmannin along with rapamycin, 1 µM wortmannin caused a clear decrease in cargo degraded compared to the rapamycin sample even though it did not meet our statistical criteria (p-value= 0.0542). Conversely, rapamycin with 10 µM wortmannin treatment significantly decreased the cargo degraded compared to rapamycin-induced conditions. These results are consistent with the faster recovery of autophagy under 1 µM wortmannin treatment compared to 10 µM. These measurements can be utilized to further guide the precise tuning of autophagy.

As these observations were made using a single A549- pHluorin-mKate2-LC3 clone, we tested the behavior of bulk sorted A549-pHluorin-mKate2-LC3 cells. We measured the change in autophagosome and autolysosome dynamics as well as the rates for 100 nM rapamycin and 1 µM Wortmannin treatment. The overall behavior of the bulk sorted cells was similar to that of the individual clone which was used for all the measurements (**Fig A-6A-E**), indicating the clone's behavior is representative of the general A549 cell line. To further confirm that the method is expandable to other cell lines, we developed a bulk sorted U2OS-pHluorin-mKate2-LC3 cell line. A similar analysis was performed on U2OS cells and parallel behaviors were observed between U2OS and A549 cell lines under rapamycin and wortmannin treatment (**Fig A-6F-J**). There was substantial variation in the amount of LC3 expressed among the bulk sorted cells, which could be the main reason for the variation observed in the data. Finer optimization of the sorting process for selecting similar expressing populations could mitigate such variability.

Serum and glutamine starvation regulate autophagosome dynamics on different timescales.

Serum starvation and nutrient deprivation regulate autophagy in many biological systems such as cancer and bioproduction [21,22]. We tested the dynamic autophagy response to serum starvation, glutamine starvation, and a combination of both in our clonal A549 cell line. Under normal conditions, cells were stably cultured at 8% fetal bovine serum (FBS) and 4 mM glutamine concentration. Cells were imaged for 1 h before diluting the FBS and glutamine concentration to 0.64% and 0.32 mM respectively by serial dilution via repeated partial media replacements. A serial dilution approach was used to minimize the stress induced by replacing the media in the wells and to prevent cells from being completely dry. Nevertheless, due to the high sensitivity of the system, we noticed differences between unperturbed conditions, in which cells were completely undisturbed, compared to the basal control, which involved removing and adding complete media to the cells (**Fig A-7A**).

Serum starvation caused an immediate increase in autophagosome and autolysosome numbers, peaking within two hours followed by a decrease (**Fig 2-8A-B**). Thereafter, the autophagosome numbers stabilized at the initial steady state number, while the autolysosomes saturated at an appreciably lower steady state number (**Fig 2-8A-B**). Conversely, glutamine starvation led to a modest increase in autophagosome number compared to basal fluctuations (**Fig 2-8A**). As discussed previously, the fluctuations in basal can be associated due to the stress induced by the removal and addition of media to cells (**Fig A-7A**). By 20 h we observed a downward trend in the autophagosome numbers for glutamine-starved conditions compared to basal (**Fig 2-8A**). Autolysosomes overall followed similar trends as autophagosomes, with a modest increase followed by a modest decrease (**Fig 2-8B**). For combined serum and glutamine starvation, there was a rapid increase and decrease in autophagosomes and autolysosomes in the first 8 h, similar

to serum starvation (**Fig 2-8A-B)**. We then observed a continuing downward trend in autophagosomes, similar to glutamine starvation (**Fig 2-8A-B**). This suggests that serum starvation may dominate at the initial stages while glutamine starvation comes into effect at a later stage.

Serum and glutamine starvation have opposing impacts on autophagy rates.

To decipher the rate dynamics leading to the observed autophagosomes and autolysosome dynamics, we measured the rates using the non-steady state approach described earlier. Rates were measured from 30 min to 20 h after starvation. An early timepoint was not chosen because the unstarved cells were also stressed initially due to the mixing involved during the change of media (**Fig A-7B-D**). Therefore, all the rates were normalized with the basal condition to account for the stress induced by the exchange of media (**Fig 2-8C-K**). We only observed a significant difference between serum starvation and basal rates at 2 h post starvation, where all rates from serum starvation were higher (**Fig 2-8C-E**). This was consistent with the observed maximum autophagosomes and autolysosome accumulation during that time period. We also observed that the differences among the three rates were minor, indicating that the overall flux was increased at two hours post starvation with minimal lag. After two hours, all three rates returned to basal levels.

For glutamine starvation, we did not detect a significant difference between basal and glutamine-starved rates until 20 h post starvation (**Fig 2-8F-H**). This was consistent with the observed late response of autophagosome and autolysosome dynamics for glutamine starvation (**Fig 2-8A-B**). We also observed no significant differences between the three rates, indicating that the overall flux decreased at 20 h post starvation.

For both glutamine and serum starvation, we observed a significant increase in all the rates at two hours, similar to serum starvation alone, while at 20 h we observed a significant decrease in all three rates, similar to glutamine starvation alone (**Fig 2-8I-K**).

Although significant, we only observed minor differences between the three rates at two hours, suggesting an increase in overall flux with minor lag. At 20 h, there was no significant difference among the three rates, indicating that the overall flux decreased relative to the basal flux at a longer time period. As hypothesized earlier, this behavior corroborates the observed autophagosome and autolysosome dynamics and highlights the different timescales of glutamine and serum starvation responses. In summary, these results suggest that serum starvation transiently induces autophagy flux on a short time scale while glutamine starvation inhibits autophagy flux on a longer time scale.

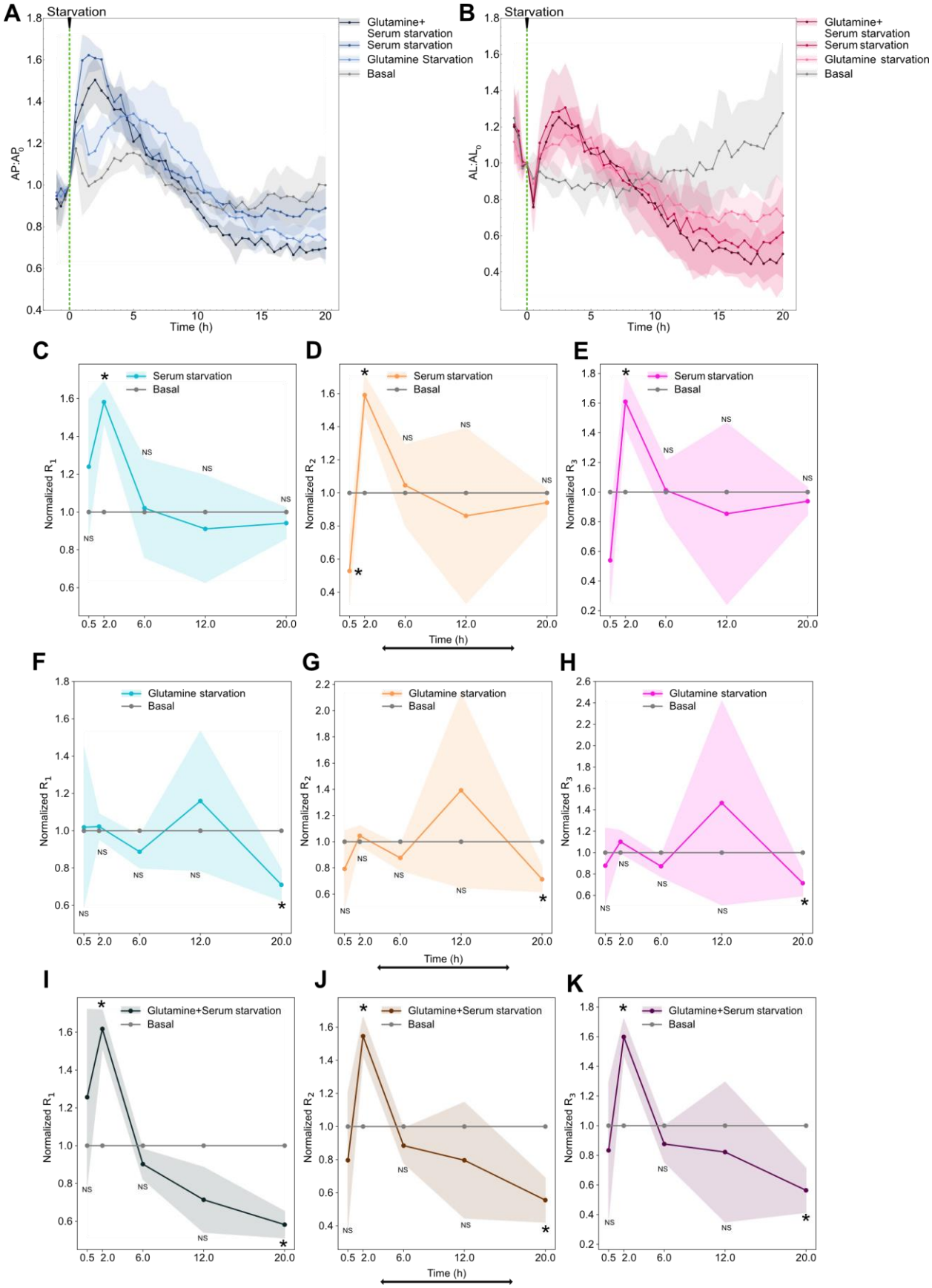
A
Starvation
Glutamine+ Serum starvation
Serum starvation
Glutamine Starvation
Basal
AP:AP0
Time (h)
B
Starvation
Glutamine+ Serum starvation
Serum starvation
Glutamine starvation
Basal
AL:AL0
Time (h)
C
D
E
Serum starvation
Basal
Normalized R1
Normalized R2
Normalized R3
Time (h)
F
G
H
Glutamine starvation
Basal
Normalized R1
Normalized R2
Normalized R3
Time (h)
I
J
K
Glutamine+Serum starvation
Basal
Normalized R1
Normalized R2
Normalized R3
Time (h)
NS
*

Figure 2-8. Serum starvation induces autophagy flux while glutamine starvation inhibits autophagy flux.(A) Autophagosome and (B) autolysosome number dynamics under starvation conditions. Normal media was removed partially and media with no serum or no glutamine or both were added at 0 min to dilute the concentration. The number of autophagosomes and autolysosomes at 0 min was used as the normalization factor. Data points represent the mean while shaded area represents $\pm$ standard deviation. Three independent replicates were performed. Normalized (C) R_1 (D) R_2 (E) R_3 temporal dynamics of serum-starved with respect to basal. Basal line at one is provided for reference. Normalized (F) R_1 (G) R_2 (H) R_3 temporal dynamics for glutamine-starved with respect to basal. Normalized (I) R_1 (J) R_2 (K) R_3 temporal dynamics for glutamine + serum-starved with respect to basal. Data points represent the mean while the shaded area represents $\pm$ standard deviation. Three technical replicates were performed. Statistical comparisons between various starvation conditions and basal rates at every time point were made using an independent two-tail t-test. (*) indicates p-value < 0.05 and NS indicated not significant. At least 150-200 cells were imaged for all experiments.

Serum addition to serum-starved cells transiently inhibits autophagy flux.

Given the faster response to serum starvation, we added back serum to the serum-starved cells at 20 h post-starvation to observe the dynamics. Serum-starved cells that were replenished with serum immediately decreased autophagosome numbers within 30 min while the continuously serum-starved cells remained at the same level (**Fig 2-9A**). Lower levels of autophagosomes were observed for 3-4 h after replenishment followed by an increase of autophagosomes to the basal level **(Fig 2-9A)**. The autolysosome numbers had a slower response to serum replenishment (**Fig 2-9B**). These observations suggest that serum is an inhibitor of autophagy flux, which could be confirmed by rate measurements.

We measured the rates after serum addition at 21, 25, and 30 h (1, 5, and 10 h post-serum addback, respectively). We observe lower rates for serum addback cells compared to serum-starved cells at 21 h. After 21 h, the rates recover to reach the basal level at 25 and 30 h (**Fig 2-9C-E**). As all three rates reach the same level by 21 h, we measured the rates immediately (10 min) after adding back serum to capture the latency in decrease among R_1, R_2, and R_3. Even though not significant, we observe a considerable decrease in R_1 immediately compared to R_2 and R_3 after the serum is added back compared to cells that continue in serum-starved conditions

(**Fig 2-9F**). Overall, these results indicate serum transiently inhibits autophagy flux, with an initial latency in R_2 and R_3 responses.

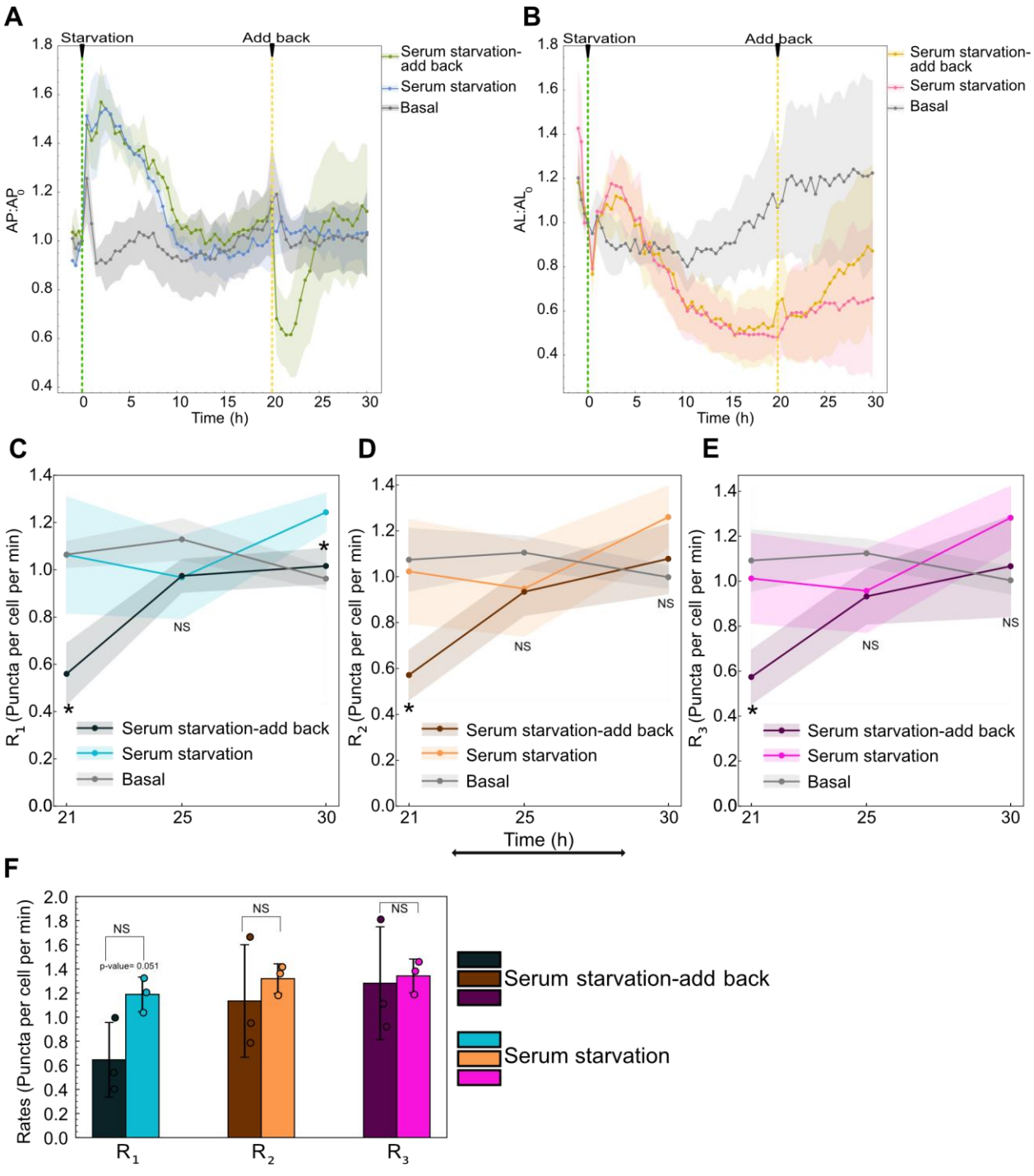

Figure 2-9. Serum addback to serum-starved cells transiently inhibits autophagy flux.(A) Autophagosome and (B) autolysosome number dynamics under continued serum-starved, serum-starved with serum replenishment at 20 h, and basal. The number of autophagosomes and autolysosomes at 0 min was used

as the normalization factor. Data points represent the mean while the shaded area represents ± standard deviation. Three independent replicates were performed. Combined serum and glutamine starvation data are plotted on all the plots to facilitate comparison (E) R_1 (F) R_2 (G) R_3 temporal dynamics for basal, serum-starved, and serum-starved after serum replenishment at 20 h. Data points represent mean while the shaded area represents ± standard deviation. Three independent replicates were performed. Independent two-tail t-test was used to compare statistical significance between serum-starved with no replenishment and serum-starved with replenishment. (*) indicates p-value < 0.05. (H) Comparison of R_1 R_2, and R_3 after 10 min of serum addback to serum-starved cells compared to continued serum-starved cells. Bar graphs represent the mean while the error bars represent ± standard deviation. Three technical replicates were performed. (*) indicates p-value < 0.05, p-values were calculated using an independent two-tail t-test. At least 150-200 cells were imaged for all experiments.

Conclusion and Discussion

Quantitatively measuring all the autophagic steps remains a significant challenge and is key to developing better autophagy-based applications. This is especially critical for developing autophagy-based therapies, where dysfunction of cellular pathways is disease- and environment-specific, leading to a variable response to the same treatment. Therefore, it is crucial to systematically characterize the disease state, kind of perturbation (for example, inducer or inhibitor) as well as the cellular response to gain a comprehensive understanding. Moreover, since autophagy is a dynamic process, it is pivotal to temporally monitor the process to capture the complete dynamic response until a steady state is reached. These measurements will be essential in informing the overall change in the autophagic state after a perturbation, the feedback mechanisms involved, and their timescales. For example, this information will assist in developing combinatorial therapies for effectively modulating autophagy to treat diseases with finer control and minimal side effects [23,24].

We present a method to quantify autophagy rates in live cells. Previous studies have quantified the rate of autophagosome production under steady state conditions [1,4,25]. We expand on these studies by creating a theoretical and experimental framework to measure autophagy rates for all three steps in the autophagy pathway under non-steady state conditions. We do so by

monitoring autophagosome and autolysosome numbers before and after inhibition of autophagosome-lysosome fusion. When combined with the instantaneous rate approach it enables measurement of all three autophagy rates without the requirement of them being equal.

By measuring autophagy rates under non-steady state conditions for rapamycin, we were able to validate our system using a well-characterized inducer of autophagy. We observed concentration-dependent increases in initial rates of autophagosome formation. These results were consistent with previous studies measuring autophagy flux [26,27] and rapamycin's well-established mode of action upstream of phagophore formation. We also observed an overall return to basal autophagy rates, consistent with previous indirect observations [28]. These results are indicative of long-term feedback mechanisms at play. Importantly, our approach enables measuring initial rates with high time resolution (~10 min), which can uncover the direct mode of action of an autophagy perturbation, before long-term feedback mechanisms convolute measurements.

The non-steady state approach also revealed novel insights into the mechanisms regulating the cellular response to rapamycin. We uncovered temporal responses to high concentrations of rapamycin that could be explained by a hybrid model of regulation of autophagy rates. Latency in the rates of autolysosome formation and degradation revealed rate-limiting steps leading to autophagosome accumulation at very early time points. Moreover, we have also shown the latency in the fusion step is not due to a limited number of lysosomes, and future efforts to dissect mechanisms of latency could be leveraged to overcome them. Probing for the fusion governing proteins that may be rate limiting can be valuable for elucidating the fundamental mechanism involved as well as for developing new targets to inhibit the fusion step. At later time points, feedback mechanisms lowered the overall flux through the pathway. Understanding the timeline

of feedback mechanisms for additional perturbations could help refine control over autophagy. Conversely, low concentrations of rapamycin treatment led to a slower but steady response in rates. We hypothesize this behavior is due to the complex interplay between multiple feedback mechanisms of MTORC1 [29,30]. Using these measurements in conjunction with fluorescent protein activity reporters at a single cell level can elucidate the complex dynamics involved [31,32] and will be important to dissect in the future. The temporal nature of this new approach also enabled the development of a new metric in the form of overall cargo degraded (AUC for R_3) which can be used as an additional property to characterize the system. This result underlines the dynamic nature of the pathway and the significance of this metric to fine-tune the flux through the pathway. In the future, it will also be interesting to determine if autophagy-associated diseases are due to a general reduction in degradative capacity (AUC for R_3), or defects in the degradation of specific cargo.

We also measured rates for wortmannin to demonstrate the universality of this method to different types of perturbations. We observed concentration-dependent effects as well as a differential rate of recovery from wortmannin inhibition. This information can be used for modeling the system and extracting parameters such as half-maximal concentration, degradation constants, and maximal induction capacity. Additionally, this information can also be used to probe for the feedback mechanisms involved and their specific pathways. For example, if there is a MTORC1 independent feedback mechanism involved in the increase of R_1 after wortmannin inhibition, the addition of rapamycin after recovery would lead to a higher R_1 value and vice versa. Future work can be focused on extracting system parameters to develop a predictive model using the current data and some additional experimentation.

To validate the behavior observed beyond a single clone and cell line, we tested the dynamics of bulk A549 and U2OS cells for rapamycin and wortmannin treatment. The overall behavior of bulk cells was similar to that of the single clone and consistent across cell lines. Therefore, this method can also be used to characterize different cell lines about the inherent basal state and their response to perturbations and makes measurements in unique cancer and neurodegenerative disease models a possibility. However, various parameters, such as the variability in the amount of fluorescent LC3 protein expressed in each line need to be carefully assessed before drawing such comparisons.

We expanded our analysis to physiological conditions such as serum and glutamine starvation. Serum starvation transiently upregulated autophagy flux while adding back serum almost immediately inhibited autophagy flux, indicating, that serum inhibits autophagy. Conversely, glutamine starvation inhibited autophagy flux on a longer time scale indicating glutamine is required for autophagy. Our observations were consistent with previously reported findings [33,34]. However, the measurements were noisier compared to chemical perturbations. One important reason for this could be the significant cell to cell variability observed under these starvation conditions, especially glutamine starvation (data not shown). Single-cell measurements could alleviate these limitations and could provide interesting new findings.

While our method enables novel measurements of autophagy rates, expanding its use will require improvements in autophagy-related tools. For example, our current approach uses fluorescent proteins to monitor autophagosome and autolysosome numbers and is thus limited to engineered cells. Performing similar experiments with live-cell organelle dyes could overcome this limitation. This would enable autophagy rate measurements in difficult-to-engineer cells, and open the door

to measurements in patient-derived cells [35,36]. Possible applications include precision medicine for autophagy-related diseases such as cancer and neurodegeneration [37,38]. Moreover, expanding such measurements to *in vivo* systems is vital for clinical translation [39].

In conclusion, our work demonstrates quantitative measurement of rates for all three steps in the autophagy pathway under non-steady state conditions. This study revealed novel mechanisms of regulation for rapamycin induction of autophagy and differential temporal kinetics of wortmannin's inhibition. In the future, these approaches could be applied to uncover mechanisms of action for novel autophagy-regulating compounds, develop predictive models, and characterize unique responses based on cellular genetic background. Moreover, integration with other live cell measurements would create a quantitative and holistic picture of autophagy as it connects to other cellular pathways.

Materials and Methods

Cell culture and media

A549 cells (ATCC, CCL-185) and U2OS cells (ATCC, HTB-96) were used for autophagy experiments. HEK 293T cells (ATCC, CRL-11268) were used for lentivirus packaging. Cells were cultured in a humidified incubator at 37°C and 5% CO_2. All cell lines were maintained in DMEM (Gibco, 11965118) supplemented with 8% fetal bovine serum (FBS [Gibco, 10438-026]). U2OS cells were also cultured with 1% penicillin-streptomycin (Gibco, 15070063). For live-cell imaging, A549 cells were cultured in FluoroBrite DMEM (Gibco, A1896701) supplemented with 8% FBS and 4 mM of GlutaMAX (Gibco, 35050061). U2OS reporter cells were cultured in the same imaging media along with 1% penicillin-streptomycin (Gibco, 15070063).

Reporter cell line construction

The FUGW-PK-hLC3 lentivirus was used to develop A549 and U2OS reporter cell lines. Lentivirus was packaged in HEK 293Ts in 6-well format as previously described [40]. The harvested lentivirus media was stored at -80°C until further use. A549 and U2OS cells were plated overnight at a density of 0.1 million cells per well in a 24-well plate. The media was replaced with lentivirus-containing media. After an hour, the lentivirus media was replaced with fresh media, and the cells were scaled up upon reaching confluency. For bulk populations, A549 and U2OS cells positive for pHluorin and mKate2 signal were sorted using a Beckman Coulter “Astrios EQ”:18-Color cell sorter. For clonal selection, transduced A549 cells were sorted into individual cells into a 96-well plate using a Beckman Coulter “Astrios EQ”:18-Color cell sorter. Each clone population was scaled up upon reaching confluency. A single clone population was used for most experiments to decrease noise arising from different integration sites. FUGW-PK-hLC3 ΔG reporter cell line was also developed using the same approach. FUGW-PK-hLC3 and FUGW-PK-hLC3 ΔG were gifts from Isei Tanida (Addgene, 61460; http://n2t.net/addgene:61460; RRID: Addgene_61460; Addgene, 61461; http://n2t.net/addgene:61461; RRID: Addgene_61461, respectively).

Chemical treatments

Bafilomycin A_1 (Selleck Chemicals, S1413), rapamycin (Selleck Chemicals, S1039), and wortmannin (Selleck Chemicals, S2758) were used for treating the cells. For measuring rates, 500 nM bafilomycin A_1 was added along with a final concentration of 0.2 µg/mL Hoechst 33342 trihydrochloride solution (Hoechst 33342 [Invitrogen, H3570]) to ensure proper mixing. All basal conditions were treated with DMSO (Sigma Aldrich, 472301).

Starvation conditions

A549 reporter cells were stably cultured in FluoroBrite DMEM (Gibco, A1896701) supplemented with 8% FBS and 4 mM of GlutaMAX (Gibco, 35050061) for 12-16 h before the experiment in a 96 well plate. Each well contained a culture volume of 100 µL. To initiate starvation conditions, 60 µL of media were removed and 160 µL of FluoroBrite DMEM containing either containing 8% FBS or 4 mM GlutaMAX or neither was added to the wells. After mixing, 160 µL of the media were removed from the wells and an additional 60 µL of FluoroBrite DMEM containing either 8% FBS or 4 mM GlutaMAX or neither was added to the wells. Therefore, leading to a 12.5-fold dilution. For addback experiments, FBS was added back to wells to bring back the serum levels to 8%. The same volume of FBS starved media and full media was added to continued serum-starved and basal wells, respectively.

Live cell microscopy

All reporter cell lines were seeded in 96-well glass-bottom plates with #1.5 cover glass (Cellvis, P96-1.5H-N). A549 cells were directly plated while U2OS cells were plated after treating the 96-well plate with collagen solution (Gibco, A1048301) to increase cell adherence. Live cell imaging was performed using Nikon Ti2 inverted microscope with an okolab stage top incubator to maintain 37°C and 5% CO_2. Cells were plated at approximately 1.7 X 10^4 cells per well for 12-18 h prior to performing the experiment. A total of 4-5 positions were imaged in each well at the indicated time using the NIS-Elements AR software. A549 reporter cell line and A549 bulk sorted cells for all chemical treatment experiments were imaged at 25% LED intensity and 200 ms exposure for GFP channel and at 30% LED intensity and 350 ms for TRITC channel images. U2OS reporter cells and A549 reporter clonal cell line for starvation experiments were imaged at 35% LED intensity and 200 ms exposure for GFP channel and at 45% LED intensity and 350 ms for TRITC channel images. Images were acquired using CFI PLAN APO LAMBDA 40X CF160

Plan Apochromat Lambda 40X objective lens, N.A. 0.95, W.D. 0.17-0.25mm, F.O.V. 25mm, DIC, Correction collar 0.11-0.23 mm, Spring Loaded, and using Andor Zyla VSC-08688 camera.

Immunofluorescence

A549s were seeded in a 96-well glass-bottom plate. Cells were treated with either DMSO or 100 nM rapamycin for indicated times. After treatment, 100% ice-cold methanol (Fisher Scientific, A412-4) was added to the cells and were incubated for 20 min at -20°C. After aspirating methanol, cells were rinsed thrice with 1X DPBS (Gibco, 21600069) solution for 5 min each. Following DPBS wash, cells were incubated with 5% goat serum (Sigma Aldrich, G9023) in 1X DPBS with 0.3% Triton™ X-100 (Fischer Scientific, BP151-100) for an hour. After aspirating the serum solution, cells were incubated with 1:600 anti-LAMP1 primary antibody solution (LAMP1 [D2D11] XP rabbit mAb [Cell Signaling Technology, 9091], 1X DPBS, 1% bovine serum albumin [BSA; Sigma Aldrich, 126609], 0.3% Triton™ X-100) overnight. After removing the primary antibody solution, cells were rinsed thrice with 1X DPBS solution. After rinsing, cells were incubated with secondary antibody solution (1:1000 goat anti-rabbit IgG H+L] Alexa flour 488 [Invitrogen™, A-11008], 1:5000 Hoechst 33342 in 1% BSA in 1X DPBS with 0.3% Triton™ X-100) for an hour in the dark. Finally, cells were washed thrice with 1X DPBS solution for 5 min each before imaging. Each condition at each time point had three replicates. The average number of LAMP1 positive puncta from the triplicates was used as one biological replicate value. The experiment was repeated four times independently.

Immunofluorescence microscopy

After fixation, cells were imaged using Nikon Ti2 inverted microscope. LAMP1 positive puncta and nuclear staining were imaged using the green channel (GFP) and blue channel (DAPI),

respectively. GFP images were acquired at 25% LED intensity and 200 ms exposure. DAPI images were acquired at 15% LED intensity and 75 ms exposure settings. Images were acquired using CFI PLAN APO LAMBDA 40X CF160 Plan Apochromat Lambda 40X objective lens, N.A. 0.95, W.D. 0.17-0.25mm, F.O.V. 25mm, DIC, Correction collar 0.11-0.23 mm, Spring Loaded, and using Andor Zyla VSC-08688 camera.

Western blot

Cells (80,000 per well) were plated in a 12-well plate overnight. The next day, cells were treated with DMSO or 100 nM rapamycin for different time points. Bafilomycin A_1 (500 nM) was added to the cells for 2 h at different timepoints for measuring LC3 accumulation. At the specific time point, the media in the wells was aspirated and the cells are quickly rinsed using 1X DPBS. Cells were then lysed with RIPA buffer (150 mM sodium chloride [NaCl; Fischer Scientific, S271], 50 mM Tris, pH 8 [Fischer Scientific, BP152], 1% Triton X-100 [Fisher Scientific, BP151-100], 0.1% sodium dodecyl sulfate [Fischer Scientific, BP166-500], 0.5% sodium deoxycholate [Sigma Aldrich, D6750]) containing protease inhibitors (Thermo Scientific™, A32955). The lysed cells in RIPA buffer were incubated on ice for 30 min. After 30 min, the samples were centrifuged at 16128 x g for 20 min, after which the supernatant of the samples was collected and stored at -20°C. Sample protein content was normalized using the Pierce™ BCA protein assay kit (Thermo Scientific™, 23225). LDS (Invitrogen™, NP0007) and TCEP (Thermo Scientific™, 77720) in 4:1 ratio was then added to the normalized samples and were heated in a thermocycler for 10 min at 95°C. The samples were then run on an SDS gel containing 4% stacking and 15% resolving gel compartments. The proteins were resolved at 115 volts for 15 min initially followed by 150 volts for an hour. The proteins were then transferred onto methanol-activated Amersham Hybond P 0.2 PVDF membrane (Cytiva, 10600021) at 150 volts for an hour. The membrane is then reactivated using methanol and quickly rinsed in distilled water. After reactivation, the membrane

is blocked using 5% milk in TBS-T buffer (Tris-Buffered Saline pH 7.6 [TBS; 20 mM Tris, pH 8, 150 mM NaCl, hydrochloric acid [Sigma Aldrich, 320331] with 0.1% Tween- 20 [Fischer Scientific, BP337-100]) solution for an hour. The membrane slices were then incubated in their respective primary antibody diluted in 2.5% BSA in TBS-T solution overnight with gentle agitation. The antibody dilution for each antibody is as follows, 1: 1000 anti- phopho-RPS6/S6 ribosomal protein (Ser240/244; D68F8) rabbit mAb (Cell Signaling Technology, 5364), 1:1000 anti-RPS6/S6 ribosomal protein (5G10) rabbit mAb (Cell Signaling Technology, 2217), 1:1000 anti- LC3B (D11) XP rabbit mAb (Cell Signaling Technology, 3868), and 1:1000 anti-GAPDH (14C10) rabbit mAb (Cell Signaling Technology, 2118). Following primary antibody incubation, the membrane was rinsed thrice with TBS-T solution for 5 min each. The membrane was then incubated with 1:5000 goat anti-rabbit IgG-HRP (SouthernBiotech, 4030-05) secondary antibody in 5% Milk TBS-T solution. The membrane was washed twice with TBS-T followed by a TBS wash. Finally, the membrane was incubated with ECL western blotting substrate (Thermo Scientific^{TM}, 32109) for 5 min before acquiring images. Amersham Imager 600 system (GE Healthcare) was used for imaging.

Image processing for live cell imaging

NIS-Elements AR software was used for extracting autophagosomes and autolysosome puncta numbers. GFP and TRITC channel images were processed and analyzed using the General analysis job functionality in the NIS-Elements AR software. Both GFP and TRITC channel images were background corrected using the rolling ball correction method with a radius of 1.95 μm. Following background correction, Spot Detection functionality was used for thresholding and detecting puncta in both channels. GFP channel images were used for estimating autophagosome puncta numbers as the green signal is only detected in autophagosomes. Bright-clustered detection method in the Spot Detection tool was used for detecting circular areas in the

GFP channel with a typical spot diameter of 0.8 μm and a minimum contrast value of 5. The contrast value acts as a thresholding parameter to only detect puncta whose difference between mean intensity inside and mean intensity outside the spot is higher than the contrast value provided. Similarly, for the TRITC channel, 0.8 μm was used as the typical spot diameter and 7.5 was used as the contrast value. A higher contrast value was used for detecting puncta in the TRITC channel because of the lower signal-to-noise ratio and thus to minimize false positive puncta. However, the puncta from the TRITC channel includes both autophagosomes as well as autolysosomes count as both have a red signal. Therefore, to extract autolysosome-only count, we compared the colocalization of puncta in GFP and TRITC channels using the AND binary operation. The number of colocalized puncta (representing autophagosomes) were then subtracted from the total TRITC puncta, thus providing the autolysosome count. All the other parameters in the spot detection tool were left as default. The puncta detection accuracy was confirmed through manual inspection of multiple images under various conditions (untreated, rapamycin and bafilomycin A_1 treatment). Post analysis, the autolysosome and autophagosome count for each image were exported as a spreadsheet.

Cellpose was used for counting cells in each image [41]. The ND2 files were converted to RGB tif files and the GFP channel images were used for segmenting and extracting the cell count. Cellpose was implemented in Python 3.7 using a custom script and 120 was used as the diameter input for segmenting individual cells. The segmentation accuracy was confirmed by manual inspection as well as by comparing with Hoechst-based nucleus count.

After extracting the cell, autophagosome and autolysosome count from each position imaged in a well. The total number of autophagosomes and autolysosomes in all the positions imaged were

added and was divided by the total number of cells providing a population level autophagosome and autolysosome count per cell. This analysis was done using a custom script in MATLAB.

Image processing for immunofluorescence microscopy

LAMP1-positive puncta in fixed samples were estimated using spot detection tool in NIS-Elements AR software. A radius of 0.8 µm and a contrast value of 10 was used for detecting LAMP1-positive puncta. Similarly, the number of cells was estimated using the spot detection tool on the nuclear stain with a typical diameter of 15 µm and a contrast value of 1.5 as parameters.

Data fitting and area under the curve estimation

Curve fitting toolbox in MATLAB was used to fit the data. Custom equations were provided for fitting the data and the Nonlinear least squares method was used for the fit. Trapz function in MATLAB was used for calculating the area under the curve and a custom script was used for propagating the error.

Statistical analysis

At least 150-200 cells were imaged for all experiments. A minimum of three experimental replicates was performed for all the quantitative experiments. Independent t-test, paired t-test, and one-way ANOVA were used as indicated for comparing statistical significance for various experiments. All statistical tests were performed in Python 3.8 using the SciPy package. ANOVA along with Tukey post hoc test for AUC calculations was performed using a webpage (https://statpages.info/anova1sm.html). Box and whisker plots indicate the median value as an

orange line, interquartile range (IQR) as a box, and range $[Q_1 - 1.5 * IQR, Q_3 + 1.5 * IQR]$ as whiskers.

References

[1] Loos B, Du Toit A, Hofmeyr JHS. Defining and measuring autophagosome flux - Concept and reality. Autophagy. 2014;10:2087–2096.

[2] du Toit A, Hofmeyr JHS, Gniadek TJ, et al. Measuring autophagosome flux. Autophagy. 2018;14:1060–1071.

[3] Fass E, Shvets E, Degani I, et al. Microtubules support production of starvation-induced autophagosomes but not their targeting and fusion with lysosomes. J Biol Chem [Internet]. 2006;281:36303–36316. Available from: http://dx.doi.org/10.1074/jbc.M607031200.

[4] Klionsky DJ, Abdel-Aziz AK, Abdelfatah S, et al. Guidelines for the use and interpretation of assays for monitoring autophagy (4th edition)1. Autophagy. 2021;17:1–382.

[5] Zhou C, Zhong W, Zhou J, et al. Monitoring autophagic flux by an improved tandem fluorescent-tagged LC3 (mTagRFP-mWasabi-LC3) reveals that high-dose rapamycin impairs autophagic flux in cancer cells. 2012 [cited 2021 Oct 29]; Available from: https://www.tandfonline.com/action/journalInformation?journalCode=kaup20http://dx.doi.org/10.4161/auto.20284.

[6] Pankiv S, Clausen TH, Lamark T, et al. p62/SQSTM1 binds directly to Atg8/LC3 to facilitate degradation of ubiquitinated protein aggregates by autophagy*[S]. J Biol Chem. 2007;282:24131–24145.

[7] Tanida I, Ueno T, Uchiyama Y. Use of pHlurorin-mKate2-human LC3 to Monitor Autophagic Responses [Internet]. 1st ed. Methods Enzymol. Elsevier Inc.; 2017. Available from:

http://dx.doi.org/10.1016/bs.mie.2016.09.054.

[8] Tanida I, Ueno T, Uchiyama Y. A Super-Ecliptic , pHluorin-mKate2 , Tandem Fluorescent Protein-Tagged Human LC3 for the Monitoring of Mammalian Autophagy. 2014;9:3–10.

[9] Tanida I, Ueno T, Kominami E. Human Light Chain 3 / MAP1LC3B Is Cleaved at Its Carboxyl-terminal Met 121 to Expose Gly 120 for Lipidation and Targeting to Autophagosomal Membranes *. 2004;279:47704–47710.

[10] Kabeya Y, Mizushima N, Ueno T, et al. LC3 , a mammalian homologue of yeast Apg8p , is localized in autophagosome membranes after processing. 2000;19.

[11] Yamamoto1 A, Tagawa1 Y, Yoshimori2 T, et al. Bafilomycin Ai Prevents Maturation of Autophagic Vacuoles by Inhibiting Fusion between Autophagosomesand Lysosomesin Rat HepatomaCell Line, H-4-II-E Cells. CELL Struct. Funct. 1998.

[12] Rubinsztein DC, Gestwicki JE, Murphy LO, et al. Potential therapeutic applications of autophagy. 2007 [cited 2021 Oct 8]; Available from: www.nature.com/reviews/drugdisc.

[13] Klionsky DJ, Elazar Z, Seglen PO, et al. Does bafilomycin A1 block the fusion of autophagosomes with lysosomes? Autophagy. 2008;4:849–850.

[14] Brown EJ, Albers MW, Bum Shin T, et al. A mammalian protein targeted by G1-arresting rapamycin-receptor complex. Nature [Internet]. 1994 [cited 2021 Jun 13];369:756–758. Available from: https://www.nature.com/articles/369756a0.

[15] Sabatini DM, Erdjument-Bromage H, Lui M, et al. RAFT1: A mammalian protein that binds to FKBP12 in a rapamycin-dependent fashion and is homologous to yeast TORs. Cell [Internet]. 1994 [cited 2021 Jun 13];78:35–43. Available from: http://www.cell.com/article/0092867494905703/fulltext.

[16] Sabersu CJ, Martinl1 MM, Brunnj GJ, et al. THE JOURNAL OF BIOLOGICAL CHEMISTRY

Isolation of a Protein Target of the FKBP12-Rapamycin Complex in Mammalian Cells*. 1995.

[17] Goutelle S, Maurin M, Rougier F, et al. The Hill equation: A review of its capabilities in pharmacological modelling [Internet]. Fundam. Clin. Pharmacol. Blackwell Publishing Ltd; 2008 [cited 2021 Jun 13]. p. 633–648. Available from: https://onlinelibrary.wiley.com/doi/full/10.1111/j.1472-8206.2008.00633.x.

[18] Blommaart EFC;, Krause P;, Schellens JPM;, et al. UvA-DARE (Digital Academic Repository) The phosphatidylinositol 3-kinase inhibitors wortmannin and LY294002 inhibit autophagy in isolated rat hepatocytes. 1997 [cited 2021 Sep 30]; Available from: https://doi.org/10.1111/j.1432-1033.1997.0240a.x.

[19] Petiot A, Ogier-Denis E, Blommaart EFC, et al. Distinct Classes of Phosphatidylinositol 3â€^{2}-Kinases Are Involved in Signaling Pathways That Control Macroautophagy in HT-29 Cells*. J Biol Chem [Internet]. 2000 [cited 2021 Sep 30];275:992–998. Available from: http://www.jbc.org.

[20] Ihle NT, Williams R, Chow S, et al. Molecular pharmacology and antitumor activity of PX-866, a novel inhibitor of phosphoinositide-3-kinase signaling. Mol Cancer Ther [Internet]. 2004 [cited 2022 Jun 8];3:763–772. Available from: https://aacrjournals.org/mct/article/3/7/763/278215/Molecular-pharmacology-and-antitumor-activity-of.

[21] Altman BJ, Stine ZE, Dang C V. From Krebs to clinic: glutamine metabolism to cancer therapy. Nat Rev Cancer 2016 1610 [Internet]. 2016 [cited 2022 Jun 8];16:619–634. Available from: https://www.nature.com/articles/nrc.2016.71.

[22] Patel DB, Santoro M, Born LJ, et al. Towards rationally designed biomanufacturing of therapeutic extracellular vesicles: impact of the bioproduction microenvironment.

Biotechnol Adv. 2018;36:2051–2059.

[23] Egan DF, Chun MGH, Vamos M, et al. Small Molecule Inhibition of the Autophagy Kinase ULK1 and Identification of ULK1 Substrates. Mol Cell. 2015;59:285–297.

[24] Liu T, Zhang J, Li K, et al. Combination of an Autophagy Inducer and an Autophagy Inhibitor: A Smarter Strategy Emerging in Cancer Therapy. Front Pharmacol. 2020;11:408.

[25] du Toit A, Hofmeyr JHS, Gniadek TJ, et al. Measuring autophagosome flux. Autophagy [Internet]. 2018;14:1060–1071. Available from: https://doi.org/10.1080/15548627.2018.1469590.

[26] Decuypere J, Kindt D, Luyten T, et al. mTOR-Controlled Autophagy Requires Intracellular Ca 2 + Signaling. 2013;8.

[27] de Wet S, Du Toit A, Loos B. Spermidine and Rapamycin Reveal Distinct Autophagy Flux Response and Cargo Receptor Clearance Profile. Cells. 2021;10.

[28] de Wet S, Du Toit A, Loos B. Spermidine and Rapamycin Reveal Distinct Autophagy Flux Response and Cargo Receptor Clearance Profile. Cells [Internet]. 2021 [cited 2021 Jun 13];10. Available from: https://pubmed.ncbi.nlm.nih.gov/33430464/.

[29] Gonzá Lez A, Hall MN, Lin S-C, et al. Cell Metabolism Review AMPK and TOR: The Yin and Yang of Cellular Nutrient Sensing and Growth Control. Cell Metab [Internet]. 2020 [cited 2021 Oct 22];31:472–492. Available from: https://doi.org/10.1016/j.cmet.2020.01.015.

[30] Dunlop EA, Tee AR. The kinase triad, AMPK, mTORC1 and ULK1, maintains energy and nutrient homoeostasis. Biochem Soc Trans [Internet]. 2013 [cited 2021 Oct 22];41:939–943. Available from: /biochemsoctrans/article/41/4/939/67121/The-kinase-triad-AMPK-mTORC1-and-ULK1-maintains.

[31] Zhou X, Clister TL, Lowry PR, et al. Dynamic Visualization of mTORC1 Activity in Living Cells. Cell Rep [Internet]. 2015;10:1767–1777. Available from: http://dx.doi.org/10.1016/j.celrep.2015.02.031.

[32] Konagaya Y, Terai K, Hirao Y, et al. A Highly Sensitive FRET Biosensor for AMPK Exhibits Heterogeneous AMPK Responses among Cells and Organs. Cell Rep [Internet]. 2017;21:2628–2638. Available from: https://doi.org/10.1016/j.celrep.2017.10.113.

[33] Sakiyama T, Musch MW, Ropeleski MJ, et al. Glutamine Increases Autophagy Under Basal and Stressed Conditions in Intestinal Epithelial Cells. Gastroenterology. 2009;136:924-932.e2.

[34] Chen R, Zou Y, Mao D, et al. The general amino acid control pathway regulates mTOR and autophagy during serum/glutamine starvation. J Cell Biol [Internet]. 2014 [cited 2022 Jun 8];206:173. Available from: /pmc/articles/PMC4107793/.

[35] Martínez-Pizarro A, Desviat LR, Ugarte M, et al. Endoplasmic reticulum stress and autophagy in homocystinuria patients with remethylation defects. PLoS One [Internet]. 2016 [cited 2021 Jun 16];11:e0150357. Available from: https://journals.plos.org/plosone/article?id=10.1371/journal.pone.0150357.

[36] Mohammadi A, Kelly OB, Filice M, et al. Differential Expression of microRNAs in Peripheral Blood Mononuclear Cells Identifies Autophagy and TGF-Beta-Related Signatures Aberrantly Expressed in Inflammatory Bowel Disease. J Crohn's Colitis [Internet]. 2018 [cited 2021 Jun 16];568–581. Available from: https://www.

[37] Levy JMM, Towers CG, Thorburn A. Targeting autophagy in cancer. Nat. Rev. Cancer. Nature Publishing Group; 2017. p. 528–542.

[38] Scrivo A, Bourdenx M, Pampliega O, et al. Selective autophagy as a potential therapeutic

target for neurodegenerative disorders. 2018.

[39] Loos B, Klionsky DJ, Toit A Du, et al. On the relevance of precision autophagy flux control in vivo – Points of departure for clinical translation for clinical translation. Autophagy [Internet]. 2020;16:750–762. Available from: https://doi.org/10.1080/15548627.2019.1687211.

[40] Minami SA, Shah PS. Transient light-activated gene expression in Chinese hamster ovary cells. BMC Biotechnol [Internet]. 2021 [cited 2021 Jun 13];21:13. Available from: https://link.springer.com/articles/10.1186/s12896-021-00670-1.

[41] Stringer C, Wang T, Michaelos M, et al. Cellpose: a generalist algorithm for cellular segmentation. Nat Methods [Internet]. 2021 [cited 2021 Jun 13];18:100–106. Available from: https://doi.org/10.1038/s41592-020-01018-x.

Chapter 3: *Image-based temporal profiling of autophagy-related phenotypes*

Introduction

The quantitative approach to measure rates discussed in Chapter 2 holds promise for precisely fine-tuning autophagy flux. However, this approach is not easily scalable as it involves destructive sampling. It also does not take advantage of the high-dimensional nature of time-resolved live-cell imaging experiments, in which sub-cellular features can be tracked in single-cell trajectories. Image-based profiling facilitates the simultaneous quantification of various morphological features of sub-cellular components at a single-cell level. Characterization of autophagy-related phenotypes using image-based profiling approaches was performed for various applications such as the identification of small molecule regulators and genetic modulators [1–3]. These studies highlight the potential of using image-based profiling for high-throughput autophagy characterization. However, these studies were performed at a single time point after fixing cells limiting our understanding of dynamic changes in autophagy phenotypes.

To address these challenges, we created a pipeline to systematically characterize temporal changes in autophagy-related morphological phenotypes at a single-cell level. We investigated changes in morphological features under common small molecule autophagy modulators, rapamycin, and wortmannin. We examined the key morphological features that were differentially modulated under various treatments as a function of time. Using a random forest classifier, we identified the features with high importance that can be used to differentiate these treatments. Additionally, we identified novel phenotypes such as increased autophagosome area during rapamycin treatment using this approach. We also used a rudimentary approach to test the possibility of characterizing autophagy regulation based on morphological features. The inclusion of features from various time points after treatment efficiently captured autophagy modulation.

Moreover, we observed that the inclusion of morphological features better-captured autophagy modulation compared to just monitoring autophagy vesicle numbers. This study serves as proof of concept for using image-based profiling to characterize autophagy temporally, which can reveal fundamental insights into autophagy phenotypes and facilitate high-throughput drug characterization.

Results

Experimental setup and image-based profiling pipeline.

We reanalyzed the images to quantity the morphological features that were previously collected [8]. pHluorin-mkate2-LC3 system was used to track autophagosomes and autolysosomes in real-time (**Fig 3-1A**). An illustrative image of the change in morphology after treatment with small molecule drugs is shown in **Figure 3-1B**. Individual autophagosomes (red spots in the pHluorin channel) and autolysosomes (cyan spots in the mKate2 channel) are quantified using the spot detection tool (**Fig 3-1C**). Cellpose was used to segment single cells and generate single-cell masks which were then used to track cells over time using the bTrack algorithm [4,5] (**Fig 3-1D**). The entire pipeline is shown in **Figure B-1.** Along with autophagosome and autolysosome numbers, three main morphological properties were quantified at a single-cell level. Namely, 1) Structural features describing features such as area, major axis length, and Zernike moments [6], 2) Intensity-based features such as mean intensity and minimum intensity, and 3) Texture features quantified using haralick features [7]. These morphological features were quantified for three biological entities- a whole cell level (Cell), autophagosomes (AP), and autolysosomes (AL). Approximately 900 features were quantified at a single-cell level for the entire time course of the experiment.

Temporal profiling of morphological features during small molecule treatment

We characterized morphological changes in cells treated with high concentrations of rapamycin and wortmannin. We previously observed that rapamycin and wortmannin have an opposing effects on autophagy [8]. Rapamycin increased the overall autophagy flux while wortmannin decreased the autophagy for 15 hours when we quantified individual autophagy rates. We identified the features that varied significantly compared to untreated at each time point for both treatments. All features with a median modified Z score of 0.5 and above with an adjusted P-value of lower than 0.05 were considered significant. A representative analysis is shown at 0.5 hours after treatment with wortmannin and rapamycin (**Fig 3-2A-B**). A median value of 0.5 was chosen as a threshold to avoid the inclusion of any noisy false positive features. An identical analysis was performed on the same cells before treatment to confirm that a threshold of 0.5 removes any false positive features (**Fig B-2A-B**).

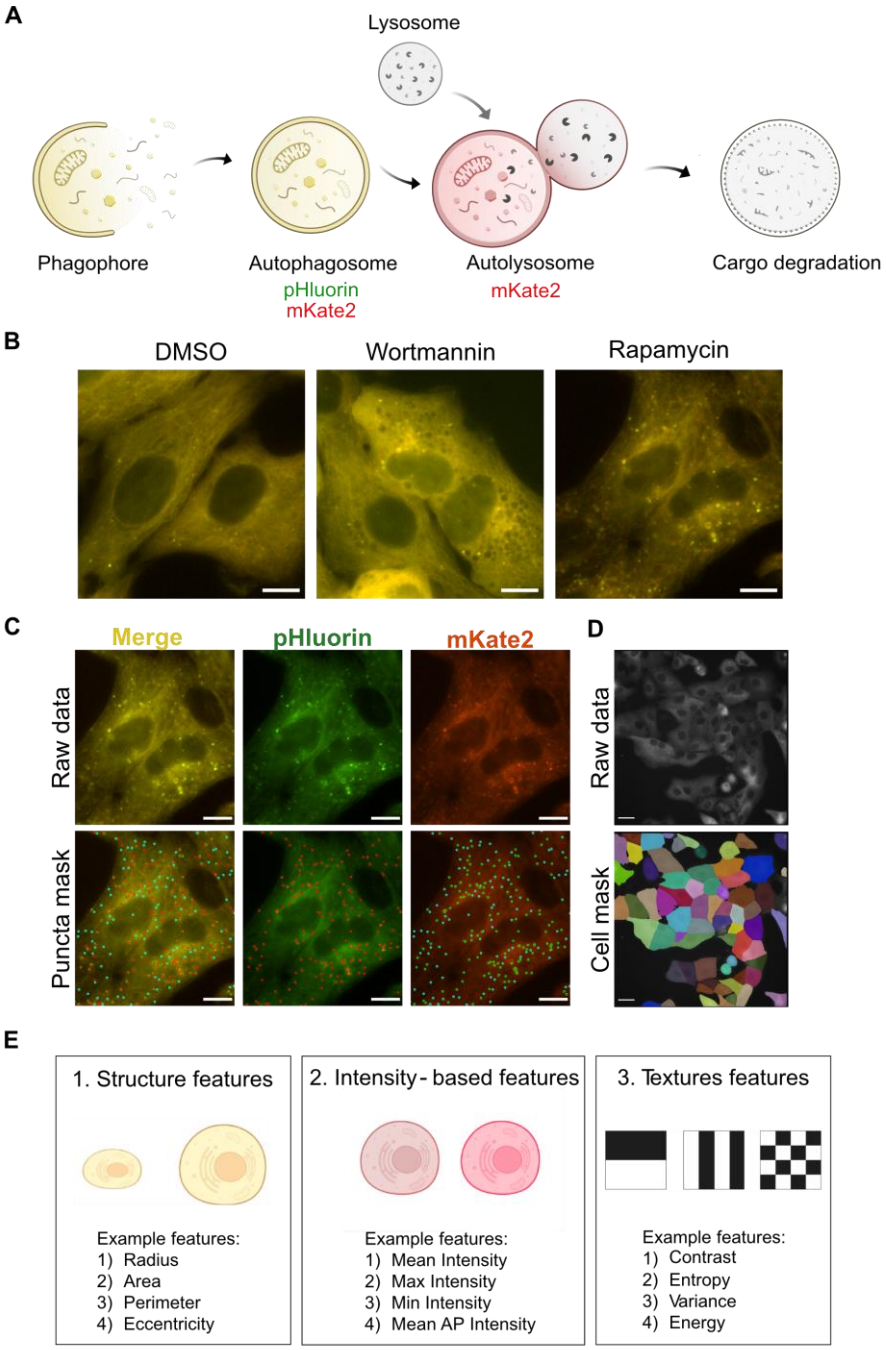

Figure 3-1. Experimental and image analysis pipeline to quantify autophagy-related phenotypes. (**A**) The autophagy pathway and pHluorin-mKate2 were the fluorescent markers used for tracking autophagosomes and autolysosomes. (**B**) Representative images of change in morphology of cells after treatment with 100 nM rapamycin and 10 µM Wortmannin for 6 hours. The scale bar represents 10 µm. (**C**) Representative images of spot detection tool for detecting autophagosomes and autolysosomes. Scale bar represents 10 µm. (**D**) Representative image of segmented cell mask used for tracking individual cells. (**E**) Three main categories of morphological features were extracted at a cellular level as well as an autophagy vesicle level.

We next analyzed the number of features that varied significantly as a function of time. A high number of features varied immediately (30 minutes) after treatment with rapamycin and wortmannin (**Fig 3-2C-D**). This was expected, given the immediate impact of these drugs on cells. We observed a decrease in the number of features after 30 minutes until about 3 hours for wortmannin treatment which stabilized until 6.5 hours. Interestingly, morphological features for rapamycin treatment recovered more drastically after the initial response for 6 hours compared to wortmannin treatment. After 6-7 hours, we observed an increase in the differential features for both treatments. Wortmannin-treated cells remarkably showed few variable features after ~12 hours, indicating that they have returned to the basal state which was consistent with rate measurements made previously [8]. Conversely, rapamycin-treated cells maintained a high number of differential features until 15 hours. Interestingly, autophagic rate dynamics did not necessarily correlate with feature dynamics, since previous measurements demonstrated that rapamycin-treated cells returned to their basal rates [8] even though features remained altered. The sustained morphological changes could indicate that rapamycin is still active and has an impact on cells even though the cells reached a new steady state that is equal to the basal rates. Furthermore, these results signify the importance of characterizing autophagy dynamically to gain a complete understanding of the perturbation.

We next set out to understand the kind of features that were altered. We grouped the features based on two classifications, biological entities, and morphology. Features categorized based on biological entities were divided into cellular (Cell), autophagosomes (AP), and autolysosomes (AL) features. Features based on morphology were classified into intensity, texture, and structure. After separating the variable features into their specific category and timepoint, highly correlated features (except one) were removed to account for redundancy and then normalized to the highest number of features in the respective category to account for the uneven number of

features in each group. This provides insights into the categories that are mainly affected by the treatment.

Wortmannin treatment largely affected cellular and autophagosome features over 15 hours (**Fig 3-2E**). Cellular features were impacted the most for the first 7 hours, after which there was diminishing variability in cellular morphology compared to basal until 15 hours. Interestingly, the majority of the autophagosome features vary between 7-12 hours. Conversely, rapamycin primarily impacted autophagosome features initially compared to cellular and autolysosome features (**Fig 3-2F**). We observed a sharp decrease in autophagosome features until ~4 hours. After 6 hours of rapamycin treatment, the increase in variable features is primarily driven by cellular features and stabilized by 15 hours. Furthermore, we examined the change in morphological features as a function of time for both treatments (**Fig 3-2G-H**). Autophagosome and autolysosome numbers were excluded from this analysis as they are only two biological features that do not fit into any category. Intensity features were impacted at all time points after treatment with wortmannin (**Fig 3-2G**). Several texture features differ uniformly until ~9 hours followed by a decrease in the variability. Variability in structural features peaked between 7-10 hours, which coincides with the peak in differential autophagosome features (**Fig 3-2G**). Conversely, rapamycin affects structural features initially which also coincides with the differential autophagosome features (**Fig 3-2H**). After 4-4.5 hours, we observed an increase in the intensity features which stabilizes by 15 hours. Texture features are mainly impacted at later time points (9- 15 hours) for rapamycin treatment. The minimal effect on autolysosomes was not surprising as both treatments majorly impact upstream autophagosome formation.

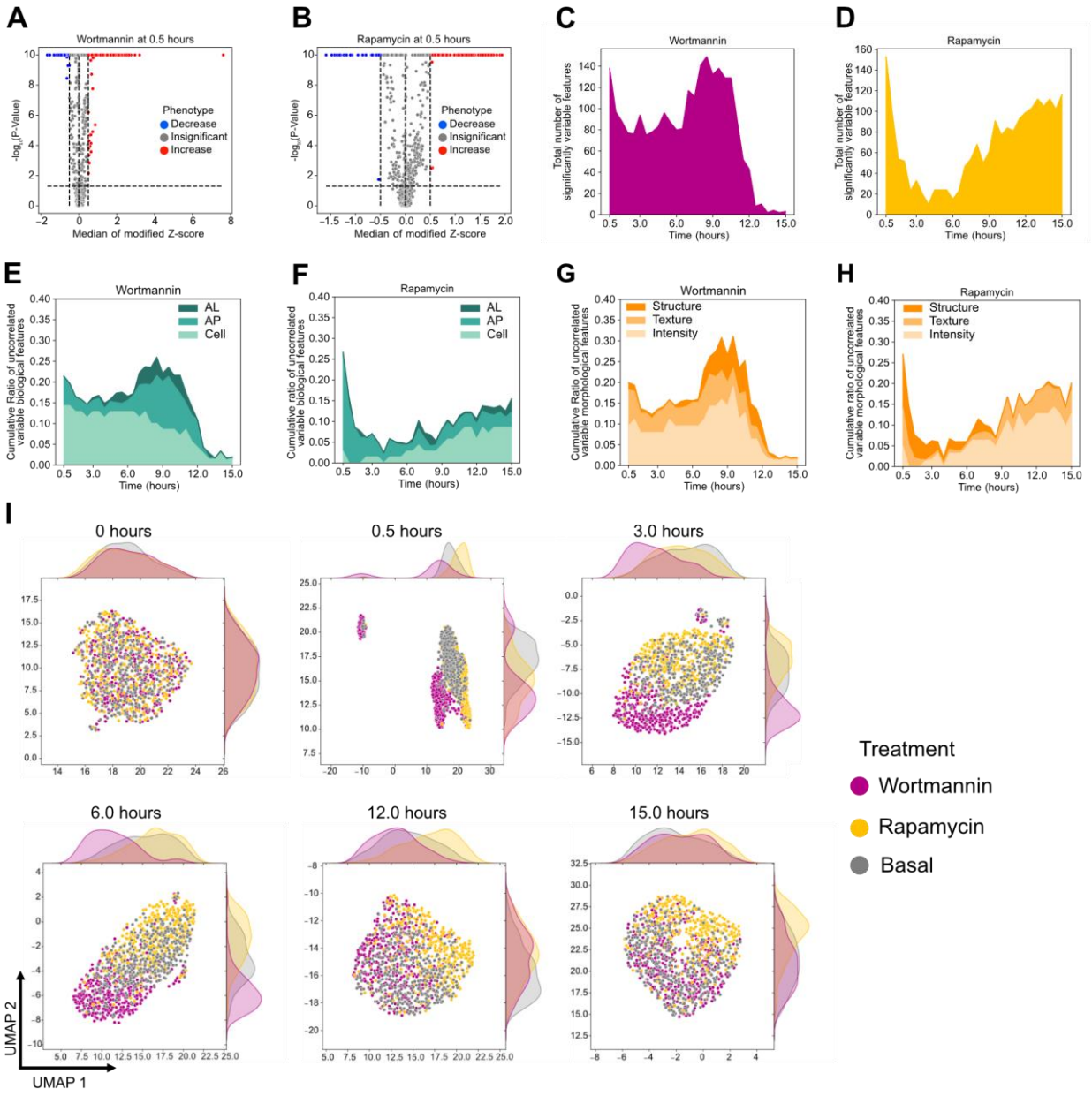

Figure 3-2. Temporal change in morphological features after rapamycin and wortmannin treatment. Volcano plot of cellular features after 30 minutes of treatment with (**A**) 10 µM wortmannin and (**B**) 100 nM rapamycin. Cellular features that varied significantly as a function of time for (**C**) 10 µM wortmannin and (**D**) 100 nM rapamycin. Cumulative ratio of features of biological entities that varied significantly as a function of time after treatment with (**E**) 10 µM wortmannin and (**F**) 100 nM rapamycin, respectively. Cumulative ratio of morphological features that varied significantly as a function of time after treatment with (**G**) 10 µM wortmannin and (**H**) 100 nM rapamycin. (**I**) UMAP of cells treated with DMSO, 100 nM rapamycin, and 10 µM Wortmannin at different time points. UMAP parameters used were neighbors= 250 and mindist=0.90. A minimum of 300 cells were analyzed for each condition. Features that changed significantly and have a median difference of 0.5 with basal were used for generating the UMAPs.

Using dimensionality reduction on all differentially regulated features, we visualized a single cell landscape for basal, wortmannin, and rapamycin treatment at multiple time points (**Fig 3-2I**). There is no distinction between the three treatments at 0 hours, indicating that the cells are indistinguishable before treatment. Immediately after treatment at 30 minutes, we observed a major shift in the clustering of wortmannin and rapamycin-treated cells from basal. Wortmannin caused a more drastic shift at all time points before 12 hours compared to rapamycin. But after 12 hours, the wortmannin-treated cells cluster together with untreated cells which is consistent with the decrease in the differential features at later time points (**Fig 3-2C**). Conversely, rapamycin-treated cells start to segregate again from basal cells beginning at 12 hours and are noticeable at 15 hours. In conclusion, wortmannin impacts cellular morphology reversibly for 15 hours while rapamycin causes a mild but persistent change in morphological features.

Feature importance in classifying rapamycin and wortmannin treatment using random forest classifier.

Identifying governing features of autophagy response to one drug versus another could be a powerful tool for dissection of drug mechanism of action and discovery of new phenotypes. Toward this end, we constructed a random forest model to identify the primary feature set that could be used to differentiate rapamycin and wortmannin treatment from basal and from each other. We aggregated features that changed significantly after the treatment from all time points at a single cell level. We removed features that are linearly correlated with a Pearson correlation of 0.75 and above except the first feature. We used a lower Pearson correlation threshold of 0.75 to remove correlated features as collinearity can considerably affect the feature importance interpretation [9]. Random forest model accuracy was measured using a 5-fold cross-validation method. To elaborate, data were split into 5 folds, where 4 folds were used for training while the remaining fold was used for testing the accuracy of the prediction. We iteratively performed this

step 5 times and calculated the average and standard deviation of the micro F_1 score. The model achieved a F_1 score of 0.89 $\pm$ 0.033 or 89% $\pm$ 3.3%. A representative confusion matrix is shown in **Figure 3-3A**. This random forest classifier was then examined to comprehend the importance associated with each feature in differentiating the treatments using Shapely Additive Explanations (SHAP) values [10]. The importance of each feature is equal to the mean absolute SHAP values for each observation. A higher importance value represents a stronger influence in classifying the treatments. The features were grouped based on the biological object and the morphological feature as discussed earlier. Autophagosome and autolysosome numbers were categorized as vesicle numbers. The feature importance for each group was measured using cumulative importance as well as average importance. Feature importance for each group in classifying wortmannin and rapamycin treatments are shown in **Figure 3-3B-C**, respectively. Autophagosome texture and structure have a high cumulative importance for both treatments. However, it's important to note that these groups contain the major fraction of the features which could contribute to the overall high cumulative value. Vesicle numbers and Cell/Intensity features have a low number of uncorrelated features but contribute majorly towards the classification represented by the average importance. For wortmannin, the Cell/Intensity group has the highest average importance and a higher magnitude compared to other groups, indicating that these features are important in identifying wortmannin treatment (**Fig 3-3B**). For rapamycin treatment, vesicle numbers and Cell/Intensity groups have the highest average importance. Nevertheless, groups such as the AP/Texture also contribute considerably towards the prediction (**Fig 3-3C**). This indicates the rapamycin classification relies on multiple features and is not dominated by a single feature or group.

We next analyzed the top 15 individual features that have the highest feature importance value in classifying the cells into the three treatments (**Fig 3-3D**). The mean intensity of the cell after 0.5 hours is the top feature that contributes towards the differentiation of wortmannin and basal

conditions. The texture of autophagosomes represented by contrast_mean measurement is also a key feature in differentiating wortmannin from basal. Initial autophagosome number and autophagosome structural features such as maximum autophagosome area (max_AP_area) and maximum autophagosome Zernike moment_10 contribute heavily towards the classification of rapamycin treatment.

We generated a 2-dimensional representation of the cellular landscape to understand the impact of these treatment on the features with high importance as a function of time (**Fig 3-3E**). This UMAP for all cells was created using variable features from all time points and a clear segregation of cells based on the treatment can be observed. We visualized mean intensity, autophagosome number, minimum_AP_contrast mean, and max_AP_area for understanding relative change in these features based on treatment and time (**Fig 3-3F**). The mean intensity of the wortmannin-treated cells showed a strong increase after 30 minutes and then decreased over time. The initial increase in mean intensity occurred from reduced clearance of fluorescent LC3 molecules, and as the autophagy rates increase over time, the accumulated LC3 molecules are degraded. On the contrary, rapamycin does not affect mean intensity initially. However, over time we observed a decrease due to the degradation of LC3 molecules. Wortmannin and rapamycin have opposite effects on initial autophagosome numbers. The feature min_AP_contrast_mean, which was a strong indicator of wortmannin treatment, was increased for a major fraction of cells. The max_AP_area feature increased after rapamycin treatment, indicating that bigger autophagosomes are formed after rapamycin treatment, which was confirmed using manual inspection. This analysis helped uncover phenotypes that were previously unknown and illustrated the features that can be used for classifying treatments based on morphological properties. Moreover, we also observed heterogeneity in response to certain features based on the treatment. For example, 30 minutes after wortmannin treatment caused a small portion of

cells to have an opposite response compared to the rest for min_AP_contrast_mean and max_AP_area features. This could be an interesting direction to investigate in the future.

Temporal morphological profiling accurately predicts the dynamic change in autophagy modulation.

We subsequently assessed the predictive value of temporal morphological profiling for characterizing autophagy perturbation and biologically-relevant flux measurements. We used wortmannin and rapamycin treatments as the test case as we characterized this system in detail in our previous study [8]. We tested 6 different conditions – 10 µM Wortmannin (10-W), 1 µM Wortmannin(1-W), 100 nM rapamycin (Rapa), 10 µM Wortmannin with rapamycin (10-WR), and 1 µM Wortmannin with rapamycin (1-WR). Based on our previous autophagy rate measurements, we concluded that rapamycin increases the overall cargo degradation over 15 hours, while wortmannin inhibits cargo degradation. Wortmannin with rapamycin combination initially behaves like wortmannin but induces cargo degradation at later time points. The extent to which cargo degradation is inhibited using wortmannin was dependent on the concentration of wortmannin used.

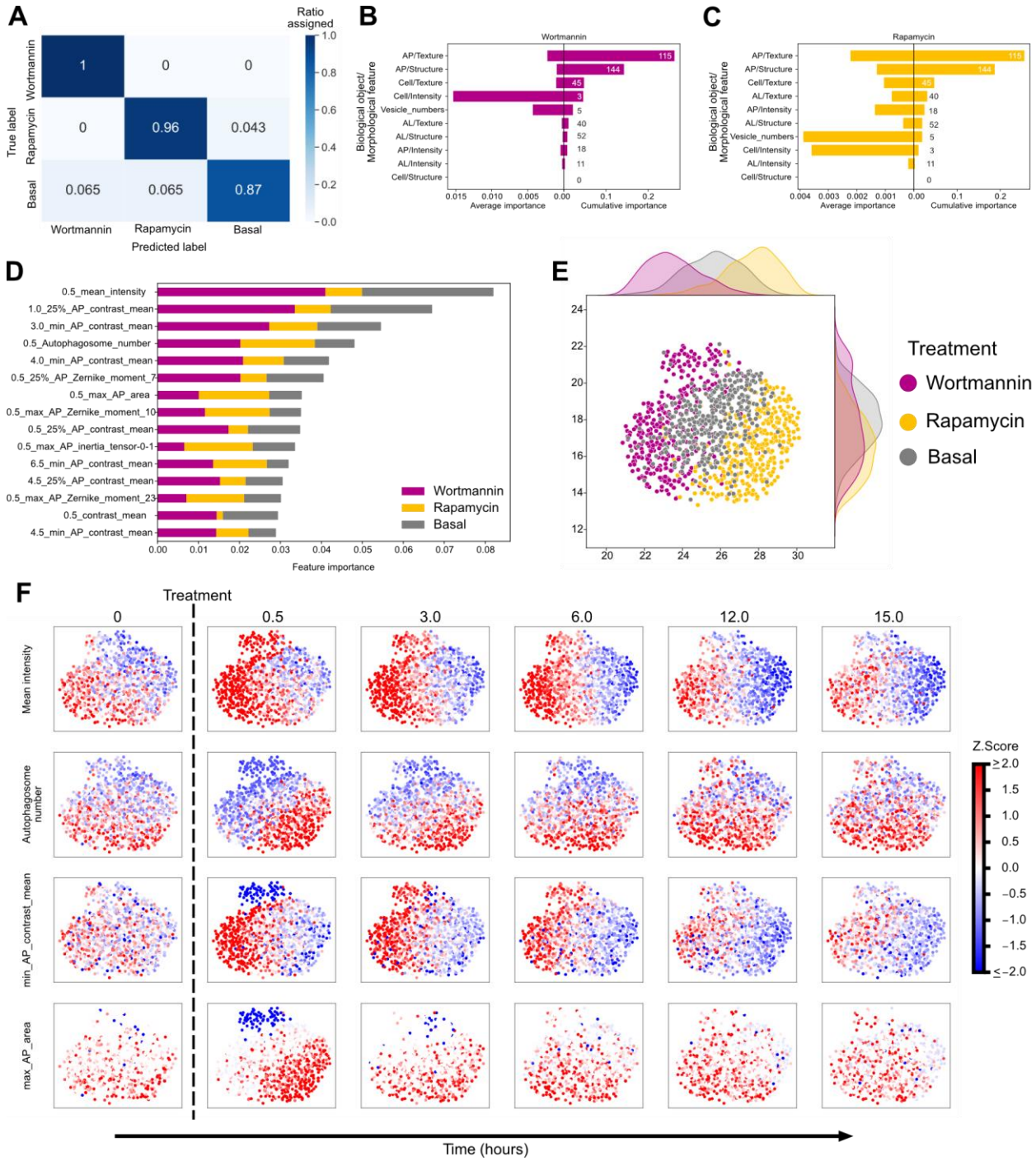

Figure 3-3. Differentiating rapamycin and wortmannin treatment and governing features.(**A**) Confusion matrix to visualize the performance of the random forest model. A minimum of 70 cells for each condition were used for testing the accuracy of the model. (**B-C**) After grouping the features based on biological entity and morphological type, the average and cumulative feature importance were calculated for 10 µM wortmannin and 100 nM rapamycin, respectively. (**D**) The top 15 features with the highest cumulative feature importance for all conditions. (**E)** UMAP of individual cells constructed using variable features from all time points. UMAP parameters used were neighbors= 250 and mindist=0.90 (**F**) Change in feature values at a single cell level as a function of time after treatment with 100 nM rapamycin and 10 µM wortmannin.

We then examined if image-based temporal profiling can accurately capture such complex temporal changes in the autophagy state without the need of measuring autophagy rates using lysosomal inhibitors. To compare the performance, we used the number of autophagosomes and autolysosome temporal data which is traditionally analyzed for estimating autophagy. This would allow us to evaluate the significance of measuring additional morphological features for determining the autophagy state. A very simple profile similarity approach was used for assessing the performance. We first aggregated all the features that varied significantly from basal for all conditions at all time points. In parallel, we used just the number of the autophagosome, and autolysosome features from all time points for comparison. We then performed principal component analysis (PCA) to remove redundancy and performed hierarchical clustering on median profiles. The workflow is shown in **Figure B-3**. Associations identified based on morphological features were different compared to associations identified just based on autophagosome and autolysosome vesicle dynamics (**Fig 3-4A-B**). We compared the profile similarity between drug treatments to quantitatively assess the accuracy of using either of these measurements in capture biologically relevant changes in the autophagy state (**Fig 3-4C-D**). We used rapamycin as our reference treatment to which all other conditions were compared since it had a unidirectional highest induction effect on autophagy. Treatments that affect morphological profiles of cells similar to rapamycin would have a high correlation and vice versa ranging between -1 to 1. We then used the overall cargo degraded for each treatment measured previously as our measurement for overall autophagy perturbed [8]. Overall cargo degraded was used as the standard because it is a single measurement that captures the change in autophagy state temporally. Cargo degraded for each treatment is normalized with cargo degraded during rapamycin treatment (normalized cargo degradation score). Normalizing with rapamycin linearizes the cargo degradation score and bounds the range between 0 and 1. If the treatment affects cargo degradation comparable to rapamycin, the normalized cargo degradation score would be closer to one while higher cargo degradation much lower than rapamycin would lead to

a value closer to zero. We then compared the fit between profile similarity measured by correlation based on image features or just autophagy vesicle numbers to the normalized cargo degradation score (**Fig 3-4E**). We observed a better fit between normalized cargo degradation score and profile similarity measured using image features (R^2= 0.8787) compared to profile similarity measured using just autophagy vesicle count (R^2= 0.6454). Indicating morphological features capture the overall perturbation to the autophagy system more accurately than just measuring autophagosome and autolysosome dynamics. Although simple, this analysis shows the potential of using image-based temporal profiling to accurately evaluate changes in the autophagy state during modulation.

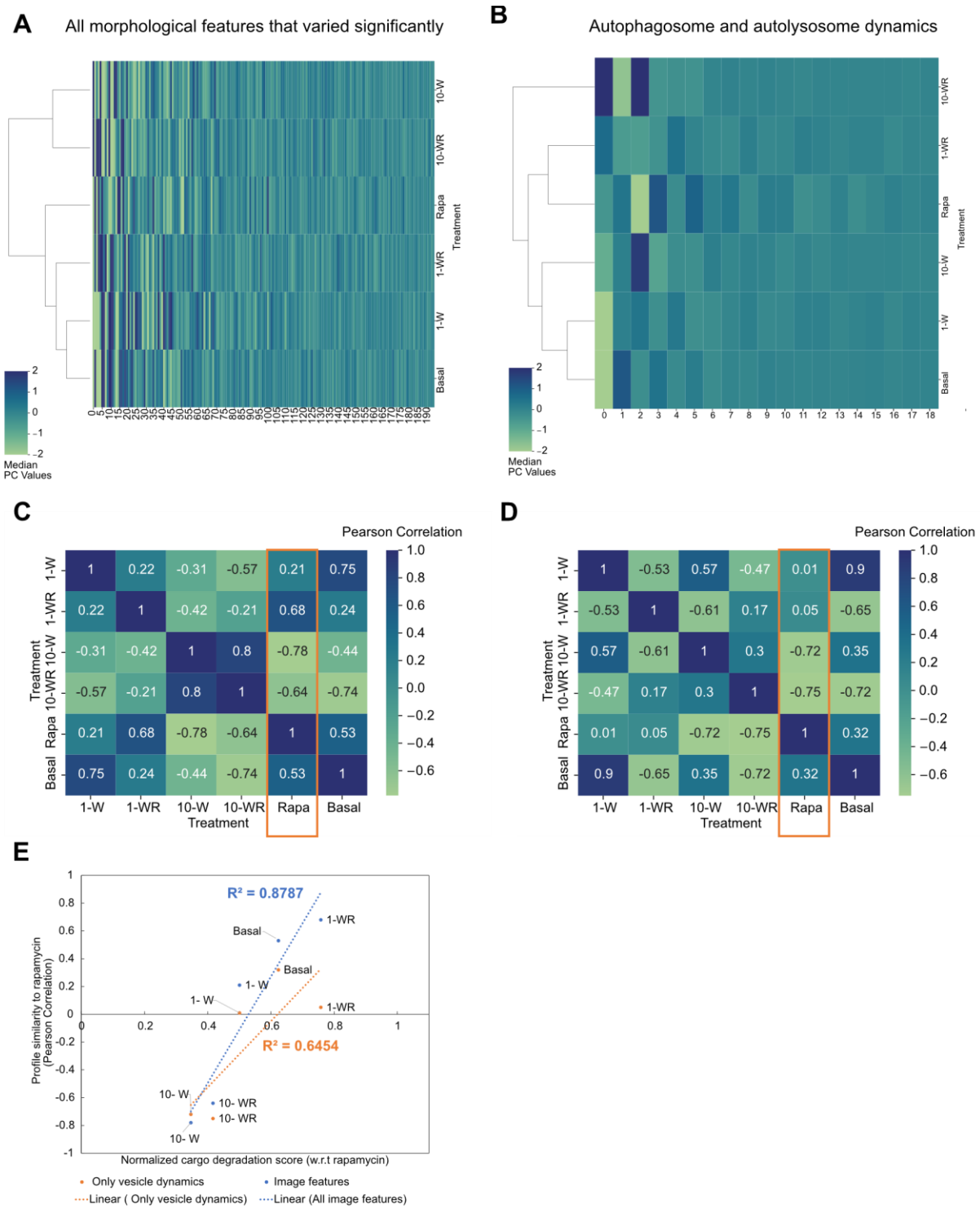

Figure 3-4. Comparing performance accuracy of characterizing autophagy modulation using morphological features vs just autophagy vesicle dynamics. (**A**) Hierarchical clustering of median profiles after principal components analysis (PCA) based on temporal image features. Color bar for heatmap represents median principal component (PC) values. (**B**) Hierarchical clustering based on of median profiles after PCA based on just temporal vesicle numbers. Color bar for heatmap represents median principal component (PC) values. (**C**) Pearson correlation between profiles based on temporal image features. (**D**) Pearson correlation

between profiles based on just temporal vesicle numbers. (**E**) Correlation between profile similarity and normalized cargo degradation score. Abbreviations represent- 10 µM Wortmannin (10-W), 1 µM Wortmannin (1-W), 100 nM rapamycin (Rapa), 10 µM Wortmannin with rapamycin (10-WR), and 1 µM Wortmannin with rapamycin (1-WR).

Discussion

Autophagy is a highly dynamic cellular process that is involved in many diseases. High throughput characterization of autophagy would not only accelerate the screening of new drugs but would enable understanding of the fundamental mechanisms involved. Image-based morphological profiling offers a comprehensive and high-throughput approach for characterizing cellular phenotypes and perturbations.

The dynamic nature and the inclusion of multiple steps in the pathway make measuring autophagy challenging. Methods developed previously can accurately measure each autophagy step with high sensitivity [8,11]. However, these methods rely on lysosomal inhibitors such as bafilomycin A1 to the cells to inhibit autophagosome or autolysosome clearance to make these observations. This perturbs the sample irreversibly and necessitates the requirement of a new sample for measuring the autophagy state at the next time point limiting the scalability. We have performed a proof-of-concept analysis that indicates temporal profiling of morphology can precisely represent the change in autophagy levels. Such approaches will allow high-throughput characterization of perturbations that would allow the screening of drugs and identification of molecular mechanisms. Profile correlation between standard drug (here rapamycin) and the untreated can be used to determine the threshold in identifying the nature of perturbation. For example, we found a correlation of 0.53 between rapamycin and basal profiles. Therefore, 0.53 can be used as a threshold and any treatment with a higher correlation would represent an

autophagy inducer and vice versa. Validating the most promising hits using traditional methods would provide additional confirmation.

Destructive sampling at each time point to probe for the autophagy rates also limits our capability in associating a certain phenotype with the temporal change in the autophagy state at a single cell level. For example, autophagy parameters that govern autophagy-dependent cell death after certain perturbations are not fully understood. This might require monitoring various autophagy parameters such as the change of different rates over time until cell death to derive a correlation between autophagy and cell death which cannot be achieved by using lysosomal inhibitors. Image-based profiling could address these issues by assessing the autophagy state without perturbing the cells. Training models based on morphological profiles and rates to predict rates of autophagy steps as a function of morphological features and time could overcome such challenges.

Comparing the performance of pathway-specific phenotypic characterization to pathway-agnostic phenotypic characterization for drug screening is another interesting route for analysis. To elaborate, autophagy-related phenotypic characterization performed here is a pathway-specific phenotypic characterization approach while assays such as Cell Painting are pathway agnostic [12]. Assays such as Cell Painting offer an unbiased and comprehensive measurement of cellular phenotypes. Such holistic measurements can capture any off-target effects that the drug might have which can be overlooked if a specific pathway is monitored and targeted alone. Conversely, Cell Painting is limited by the temporal resolution it can achieve which might be important for biological processes that are highly dynamic such as autophagy. Therefore, studies comparing

the performance of either method would be useful in understanding the optimal approach for characterizing perturbations.

In this study, we focused on characterizing morphological phenotypes at a bulk level and did not fully leverage the benefits of the single-cell temporal resolution. We observed heterogeneity in multiple features and time points for both rapamycin and wortmannin treatments. Identifying features correlated to the heterogeneity could reveal novel insights. Coupling this of analysis with biosensors can also elucidate biological mechanisms involved in heterogeneity.

Monitoring cargo sequestered such as mitochondria along with autophagy vesicles can provide additional information about the change in morphology of the autophagy vesicles based on cargo sequestered. Identifying morphological markers of autophagy vesicles that correlate with cargo sequestered could lead to the identification of various cargo sequestered by just profiling autophagy vesicles without the need of tagging each cargo. In conclusion, image-based profiling of autophagy is an exciting route that can be explored in various directions which can improve fundamental understanding of the autophagy pathway as well as expedite drug screening for various disease indications.

Materials and Methods

Cell culture, Chemical treatments, and Live cell imaging

Cell culture, generation of the A549-pHluroin-mKate2 reporter cell line, image acquisition for live cell imaging, and chemical treatments using rapamycin, wortmannin, and DMSO were previously discussed [8]. Three individual replicates were performed for collecting data for rapamycin and wortmannin experiments. Third replicate consisted of technical duplicates.

Image analysis, feature extraction and interpretation

Cell masks were generated using the Cellpose algorithm [4]. A custom-trained model was used for extracting cell masks [Available on GitHub]. Individual cells were tracked using the cell masks and bTrack algorithm [5]. Custom-optimized parameters were used as input for btrack [Available on GitHub]. Cell tracking efficiency was confirmed manually for various independent experiments. An example track series is available on GitHub. After the division of a cell, one of the daughter cells continues to have a parent ID and these cells were followed for the entire time course. The other daughter's cell information is discarded. This leads to the loss of immense data and could be improved in the future.

Puncta mask for autophagosomes and autolysosomes are created using a spot detection tool in NIS elements software. Spot detection in different channels was previously elaborated[8]. The main changes to this protocol were 1) the Contrast value for detecting puncta in the TRITC channel was changed to 6. 2) The detected spots were further dilated using Grow Bright regions to Intensity operation to capture different sizes of puncta. 3) Puncta present in GFP and TRITC channels were detected using BOTH= TRITC HAVING (TRITC AND GFP) binary operation. 4)

Only red puncta (autolysosomes) were detected using TRITC SUB BOTH. The general analysis file is available on GitHub. The accuracy of the masks was confirmed manually for cells under various treatment conditions. The total cell count detected using cell masks was also compared to cell count based on nucleus count Hoechst staining. The puncta masks are then subject to the watershed algorithm to differentiate conjoined adjacent puncta. The raw images, cell masks, and puncta masks of cells that are fully tracked are then used for extracting features.

Feature were extracted for three biological entities- Cell as whole, Autophagosome (AP) and autolysosomes (AL). GFP channel images were used for extracting AP and cellular features. For AL, TRITC channel images were used for extracting morphological features. GFP channel images have better signal to noise ratio compared to TRTIC, hence used for extracting cellular features. Cell, AP and AL masks generated as described above were used for feature extraction. Regionprops from skimage.measure was used for extracting some of the features[13]. The mean and range of all 14 Haralick texture features calculated in all directions were included as features. 25 Zernike moments were calculated using 0.5*major_axis_length of the object as radius. Hararlick features and Zernike moments were estimated using Mahotas package [14]. After calculating features for each vesicle, descriptive statistics of each feature for all the vesicles in an individual cell were calculated. The descriptive statistics include mean, median (50%), lower quartile (25%), upper quartile (75%), maximum value(max), and minimum value(min). AP and AL features have their specific prefix before the feature and the prefix before AP/AL refers to the descriptive statistic of that feature. For example, mean_AP_area refers to the mean AP area of the all the AP in that specific cell. The list of 949 features extracted along with their respective categorization as biological entity and morphological type for each feature is available on GitHub.

Data preprocessing and standardization

Features containing NAN values were removed. Each individual feature for each cell was centralized using the median value of DMSO-treated cells (median (X_{DMSO})) and divided by 1.2532 times the mean absolute deviation (mad (X_{DMSO})) of that feature from the respective plate (equation is shown below). 1.2532 times the mean absolute deviation (mad (X_{DMSO})) is approximately equal to the standard deviation [15]. This approach was used to account for the batch effects between experiments.

$$X_s = \frac{X - \text{median}(X_{DMSO})}{1.2532 * \text{mad}(X_{DMSO})}$$

Random forest classification and feature importance

Features that vary significantly after adding rapamycin and wortmannin at all time points were combined at a single cell level. Features with a correlation of 0.75 and above with other features were removed to reduce redundancy and minimize multicollinearity. RandomForestClassifier algorithm from sklrean.ensemble was used as the model . The dataset was split into 5-folds. 4 folds were used for training the algorithm while the extra fold was used for testing the accuracy of the model using the micro F_1 score. 1000 trees were used as the random forest model, entropy as the criterion, and other hyperparameters are left as default. F_1 micro score package from sklearn.metrics was used for calculating the F_1 score [16]. A minimum of 70 cells were used for testing the accuracy of the model. Shapley Additive exPlanations (SHAP) method was used to interpret the feature importance from the classifier [10]. In short, SHAP assigns feature importance value for each feature by considering all possible combinations of features and the contribution of an individual feature to the final prediction. This was employed using SHAP package in Python.

Statistical analysis

Mann- Whitney U statistical test was used for estimating the statistical significance of each feature between untreated and treated cells. Benjamin-Hochberg method was used for false discovery rate correction. All features with an adjusted p-value lower than 0.05 were considered significant.

Data availability

The analyzed data is available on GitHub. Raw image data is available upon request.

Code availability

All codes for feature extraction, preprocessing, and analysis are available on https://github.com/shahlab247/ATG_morphological_profiling

References

[1] Peppard JV, Rugg C, Smicker M, et al. Identifying Small Molecules which Inhibit Autophagy: a PhenotypicScreen Using Image-Based High-Content Cell Analysis. Curr Chem Genomics Transl Med [Internet]. 2014 [cited 2023 Jan 21];8:3. Available from: /pmc/articles/PMC3941084/.

[2] Collins A, Huett A. A multi-phenotypic imaging screen to identify bacterial effectors by exogenous expression in a HeLa cell line. Sci Data 2018 51 [Internet]. 2018 [cited 2023 Jan 21];5:1–12. Available from: https://www.nature.com/articles/sdata201881.

[3] Schüssele DS, Haller PK, Haas ML, et al. Autophagy profiling in single cells with open source CellProfiler-based image analysis. Autophagy [Internet]. 2022 [cited 2023 Jan 21];

Available from: https://www.tandfonline.com/doi/abs/10.1080/15548627.2022.2065617.

[4] Stringer C, Wang T, Michaelos M, et al. Cellpose: a generalist algorithm for cellular segmentation. Nat Methods [Internet]. 2021 [cited 2021 Jun 13];18:100–106. Available from: https://doi.org/10.1038/s41592-020-01018-x.

[5] Ulicna K, Vallardi G, Charras G, et al. Automated Deep Lineage Tree Analysis Using a Bayesian Single Cell Tracking Approach. Front Comput Sci. 2021;3:92.

[6] Khotanzad A, Hong YH. Invariant Image Recognition by Zernike Moments. IEEE Trans Pattern Anal Mach Intell. 1990;12.

[7] Haralick RM, Dinstein I, Shanmugam K. Textural Features for Image Classification. IEEE Trans Syst Man Cybern. 1973;SMC-3:610–621.

[8] Beesabathuni NS, Park S, Shah PS. Quantitative and temporal measurement of dynamic autophagy rates. 2022 [cited 2022 Oct 11]; Available from: https://www.tandfonline.com/action/journalInformation?journalCode=kaup20.

[9] Strobl C, Boulesteix AL, Kneib T, et al. Conditional variable importance for random forests. BMC Bioinformatics [Internet]. 2008 [cited 2023 Jan 20];9:307. Available from: /pmc/articles/PMC2491635/.

[10] Lundberg SM, Erion G, Chen H, et al. From local explanations to global understanding with explainable AI for trees. Nat Mach Intell 2020 21 [Internet]. 2020 [cited 2023 Jan 20];2:56–67. Available from: https://www.nature.com/articles/s42256-019-0138-9.

[11] Loos B, Du Toit A, Hofmeyr JHS. Defining and measuring autophagosome flux - Concept and reality. Autophagy. 2014;10:2087–2096.

[12] Bray MA, Singh S, Han H, et al. Cell Painting, a high-content image-based assay for morphological profiling using multiplexed fluorescent dyes. Nat Protoc. 2016;11.

[13] Van Der Walt S, Schönberger JL, Nunez-Iglesias J, et al. Distributed under Creative Commons CC-BY 4.0 OPEN ACCESS scikit-image: image processing in Python. [cited 2023 Jan 25]; Available from: https://developers.google.com/.

[14] Coelho LP. Mahotas: Open source software for scriptable computer vision. J Open Res Softw [Internet]. 2013 [cited 2023 Jan 25];1:e3. Available from: http://openresearchsoftware.metajnl.com/articles/10.5334/jors.ac/.

[15] Geary RC. I. THE RATIO OF THE MEAN DEVIATION TO THE STANDARD DEVIATION AS A TEST OF NORMALITY. [cited 2023 Jan 25]; Available from: https://academic.oup.com/biomet/article/27/3-4/310/240061.

[16] Pedregosa FABIANPEDREGOSA F, Michel V, Grisel OLIVIERGRISEL O, et al. Scikit-learn: Machine Learning in Python. J Mach Learn Res [Internet]. 2011 [cited 2023 Jan 25];12:2825–2830. Available from: http://jmlr.org/papers/v12/pedregosa11a.html.

Chapter 4: *Implications and Future work*

The lack of methods to characterize autophagy quantitatively and comprehensively is a major bottleneck in gaining a fundamental understanding of biology as well as in developing applications. Chapter -2 and Chapter 3 delve into novel approaches for characterizing autophagy dynamically with high sensitivity and resolution. Chapter 2 highlighted the importance of measuring individual autophagy steps dynamically to gain a comprehensive understanding of the system and the perturbation targeting autophagy. While in Chapter 3, we tested the potential of using image-based temporal profiling for characterizing autophagy. In this chapter, we discuss the utilization of these methods to tackle some of the unaddressed challenges and propose conceptual ideas for future work. These studies can provide novel insights into fundamental biological questions, enable precise autophagy modulation, and accelerate drug screening.

What are the autophagy system parameters governing homeostasis or cell death?

Autophagy is pivotal in maintaining homeostasis and is heavily linked to cell death which can be utilized to maximize therapeutic benefit [1,2]. Especially in cancer, the complex interplay between autophagy, homeostasis, and cell death affects tumorigenesis. Therefore, understanding the role of autophagy parameters that govern these processes is critical. Here, we provide a list of questions that can elucidate the role of autophagy in cancer systematically.

1) What are the basal and optimal levels of autophagy activity (**Fig 4-1A**)?
2) How does the basal level of autophagy change in diseased cells and what is the influence of microenvironmental conditions such as amino acid starvation (**Fig 4-1B**)?
3) Can the homeostasis levels change due to a higher metabolic burden, making the diseased cells more sensitive to small perturbations (**Fig 4-1C**)?

4) Could the same diseased cell be driven to cell death by inhibiting as well as inducing autophagy but with different thresholds? An example illustration is shown in **Figure 4-1B** where the altered basal activity is closer to the lower threshold and therefore inhibiting could be a better strategy.

These questions remained far from reach because of a lack of quantitative, sensitive, and comprehensive. We briefly discuss experimental setups to tackle these questions using autophagy measurements discussed in previous chapters. First and foremost, establishing morphological profiles and basal rates for various mutants under normal and starvation conditions would act as a great resource to understand the change in basal state as a function of microenvironmental conditions. Combined with drug perturbations, these measurements can elucidate the fundamental mechanism involved and the responsiveness to therapeutic intervention based on genetic background and starvation conditions. Thus, aiding the development of therapies tailored to the genetic and microenvironmental makeup of the tumor.

Determining homeostatic levels requires extending autophagy limits in either direction of basal activity using modulators. However, it's important to remember, the phenotypic response is highly context-dependent and can vary based on the metabolic state and the pathway targeted [3]. Moreover, most small molecule drugs have off-target effects which could convolute the interpretation of the data. For example, the response to the same level of inhibition of autophagy through a Class III PI3K inhibitor can be different from a ULK1 inhibitor. Therefore, it is crucial to account for the pathway that is targeted along with the amount of autophagy perturbed. Optogenetic-based tools could partially overcome these challenges by allowing better specificity, precision, and reversibility [4]. Moreover, measuring key regulatory signaling nodes such as mTORC1, AMPK, Akt, and ULK1 simultaneously along with autophagy at a single cell level can

elucidate the decision-making process of the cell and the heterogeneity in response. This can be achieved by using biosensors and time-lapse imaging experiments [5].

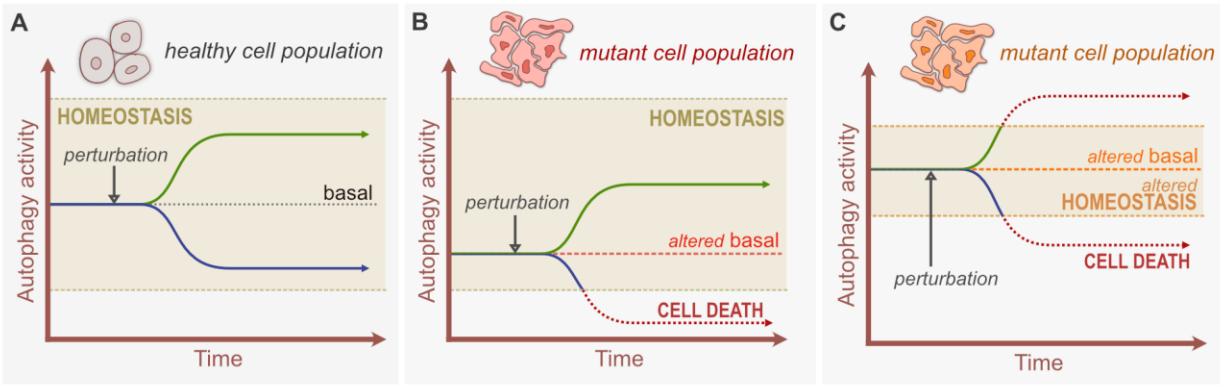

Figure 4-1: Variability in basal and homeostasis levels of autophagy. (**A**) Basal homeostasis. (**B**) Mutant cell population with altered basal but same homeostasis levels as healthy cells. (**C**) Mutant cell population with altered basal and altered homeostasis levels compared to healthy population.

It is also critical to understand the specific autophagy parameter governing a phenotype. For instance, if autophagy induction leads to cell death, probing the relationship between cell death and various parameters such as rate of induction and cargo degradation can provide fundamental insights. Performing such analysis need perturbations that can modulate specific characteristic of autophagy while keeping the other parameters constant. Rapamycin behavior observed in chapter 2 acts as one such example where we found a variable rate of induction as a function of time. Therefore, rapamycin can be used to identify the correlation between the phenotype and altered rate of change of autophagy. However, the number of well-characterized perturbations is limited and the need for such measurements is underlined. Identifying autophagy-related morphological signatures of cells before undergoing cell death can provide biomarkers for early detection and diagnosis of disease. In conclusion, systematic and sensitive measurements can reveal governing autophagy parameters related to homeostasis and cell death and enable modulation with precise control. Here we focused on cell death, but similar ideas can be applied to any phenotype of interest.

What is getting sequestered/ degraded and is it dynamic?

Selective cargo degradation is an important aspect of the autophagy pathway [6]. However, little work is done in characterizing the change in selective cargo captured and degraded under different perturbation conditions. The tools discussed in previous chapters are focused on characterizing all autophagy vesicles carrying various kinds of cargo. Similar tools can be extended for monitoring selective cargo along with autophagy vesicles. A simple but powerful study is understanding the specific cargo degraded under various perturbations. Simultaneously imaging of cargo of interest such as mitochondria and autophagy vesicles could facilitate the quantification of system parameters such as the fraction of specific cargo degraded at basal and under perturbation (**Fig 4-2**). It's important to note that the colocalization of cargo and autophagy vesicles does not automatically imply cargo degradation and the flow through the pathway needs to be confirmed using the rate measurements discussed in earlier chapters. Moreover, identifying the correlation between changes in autophagy vesicle morphology as a function of the kind of cargo sequestered would eventually allow the identification of the cargo sequestered without tagging the cargo using image-based profiling and predictive machine learning models.

Another aspect of cargo degradation that's interesting to investigate is whether the specific cargo degradation is dynamic or relatively uniform after a perturbation. As discussed in Chapter 1, many dynamic biological perturbations such as viruses exploit temporal and selective degradation of specific cargo. Measuring autophagy vesicles and cargo sequestered during virus replication dynamically can provide insights into the specific role of each cargo and its influence on virus replication. For example, lipophagy can be upregulated to provide ATP for virus replication but simultaneously reticulophagy could be inhibited as it's the primary site of flavivirus replication as discussed in Chapter 1. It is also important to remember that these processes are executed with high temporal accuracy. Therefore, measuring selective autophagy temporally during virus

infection could clear some of the ambiguity associated. Such information would enable the development of anti-viral therapies targeted toward the host. A limitation of such kind of analysis is the limited availability of non-overlapping fluorophores to simultaneously image multiple cargoes as well as autophagy vesicles using live cell imaging. Multiplexed immunofluorescence staining can overcome such limitations at the expense of single-cell temporal resolution.

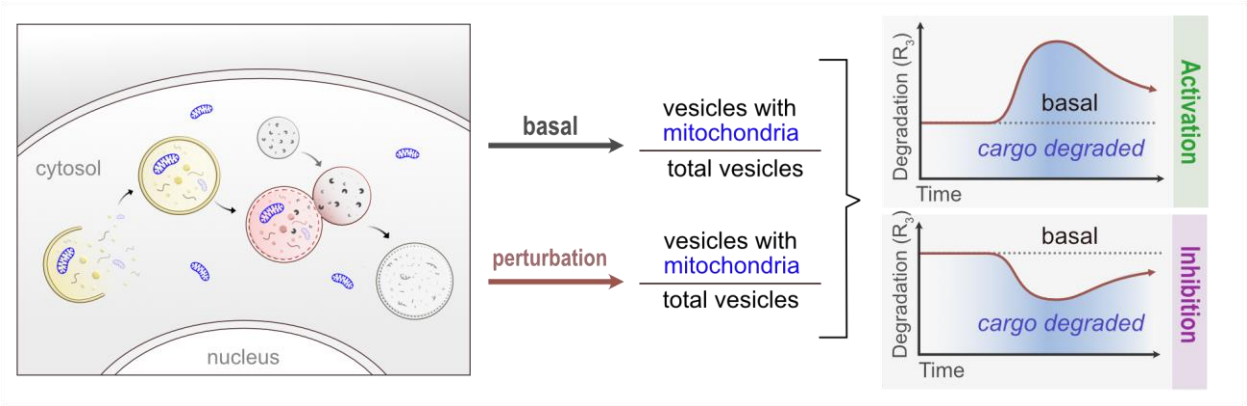

Figure 4-2: Quantification of selective autophagy can provide novel fundamental insights.

Can temporal resolution discern molecular components of the autophagy pathway?

Although significant progress has been made to understand molecular components involved in autophagy, there is still much that is not known [7,8]. The ability to capture changes on small-time resolution and to retain temporal information at a single cell level is a big advantage of the approaches discussed in chapter-2 and 3. Combining genetic perturbation with single-cell measurements with high temporal resolution can accelerate our understanding of the molecular components involved in the pathway. For instance, in Chapter 2 we have shown a delay in the increase in R_2 and R_3 after treatment with rapamycin even though the number of lysosomes remains constant. We hypothesized that there are other molecular components involved that are responsible for the delay. To uncover such molecular components involved in the fusion of autophagosome and autolysosome, the delay in the increase of fusion and acidification rates can be measured after downregulating various genes. An increase in delay after down-regulation

could indicate that the specific gene/protein is involved in the fusion step and vice versa (**Fig 4-3**). Coupling these approaches with methods such as optical pooled screening will increase the throughput of such experiments [9]. A recent study has highlighted the use of optical pooled screening and live cell imaging to confirm genes involved in the mitotic division by measuring the change in the duration of the division process [10]. Similar approaches can be applied to understand the machinery involved in autophagosome formation by measuring the timescale of response after genetic perturbation.

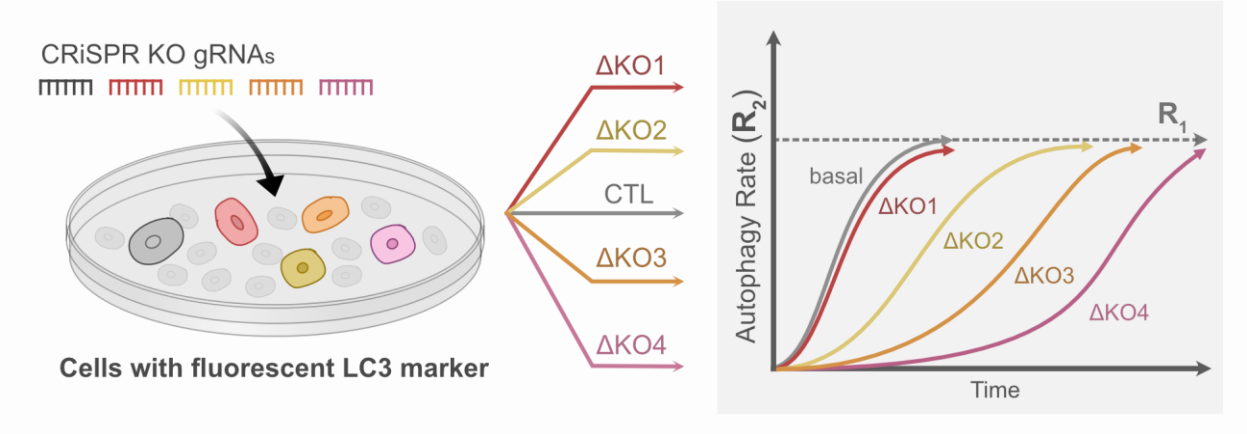

Figure 4-3: Conceptual representation of combining genetic perturbation and temporal measurements to reveal molecular components.

Scope for improvement

Integrating rates and image-based profiling measurements

Rate measurements discussed in Chapter 2 did not account for the change in morphology of the vesicles in the cells. Morphological features such as the size of the vesicles could play a key role in estimating the amount of cargo degraded along with the number. For instance, can perturbations increase the flux by increasing the amount sequestered in each vesicle instead of the number of vesicles or vice-versa? Therefore, incorporating morphological features such as size into the rate/cargo degradation measurements can be useful. Rates measurements are also

limited by the throughput which is pivotal for the screening drugs targeting autophagy. Both these challenges can be addressed by image-based profiling approaches discussed in Chapter 3

Although image-based profiling offers a high throughput and comprehensive characterization of autophagy phenotypes, direct measurement of individual steps of autophagy is not feasible, yet. This is important to understand the kinetics of the pathway, time scales of perturbation and feedback, and develop a correlation between autophagy steps or a parameter to a phenotype. Nevertheless, from chapter 3 we highlighted the potential of using morphological profiles to accurately differentiate and characterize autophagy activity. A similar principle can be used to develop predictive models to estimate autophagy rates based on the morphological profiles, time, and treatment. Therefore, combining morphological features with rate measurements would enable high-throughput characterization of the autophagy system without losing rate information about the individual steps.

Concluding remarks

The importance of autophagy in biomedicine is growing rapidly, but the lack of quantitative, sensitive, and dynamic measurements hinders the development of precise therapies and a full understanding of the process. In this dissertation, we proposed two new temporal methods to characterize autophagy and address these challenges. Quantitative and temporal rate measurements allow precise evaluation of individual rates of autophagy pathway temporally. Temporal image- based profiling approach facilitates the quantification of a various autophagy-related phenotypes at a single-cell level which can then be used to estimate the change in autophagy state accurately. Together, these approaches can facilitate high-throughput and precise measurement of autophagy. This work will accelerate drug discovery process and unravel new fundamental biological insights.

References

[1] Jung S, Jeong H, Yu SW. Autophagy as a decisive process for cell death. Exp Mol Med 2020 526 [Internet]. 2020 [cited 2023 Jan 9];52:921–930. Available from: https://www.nature.com/articles/s12276-020-0455-4.

[2] Bekker M, Abrahams S, Loos B, et al. Can the interplay between autophagy and apoptosis be targeted as a novel therapy for Parkinson's disease? Neurobiol Aging. 2021;100:91–105.

[3] Loos B, Engelbrecht AM, Lockshin RA, et al. The variability of autophagy and cell death susceptibility. https://doi.org/104161/auto25560 [Internet]. 2013 [cited 2023 Jan 26];9:1270–1285. Available from: https://www.tandfonline.com/doi/abs/10.4161/auto.25560.

[4] D'Acunzo P, Strappazzon F, Caruana I, et al. Reversible induction of mitophagy by an optogenetic bimodular system. Nat Commun 2019 101 [Internet]. 2019 [cited 2023 Jan 26];10:1–13. Available from: https://www.nature.com/articles/s41467-019-09487-1.

[5] Kosaisawe N, Sparta B, Pargett M, et al. Transient phases of OXPHOS inhibitor resistance reveal underlying metabolic heterogeneity in single cells. Cell Metab. 2021;33:649-665.e8.

[6] Galluzzi L, Baehrecke EH, Ballabio A, et al. Molecular definitions of autophagy and related processes. EMBO J [Internet]. 2017 [cited 2023 Jan 8];36:1811–1836. Available from: https://onlinelibrary.wiley.com/doi/full/10.15252/embj.201796697.

[7] Wen-You Yim W, Mizushima N. Cell Discovery Lysosome biology in autophagy. 2020 [cited 2023 Jan 8];6:6. Available from: https://doi.org/10.1038/s41421-020-0141-7.

[8] Chang C, Jensen LE, Hurley JH. Autophagosome biogenesis comes out of the black box.

Nat. Cell Biol. 2021.

[9] Feldman D, Singh A, Schmid-Burgk JL, et al. Optical Pooled Screens in Human Cells. Cell. 2019;179.

[10] Funk L, Su K-C, Ly J, et al. The phenotypic landscape of essential human genes. Cell [Internet]. 2022 [cited 2023 Jan 26];185. Available from: https://pubmed.ncbi.nlm.nih.gov/36347254/.

Appendix A: Supplemental information for quantitative and temporal measurement of autophagy rates

Bafilomycin A_1 mechanism of action does not affect non-steady state measurements.

Governing equations

$$\frac{dAP}{dt} = R_1 - R_2 \quad (1)$$

$$\frac{dAL}{dt} = R_2 - R_3 \quad (2)$$

Autophagy vesicles under normal conditions.

1) Autophagosomes (AP) are yellow (both green and red). Yellow puncta are denoted by Y
2) Autolysosomes (AL) are red because of acidification.
3) Note- if bafilomycin A_1 mechanism of action is to stop autolysosome acidification, autolysosomes would also be yellow.

Case 1: Bafilomycin A_1 inhibits the fusion step.

$$R_2 = 0$$

In this case, the rate of accumulation of autophagosomes, which are in yellow, represents the rate of autophagosome formation.

$$Y = AP \quad (3)$$

$$\left(\frac{dY}{dt}\right)_{inh} = \left(\frac{dAP}{dt}\right)_{inh} = R_1 \quad (4)$$

Case 2: Bafilomycin A_1 inhibits the acidification step.

$$R_3 = 0 \quad (5)$$

In this case, the total number of yellow puncta that would accumulate after the addition of bafilomycin A_1 is equal to the sum of autophagosomes and autolysosomes following bafilomycin A_1 treatment.

$$Y = AP + AL \tag{6}$$

Differentiating equation 6 with respect to time would provide

$$\frac{dY}{dt} = \frac{dAP}{dt} + \frac{dAL}{dt} \tag{7}$$

While adding equations 1 and 2 would provide

$$\frac{dAP}{dt} + \frac{dAL}{dt} = R_1 - R_2 + R_2 - R_3 \tag{8}$$

As we know, $R_3 = 0$ because acidification/degradation is completely inhibited. So, equation 8 reduces to

$$\frac{dAP}{dt} + \frac{dAL}{dt} = R_1 \tag{9}$$

Comparing equation 7 and equation 9 shows that

$$\frac{dY}{dt} = R_1 \tag{10}$$

Therefore, the rate of accumulation of yellow puncta, in either case, would provide the rate of formation of autophagosomes from which other rates can be calculated as discussed in the main text.

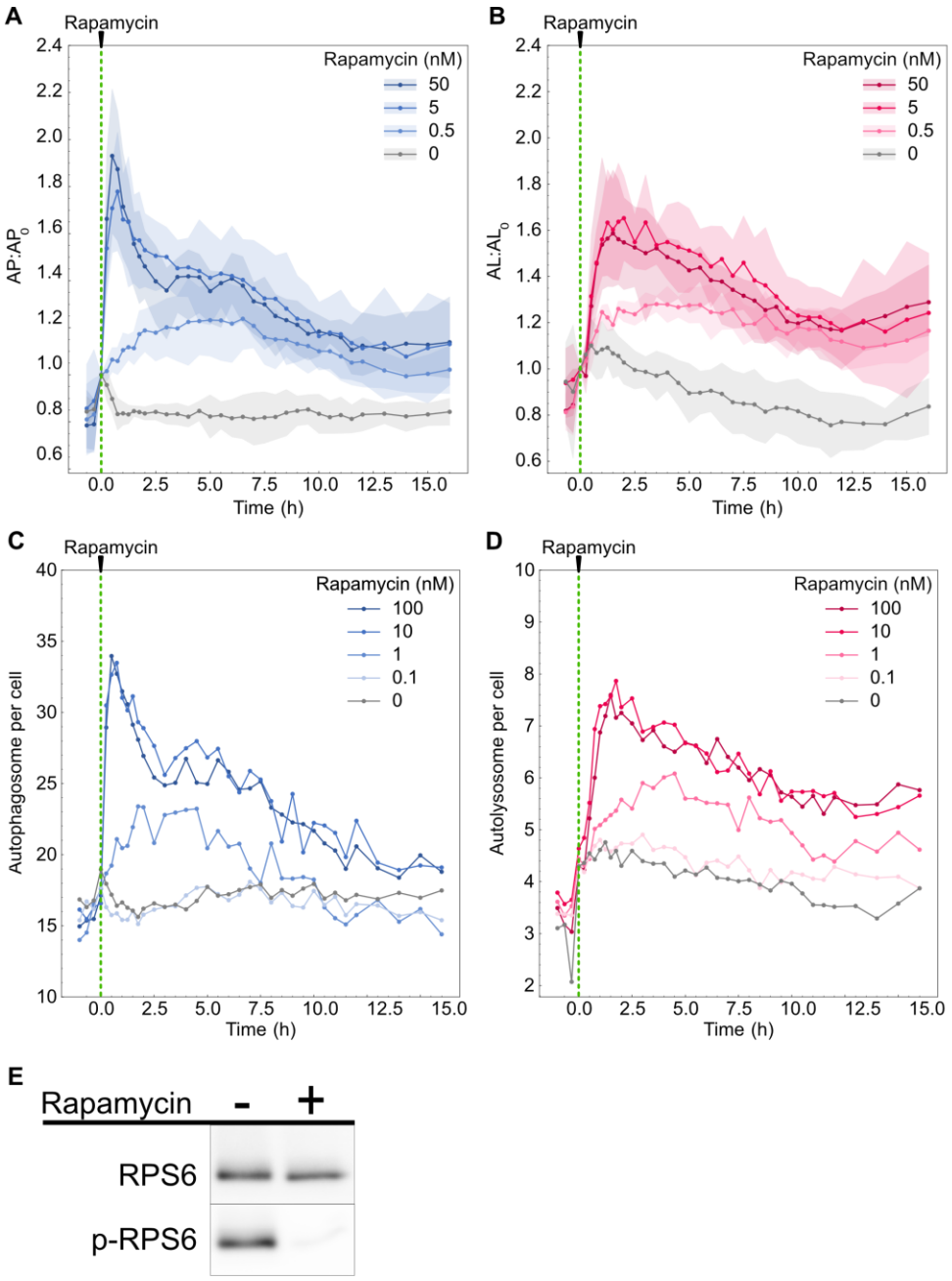

Figure A-1. Autophagosome and autolysosome dynamics for additional rapamycin concentration. Dynamics of (A) Autophagosome and (B) autolysosome number after rapamycin treatment. The indicated concentration of rapamycin was added at 0 min. The number of autophagosomes and autolysosomes at 0 min was used as the normalization factor. Data points represent mean while shaded area represents standard deviation. Four independent replicates were performed. Raw (C) autophagosome and (D) autolysosomes dynamics of one individual replicate after rapamycin treatment (E) Western blot of p-RPS6 (phospho-RPS6 ribosomal protein (Ser 240/244)) after treatment with 100 nM rapamycin for 2.5 h. Total RPS6 ribosomal protein was used as a control.

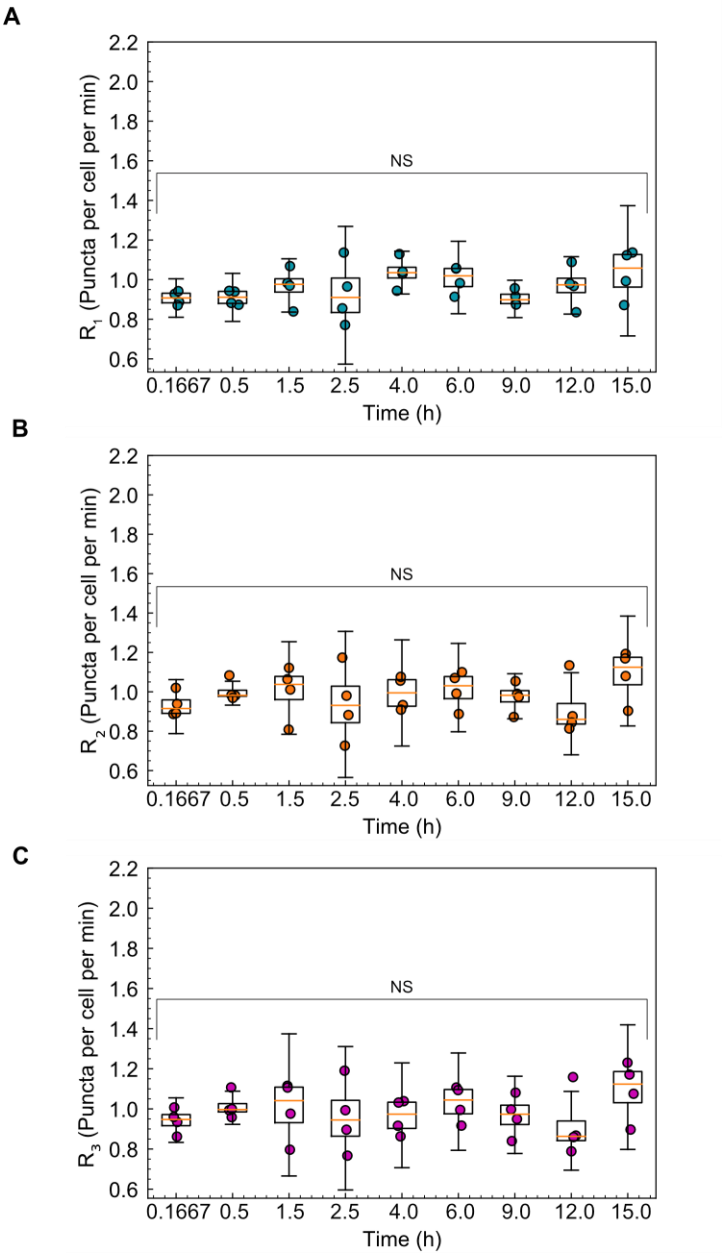

Figure A-2. Basal autophagy rates remain constant over time. (**A**) Rate of autophagosome formation (R_1). (**B**) Rate of autolysosome formation (R_2). (**C**) Rate of autolysosome degradation (R_3). NS indicates not significant. P-values were calculated using a one-way ANOVA test.

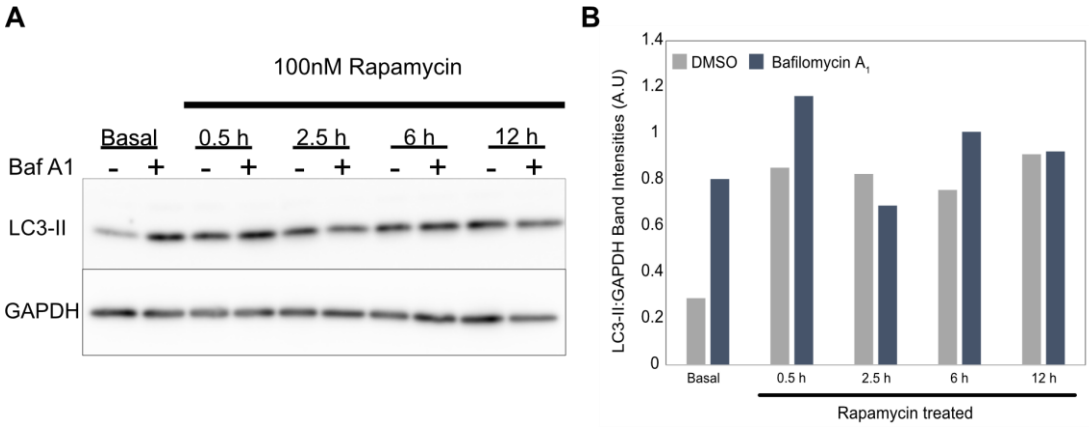

Figure A-3. Western blot of LC3-II accumulation during rapamycin treatment. **(A)** LC3-II and GAPDH protein measurement using western blot. Cells were treated with 100 nM rapamycin for indicated times followed by 500 nM bafilomycin A_1 (Baf A1) treatment for 2 h. Basal samples represent DMSO-treated cells. (**B**) Quantification of the western blot shown in **Fig A-3A** using densitometry. LC3-II band intensity was normalized with the respect to GAPDH band intensity in the same lane.

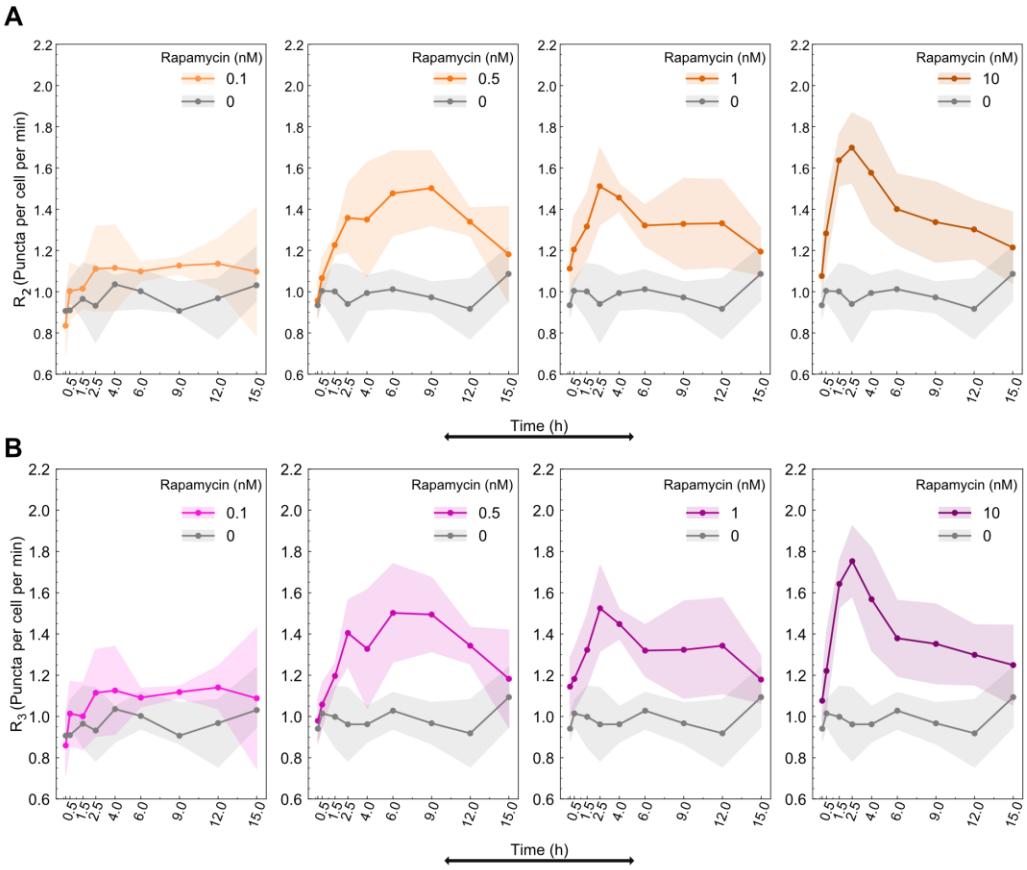

Figure A-4. Rapamycin concentration modulates autolysosome formation and degradation rates. (**A**) Temporal dynamics of rate of autolysosome formation (R_2) and (**B**) Autolysosome degradation (R_3) for different concentrations of rapamycin. Data points represent the mean, while the shaded area represents ± standard deviation. Four independent replicates were performed.

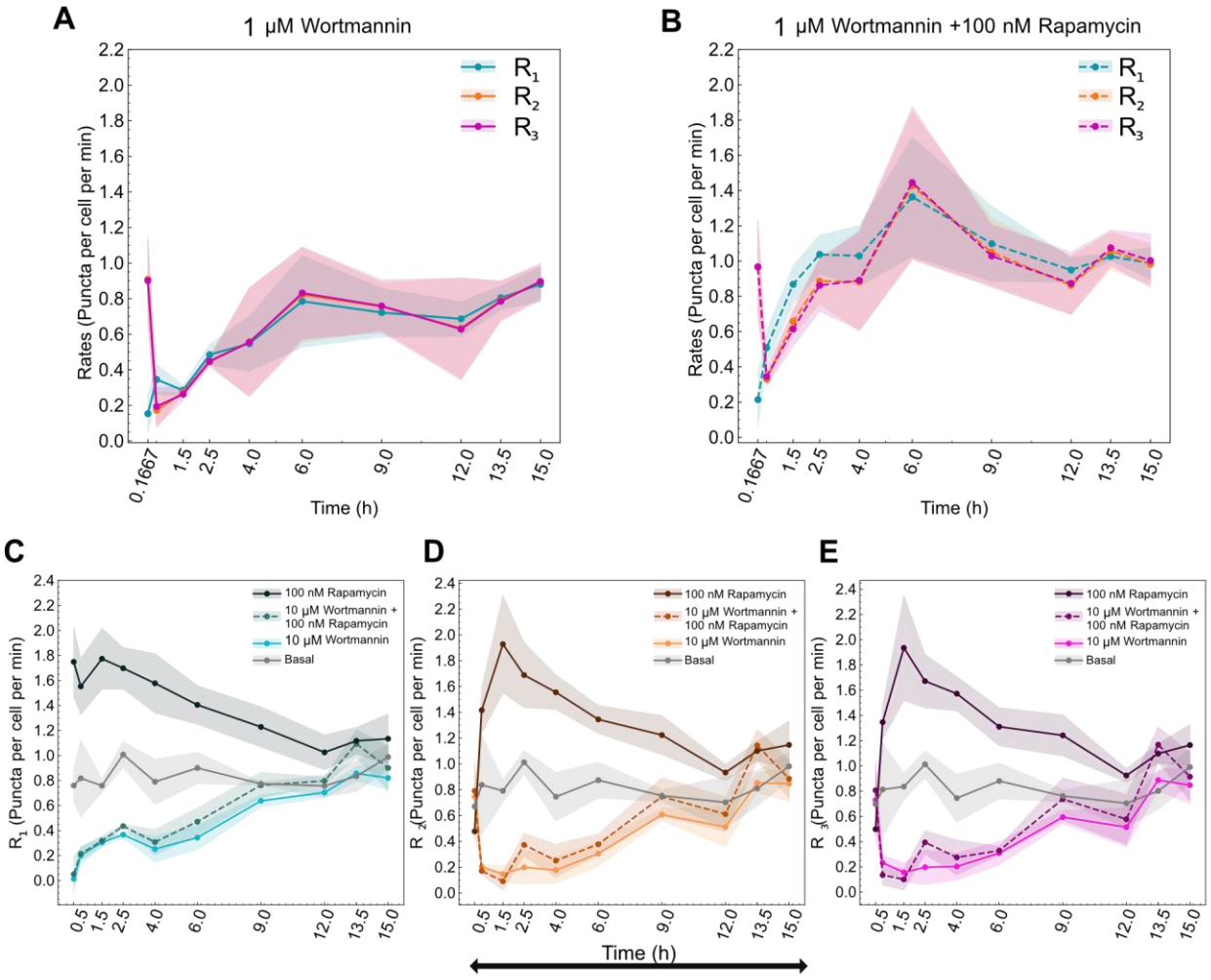

Figure A-5. Temporal evolution of autophagy rates during wortmannin treatment. All three autophagic rates (R_1, R_2, R_3) were measured at indicated times for (**A**) 1 μM Wortmannin only and (**B**) 1 μM wortmannin with 100 nM rapamycin. Measurement of (**C**) R_1 (**D**) R_2 **(**E**)** R_3 for basal, 10 μM wortmannin with and without 100 nM rapamycin, and 100 nM rapamycin alone at indicated times. Data points represent the mean, while the shaded area represents ± standard deviation. Three independent replicates were performed.

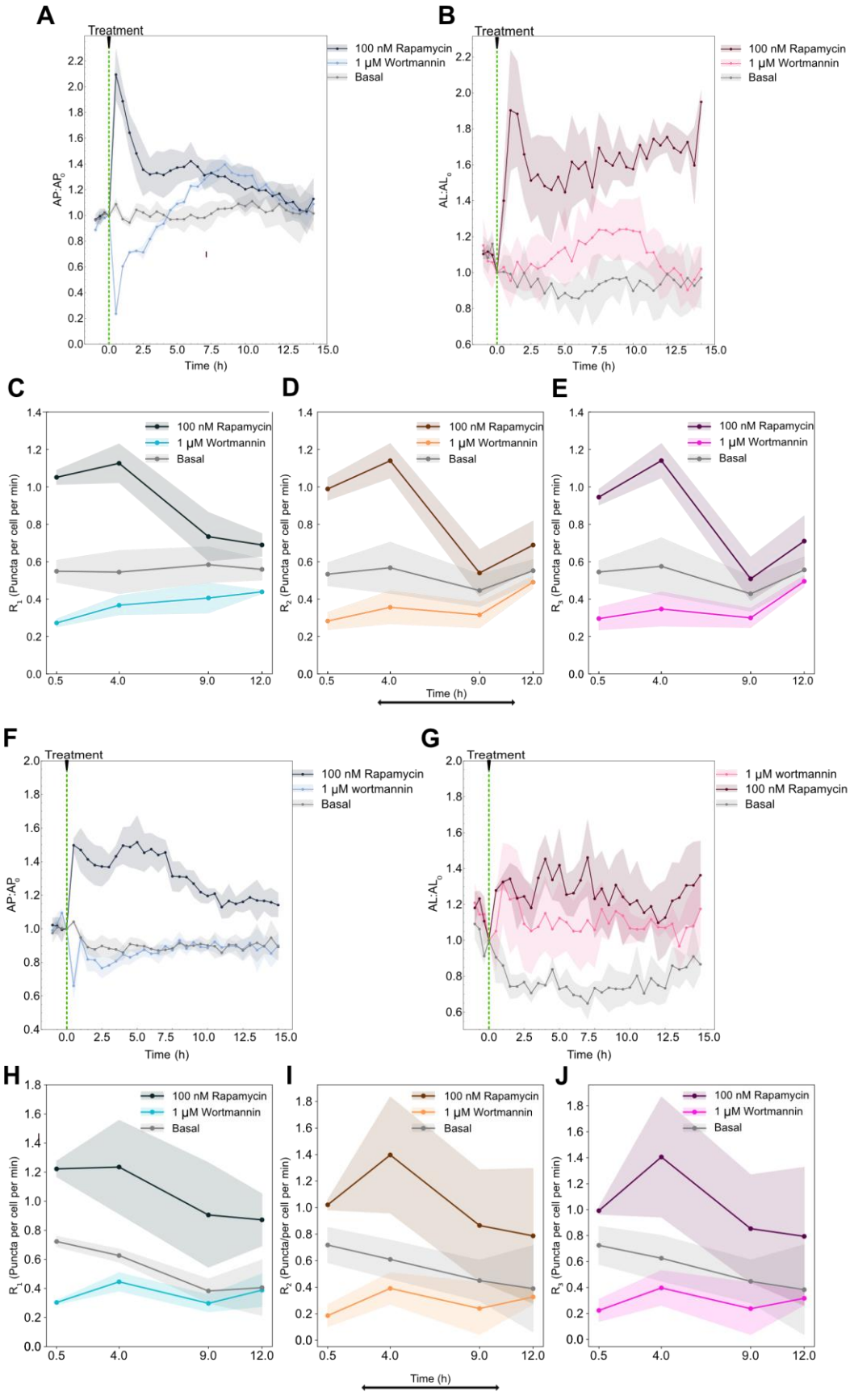
A
Treatment
100 nM Rapamycin
1 μM Wortmannin
Basal
AP:AP0
Time (h)
B
Treatment
100 nM Rapamycin
1 μM Wortmannin
Basal
AL:AL0
Time (h)
C
D
E
100 nM Rapamycin
1 μM Wortmannin
Basal
R1 (Puncta per cell per min)
R2 (Puncta per cell per min)
R3 (Puncta per cell per min)
Time (h)
F
Treatment
100 nM Rapamycin
1 μM wortmannin
Basal
AP:AP0
Time (h)
G
Treatment
1 μM wortmannin
100 nM Rapamycin
Basal
AL:AL0
Time (h)
H
I
J
100 nM Rapamycin
1 μM Wortmannin
Basal
R1 (Puncta per cell per min)
R2 (Puncta/per cell per min)
R3 (Puncta per cell per min)
Time (h)

Figure A-6. Validation of autophagy rate measurements using bulk A549- pHluorin-mKate2-LC3 and U2OS-pHluorin-mKate2-LC3 cell line. (**A**) Autophagosome and (**B**) autolysosome dynamics of bulk A549-pHluorin-mKate2-LC3 cell line after chemical treatment. Temporal evolution of (**C**) R_1 (**D**) R_2 **(E)** R_3 of bulk A549- pHluorin-mKate2-LC3 cell line for basal, 1 µM wortmannin, and 100 nM rapamycin. Data points represent the mean, while the shaded area represents ± standard deviation. Three technical replicates were performed. (**F**) Autophagosome and (**G**) autolysosome dynamics of bulk U2OS- pHluorin-mKate2-LC3 cell line after chemical treatment. Temporal evolution of (**C**) R_1 (**D**) R_2 **(**E**)** R_3 of bulk U2OS- pHluorin-mKate2-LC3 cell line basal after treatment with 1 µM wortmannin, and 100 nM rapamycin. Data points represent the mean, while the shaded area represents ± standard deviation. Three technical replicates were performed.

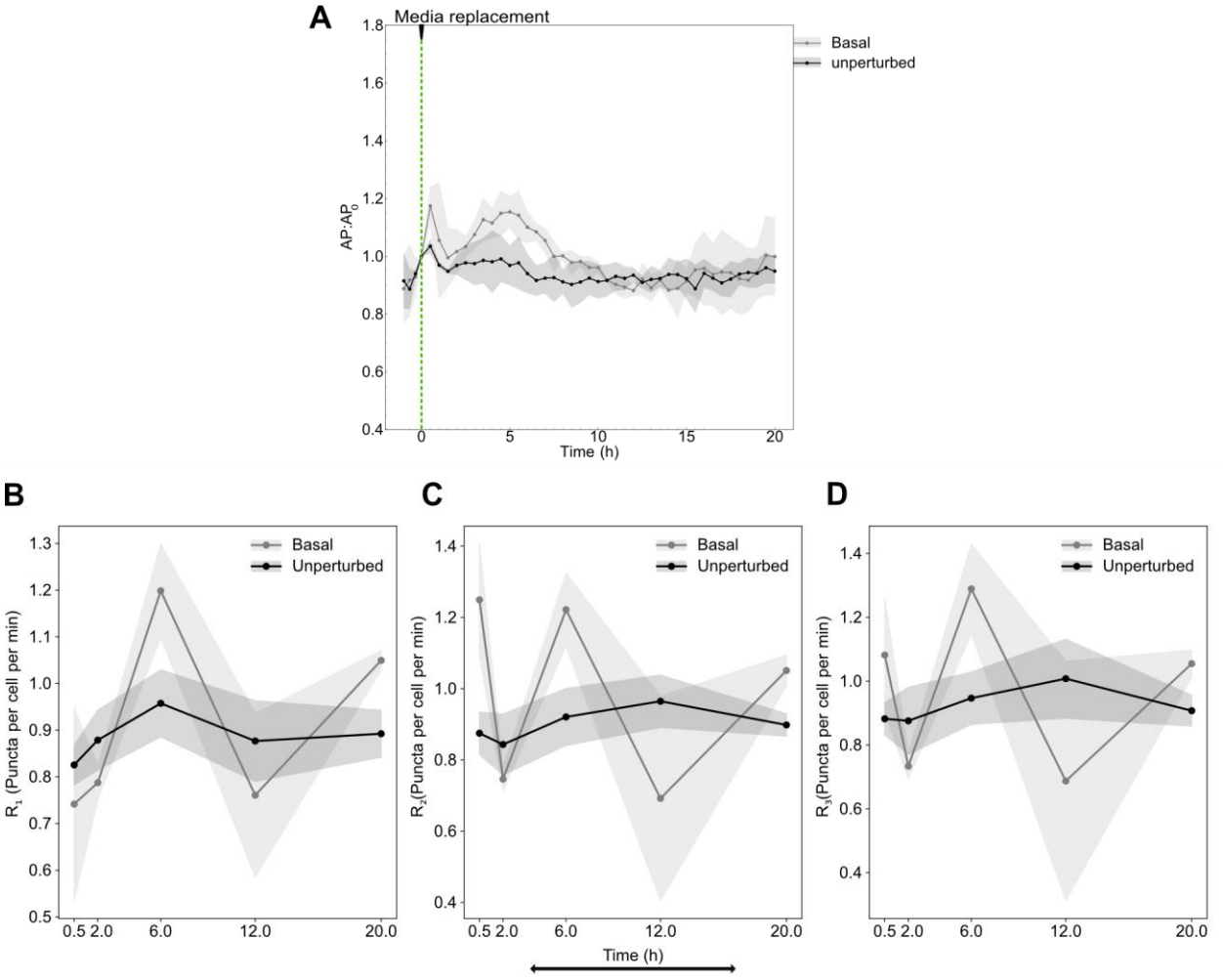

Figure A-7. Replacing media perturbs autophagy. (**A**) Autophagosomes dynamics for basal condition, where media was replaced with normal media, compared to completely unperturbed condition. Data points represent the mean, while the shaded area represents ± standard deviation. Three independent replicates were performed. Temporal dynamics of (**B**) R_1 (**C**) R_2 **(D)** R_3 under basal treatment where media was replaced compared to unperturbed condition. Data points represent the mean, while the shaded area represents ± standard deviation. Three technical replicates were performed.

Appendix B: Supplemental information for image-based temporal profiling of autophagy-related phenotypes

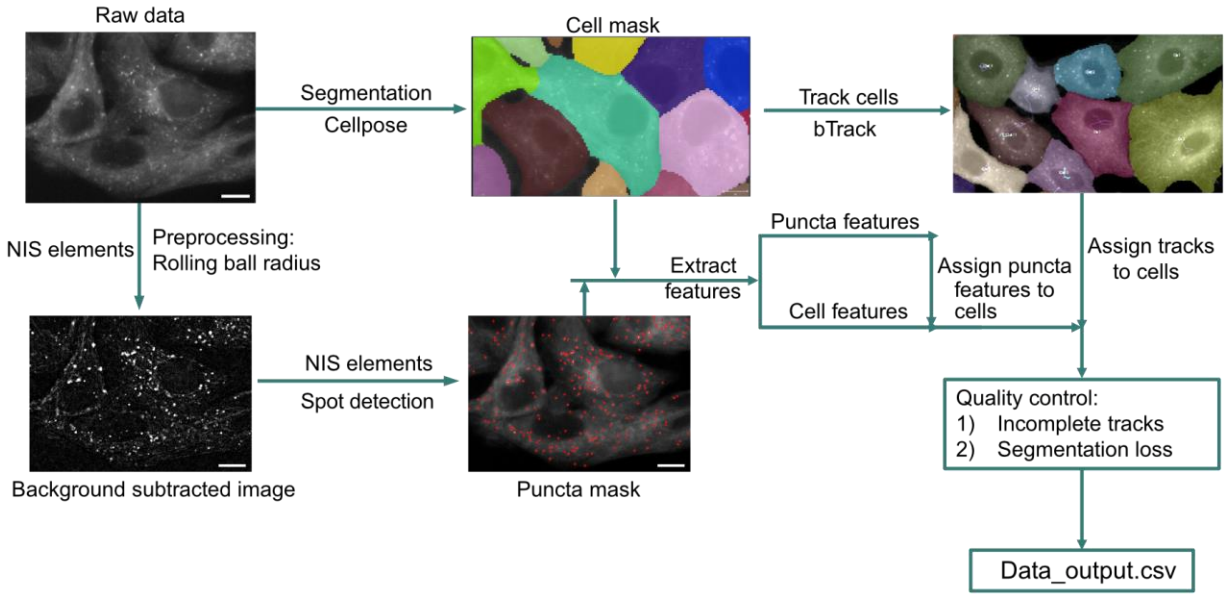

Figure B-1: Image analysis pipeline

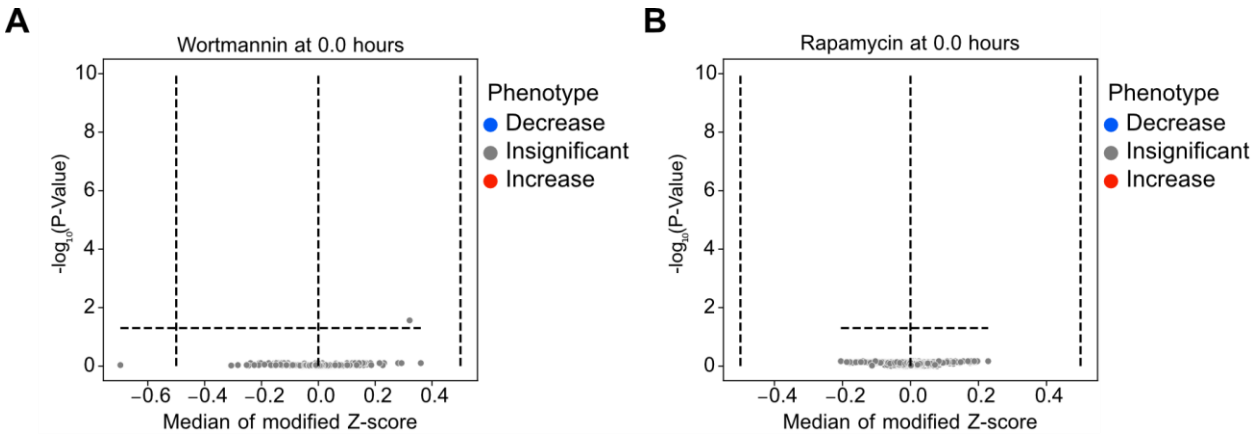

Figure B-2. Confirmation of no change in morphological features before treatment. **A-B:** Volcano plot of cellular features before treatment.

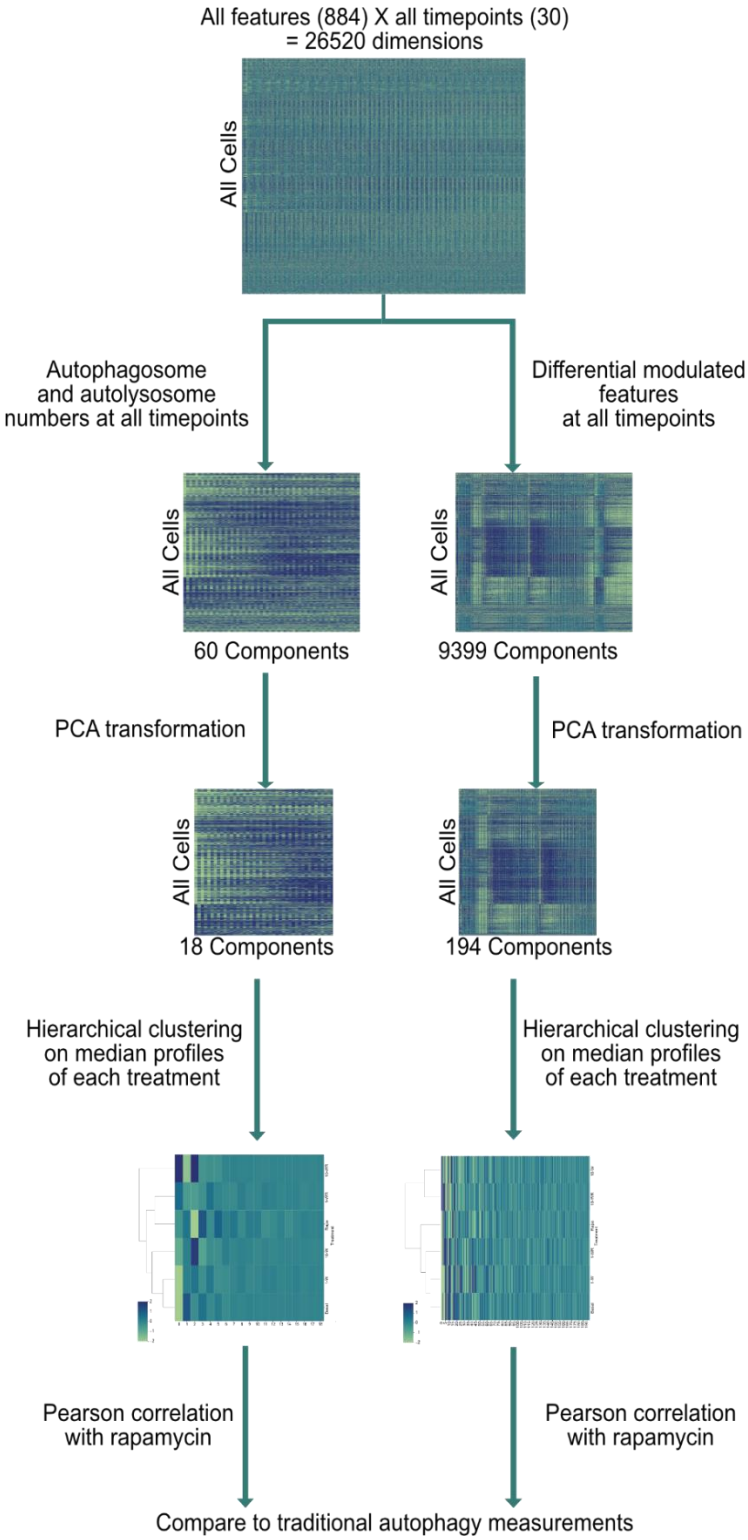

Figure B-3. Stepwise procedure for calculating profile correlation. 90% of the variance is retained after PCA. For hierarchical clustering based on median profiles, sns.clustermap function was used. '*average'* method and '*euclidean'* metric was used for generating the clusters.